FORMATION OF CARBONACEOUS NANOPARTICLES FROM METHANE IN NON-EQUILIBRIUM PLASMA FLOW REACTOR

A THESIS SUBMITTED TO
THE GRADUATE SCHOOL OF NATURAL AND APPLIED SCIENCES
OF
MIDDLE EAST TECHNICAL UNIVERSITY

BY

İBRAHİM BURAK ŞEN

IN PARTIAL FULFILLMENT OF THE REQUIREMENTS
FOR
THE DEGREE OF MASTER OF SCIENCE
IN
CHEMICAL ENGINEERING

AUGUST 2025

Approval of the thesis:

FORMATION OF CARBONACEOUS NANOPARTICLES FROM METHANE IN NON-EQUILIBRIUM PLASMA FLOW REACTOR

submitted by **İBRAHİM BURAK ŞEN** in partial fulfillment of the requirements for the degree of **Master of Science** in **Chemical Engineering, Middle East Technical University** by,

Prof. Dr. Naci Emre Altun
Dean, **Graduate School of Natural and Applied Sciences** _____

Prof. Dr. Yusuf Uludağ
Head of the Department, **Chemical Engineering** _____

Assist. Prof. Dr. Necip Berker Üner
Supervisor, **Chemical Engineering, METU** _____

Examining Committee Members:

Prof. Dr. Gürkan Karakaş
Chemical Engineering, METU _____

Asst. Prof. Dr. Necip Berker Üner
Chemical Engineering, METU _____

Assoc. Prof. Dr. Emre Büküşoğlu
Chemical Engineering, METU _____

Prof. Dr. Esin Varol
Chemical Engineering, Eskişehir Technical University _____

Asst. Prof. Dr. Yasemin Saygılı
Energy Systems Engineering, Ankara University _____

Date: 28.08.2025

I hereby declare that all information in this document has been obtained and presented in accordance with academic rules and ethical conduct. I also declare that, as required by these rules and conduct, I have fully cited and referenced all material and results that are not original to this work.

Name Last name : İbrahim Burak Şen

Signature :

ABSTRACT

FORMATION OF CARBONACEOUS NANOPARTICLES FROM METHANE IN NON-EQUILIBRIUM PLASMA FLOW REACTOR

Şen, İbrahim Burak
Master of Science, Chemical Engineering
Supervisor : Asst. Prof. Dr. Necip Berker Üner

August 2025, 102 pages

Carbon is the fourth most abundant element in the universe. It can be found in various forms such as graphene, graphite, fullerene, diamond and more. Graphite and nanodiamonds are the two crystalline structured forms of carbon. Graphite is being used in battery production due to its high thermal and electrical conductivity and intercalation capacity. Bulk diamond is used in cutting tools while nanodiamond is used for bioimaging and quantum computing. Although the synthesis of these materials in a thermally equilibrated medium is well-established, their direct synthesis from gas phase to solid free-standing particles in non-equilibrium flow-through plasmas is not yet fully understood due to difficulties in particle nucleation and rapid film formation at the reactor walls.

In this thesis, methane conversion into carbonaceous nanoparticles was tested through a variety of experiments and characterization methods to make a preliminary study for nanodiamond particle formation which was enabled by integration of a Stairmand-type cyclone separator used to eliminate contaminated particles through mobility differences. Size-separated, hence, purified particles were subjected to intensive characterization via XRD, Raman, TGA, and TEM. All operating

parameters – pressure, gas composition and plasma power - effected crystalline sizes, however, residence time of particles had the strongest influence.

Increased residence time led to formation of highly anisotropic particles whose grain sizes were calculated from XRD and Raman. In-plane crystalline size was 2.2 nm and crystalline size in stacking direction was 1.43 nm for highest graphitized particle. However, HRTEM images showed these particles contained bigger grains sized up 8 nm while depicting an evolutionary pathway for how morphology of particles changed with varying residence time. It was concluded that compared to synthesis of Si, metal oxides and other nanocrystals, crystalized carbonaceous nanoparticle formation in such plasmas is more energy intensive, favoring high pressures and is more dependent on residence time.

Keywords: Graphite, Non-equilibrium plasma reactor, Synthesis, Methane conversion, Carbon characterization.

ÖZ

İÇTEN AKIŞLI DENGESİZ PLAZMA REAKTÖRÜNDE METANDAN KARBONLU NANOPARÇACIK ÜRETİMİ

Şen, İbrahim Burak
Yüksek Lisans, Kimya Mühendisliği
Tez Yöneticisi: Dr Öğr. Üyesi Necip Berker Üner

Ağustos 2025, 102 sayfa

Karbon evrendeki dördüncü en yaygın bulunan elementtir. Grafit, grafen, fulleren ve elmas dahil olmak üzere pek çok formda bulunabilir. Grafit ve elmas kristal yapıda bulunan karbon formlarıdır. Grafit yüksek elektrik ve ısı iletkenliği ve arakatkı kapasitesi nedeniyle batarya üretiminde kullanılır. Elmaslar kesim araçlarında kullanılırken nanoelmaslar ise kuantum bilgi işlemede ve biyogörüntüleme alanında kullanılabilmektedir. Bu parçacıkların termal dengede bulunan ortamlarda sentezi iyi bilinmesine karşın parçacık çekirdeklenmesinin zorluğu ve reaktör duvarlarında hızlı film oluşması gibi sebeplerden dolayı direkt gaz fazından dengesiz içten akmalı plazma reaktörlerinde sentezi henüz iyi oturmamıştır.

Bu tezde, üretilen ve duvardan kopan parçacıkları mobilitelerine göre ayıran Stairmand tarzı bir siklon ayırıcı kullanımıyla gaz fazındaki metandan direkt olarak karbonlu nanoparçacık oluşumu çeşitli deneyler ve karakterizasyon yöntemleriyle test edilmiştir. Boyutlarına göre ayrılmış, bir başka deyişle saflaştırılmış parçacıklar XRD, Raman, TGA ve TEM gibi karakterizasyon yöntemleriyle incelenmiştir. Basınç, gaz kompozisyonu, plazma gücü gibi parametrelerin kristal boyutlarına etki

ettiği görülmesine karşın en büyük etkiyi parçacıkların reaktörde kalış sürelerinin yaptığı görülmüştür.

Artan reaktörde kalma süresi eşyönsüz (anizotropik) parçacık oluşumuna sebep olmuş olup XRD ve Raman ölçümleriyle kristal boyutları hesaplanmıştır. En çok kristalize olmuş parçacık için yatay düzlemdeki kristal boyutu 2.2 nm iken dikey düzlemdeki kristal boyutu 1.43 nm bulunmuştur. Buna karşın, yüksek çözünürlüklü TEM görüntüleri bu parçacıkların 8 nm'ye kadar kristaller içerdiğini göstermiştir. Bunlara ek olarak parçacık morfolojisinin reaktörde kalma süresi ve basınçla nasıl evrimleştiği gösterilmiştir. Bu tarz plazmalarda kristalize olmuş karbonlu parçacık üretmenin Si, metal oksitler ve diğer nanokristallerin üretimine göre çok daha fazla enerjiye ve daha yüksek basınçlara ihtiyaç duyduğu ve uzun reaktörde kalma süreleri gerektirdiği sonuçlarına varılmıştır. Bu çalışmada elde edilen sonuçlar ile, aynı deney düzeneği kullanılarak nanoelmas ve katkılı nanoelmas parçacıkları üretmek için bir altyapı oluşturulmuştur.

Anahtar Kelimeler: Grafit, Dengesiz plazma reaktörü, Sentez, Metan dönüşümü, Karbon karakterizasyonu.

To Carl Sagan, who inspired many, including my childhood self, to hold science as a candle in the dark, guiding us through a demon-haunted world

ACKNOWLEDGMENTS

This work would not have been possible without the exceptional guidance of my advisor, Necip Berker Üner, over the past four years we worked together. I couldn't have been more grateful for his unlimited tolerance, leadership and teaching skills. His ability to transform complexity into simplicity not only made me a better student but a better man. He never gave up on me and consistently supported me when it comes to academical or personal life matters.

I would also like to thank Zeynep Çulfaz Emecen, whom I have been a teaching assistant to for three semesters, for trusting me from the very beginning. Her confidence in me was most evident when she allowed me to teach the class for an entire week during the third week of our first semester together - an experience that ignited my passion for teaching and an experience I still remember very fondly.

I want to thank members of NEPaL Research Group; Hüseyin Öztürk, Zeynep Birce Reyhan, Berkay Şimşek, AbdelAziz Hamza, İpek Dengiz, Berkin Başarır, Andaç Yağız Kaya, Sultan Muslu and Yağmur Ön. It is good to know that these wonderful people share the same passion with me. I also want to thank my friends Onur Kaan Aydın, Metin Alp Yurtseven, Furkan Al, Gülce İlhan, Bengisu Barış, Berk Can İçten and Toprak Çağlar. Without them, my days at the department would have been so bland.

My best friends -Doğa Özcan, Ege Kosova, Alper Beşparmak and Fırat Sarıbaş- they were the ones I spent most of my time not only in my graduate days but since elementary school. I thank them for countless moments of laughter, support and unforgettable memories.

I cannot express the depth of gratitude I have towards my family. My father and my mother provided me with everything I needed, even in the toughest times. They have always strived to help their sons become best versions of themselves. This thesis belongs to them as much as it does to me. And my brother, thanks for the joga bonitos we shared not only on the pitch but in life.

Finally, I want to thank my dear wife, Büşra Yarım Şen, and our cat, Kırpık, for always being by my side - for their love and warmth and for sharing every moment with me, in sickness and in health. I love you.

TABLE OF CONTENTS

ABSTRACT v

ÖZ vii

ACKNOWLEDGMENTS x

TABLE OF CONTENTS xii

LIST OF FIGURES xv

LIST OF ABBREVIATIONS xvii

CHAPTERS

1 INTRODUCTION 1

2 LITERATURE REVIEW 5

2.1 Carbonaceous Nanoparticles 5

2.1.1 Classification and Properties 5

2.1.2 Structural Evolution of Carbonaceous Nanoparticles: The Ferrari-Robertson Model 7

2.1.3 Applications 8

2.2 Synthesis of Carbonaceous Nanoparticles from Gas-Phase Precursors 10

2.2.1 Thermal Processes 10

2.2.2 Non-equilibrium Processes 12

2.3 Non-equilibrium Plasma Reactors and Fundamentals 13

2.3.1 Reactor Types 15

2.4 Non-equilibrium Flow-through Reactors for Nanomaterial Production 19

2.4.1 Silicon Nanoparticle Formation Mechanism from Silane as an Example to Gas-to-Solid Conversion 19

2.4.2 Operational Parameters 22

2.4.3 Advantages and Limitations 24
2.5 Carbonaceous Nanoparticle Formation in Capacitively-coupled Flow-through RF Plasma 24
3 EXPERIMENTAL METHODS 27
3.1 Experimental Setup 27
3.1.1 Gas Feed 27
3.1.2 Plasma Reactor 28
3.1.3 Particle Separation 30
3.1.4 Particle Collection 32
3.2 Powder Characterization Methods 34
3.2.1 X-Ray Diffraction 34
3.2.2 Raman Spectroscopy 34
3.2.3 Thermogravimetric Analysis 35
3.2.4 Optical and Electron Microscopy 35
3.3 Plasma Diagnostics 36
4 RESULTS AND DISCUSSION 39
4.1 Particle Separation Performance 39
4.2 Effect of Reactor Pressure and Residence Time on OES 45
4.3 Investigation of Particle Formation via Bulk Characterization 49
4.4 Evolution of Particle Formation via TEM 55
5 SUMMARY, CONCLUSION AND FUTURE WORK 63
5.1 Summary 63
5.2 Conclusion 64
5.3 Future Work 64

REFERENCES 67

A. CONTROL AND CALIBRATION OF MFCs THROUGH ARDUINO-BASED BUBBLE FLOW METER AND CONTROL BOX 87

B. STAIRMAND-TYPE LOW-PRESSURE CYCLONE SEPARATOR DESIGN 91

C. CALCULATION OF FILTER COLLECTION EFFICIENCY 99

D. X-RAY DIFFRACTION DATA USED FOR FWHM CALCULATIONS 101

LIST OF FIGURES

FIGURES

Figure 2.1. Ternary diagram of amorphous carbon based on sp^2, sp^3 bonds and H content. 7
Figure 2.2. Schematic of formation of polycyclic aromatic hydrocarbons. 11
Figure 2.3. HACA mechanism. 12
Figure 2.4. Complementary views of nonequilibrium phenomena. 14
Figure 2.5. Scheme of a compact non-thermal plasma torch for carbonaceous nanoparticles synthesis. 16
Figure 2.6. Plasma enhanced chemical vapor deposition reactor during operation. 18
Figure 2.7. (a) Physical scheme of inception of cluster growth. 20
Figure 3.1. Schematic drawing of the experimental setup. 27
Figure 3.2. Plasma reactor image with the RF shielding. 30
Figure 3.3. Zoomed-in portion of particle separation equipment in the experimental setup. 31
Figure 3.4. Removable 400-mesh stainless steel wire gauzes. 32
Figure 3.5. TEM grid installed removable mesh filters. 33
Figure 3.6. Configurations of OES. 36
Figure 4.1. Plasma reactor images. 39
Figure 4.2. Particles collected at the upstream of the impaction stage. 40
Figure 4.3. Particles collected at the upstream of the cyclone. …….41
Figure 4.4. Particles collected at the upstream of the cyclone. 42
Figure 4.5. TGA and DTG curves of powders collected from two locations in the setup. 44
Figure 4.6. Particle accumulation at the cyclone dust pot. 45
Figure 4.7. Actinometry of C_2 intensity to Ar I intensity at 5.5 Torr and 13.7 Torr. 46
Figure 4.8. Actinometry of C_2 intensity to Ar I intensity at increasing pressure. ... 47

Figure 4.9. Actinometry of C_2, CH and H_2 intensity to Ar I intensity at increasing residence time. 49
Figure 4.10. FWHM of $2\Theta = 26°$ peak as a function of operational parameters. ... 50
Figure 4.12. Effect of residence time on Raman spectra. 52
Figure 4.13. Effect of residence time on XRD spectra. 53
Figure 4.14. TGA and DTG curves of particles synthesized with increasing residence time. 54
Figure 4.15. Particle formation with increasing residence time at 30 Torr. 56
Figure 4.16. Size distribution of particles synthesized at 30 Torr. 57
Figure 4.17. HRTEM image of 277 ms synthesized particles at 30 Torr. 58
Figure 4.18. Particle formation with increasing residence time at 50 Torr. 59
Figure 4.19. Size distribution of particles synthesized at 50 Torr. 59
Figure 4.20. Particle formation with increasing residence time at 10 Torr. 60
Figure 4.21. SAED pattern of particles synthesized at 10 Torr and 220 ms. 61
Figure 4.22. SAED pattern comparison of particles synthesized at high residence times. 59

LIST OF ABBREVIATIONS

a-C	Amorphous carbon
AC	Alternating current
DC	Direct current
FWHM	Full-width-at-half-maximum
HACA	Hydrogen-abstraction-acetylene-addition
HCTEM	High-contrast transmission electron microscopy
HRTEM	High-resolution transmission electron microscopy
LTP	Low temperature plasma
nc-G	Nanocrystalline graphite
NEP	Non-equilibrium plasma
OES	Optical emission spectroscopy
PAH	Polycyclic aromatic hydrocarbon
RF	Radio frequency
SAED	Selected area electron diffraction
SEM	Scanning electron microscopy
ta-C	Tetrahedral amorphous carbon
TEM	Transmission electron microscopy
TGA	Thermogravimetric analysis
XPS	X-ray photoelectron spectroscopy
XRD	X-ray diffraction

CHAPTER 1

INTRODUCTION

Carbon is the fourth most abundant element in the universe, coming after hydrogen, helium and oxygen [1]. It can be found as either atomic carbon, carbon-containing molecular compounds that form the basis of organic chemistry, or solid carbonaceous matter [2]. Due to carbon's ability to form either sp, sp^2 or sp^3 hybridized bonds, solid carbon appears as a large compendium of possible configurations that ranges from graphene to graphite, carbon black to carbon nanotubes, and fullerene to diamond. These allotropic forms bring a large library of terminologies with them.

Graphene is a single layer of carbon atoms which are arranged in a 2-D honeycomb crystal lattice [3]. When layers of graphene sheets stack on top of each other in a hexagonal structure, they form a 3-D crystal - called graphite [4]. Diamond, on the other hand, is also 3-D crystalline form of carbon however, instead of a hexagonal structure, carbon atoms are arranged in face centered cubic structure [5]. Carbon nanotubes are rolled-up graphene sheets into cylinders that comprised of either one graphene sheet – single-walled carbon nanotubes or several graphene sheets – multi-walled carbon nanotubes [6]. In fullerenes, carbon atoms are arranged in combination of pentagons and hexagons leading to a ball-like structure. Smallest fullerene contains 20 carbon atoms [7]. Unlike all these special forms, amorphous carbon cannot be classified into single category as the previously mentioned allotropes. Fundamental difference comes from amount of hybridization of sp^2 and sp^3 bonds. Relative proportion of these hybridizations influence crystallinity hence material properties. If sp^2 hybridization is dominant, material is said to be graphitic [8], if sp^3 hybridization is dominant it is said to be diamond-like carbon [9].

Carbon-based materials such as graphitic carbon and nanodiamonds, have attracted significant attention over the past years due to their structural, thermal and electronic properties that enabled them to be used in applications such as energy storage [10], [11], [12], catalysis [13], [14], [15], [16], advanced composite materials [17], [18], [19], quantum computing [20], [21] and bioimaging [22], [23]. For such solid carbon, there are many routes of synthesis, which are either physical, such as the exfoliation of graphite [24], [25], or chemical, such as pyrolysis [26], [27], combustion, chemical vapor deposition [28] or gas-phase conversion [29]. Among these, conversion of simple hydrocarbons into valuable carbon nanoparticles is crucial both economically and environmentally.

The family of hydrocarbons start from methane (CH_4), the simplest saturated hydrocarbon, and extends to heavy oils, commonly used in the synthesis of carbon black. Using the simplest hydrocarbon building block for the production of carbon allotropes is an interesting idea, since CH_4 is abundant in nature and it is inexpensive. Inherently, CH_4 is oxygen-free, thus synthesized particles should not contain oxygenated groups, and it can be acquired in high purity in gas phase unlike acetylene stored dissolved in ketones or alcohols [30].

Due to its stability, however, methane requires a powerful *processor,* in other words, a very reactive environment to enable nucleation and particle growth. An obvious way, is to heat methane up, which is expected to thermodynamically favor dissociation around 900 °C [31]. A carbon-to-hydrogen ratio of 1:4 means a relatively high amount of molecular hydrogen in an environment with even higher temperatures, which can act as an *in situ* reducing agent or a heat source for the background gas [32]. A special medium that can activate methane, split it and produce atomic hydrogen, all without heating the gas is non-equilibrium plasma (NEP). Generating NEP in a reactor offers a powerful and versatile synthesis platform for synthesizing nanoparticles out of gaseous precursors due to highly energetic hot electrons in a cooler bulk gas that favor particle nucleation and growth [33]. Integration of continous-flow configuration with a non-equilibrium plasma would enable a precise control over residence time, along with gas composition and

plasma power, thereby utilizing the basic requirements chemical reaction engineering with the goal of tuning of particle sizes and crystallinity. Particle growth can either be on surfaces [34] or without solid support [35], as demonstrated in flow reactors such as the one shown in Figure 1.1. In the case of growth without support, negative charging of particles prevent aggregation due to Coulombic repulsion [33], which is a unique feature of plasmas. Therefore, particle size distributions are commonly observed to be in NEP reactors when compared to flames and tubular furnaces [36], [37]. The flexibility and capability of NEP flow reactors were demonstrated via the synthesis of various materials, such as Si, Ge, ZnO, Al_2O_3 and GaN [16-18], all in the form of a fine and crystalline powder.

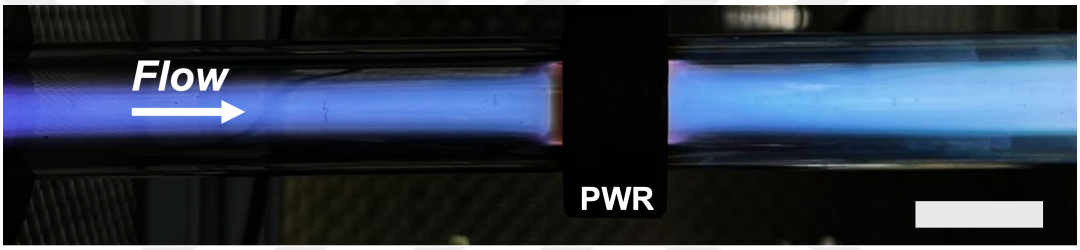

Figure 1.1. A non-equilibrium continuous flow reactor in operation. PWR denotes powered electrode. Scale bar is in 12 mm in width.

Despite the success and progress in making free-standing nanocrystals of metal oxides, and group IV and III-V semiconductors, growth of carbonaceous particles have not yet been explored in detail [40], [41], [42]. The primary challenge comes from the fact that in the pyrolysis of methane, methane chemistry favors rapid film formation on the reactor walls, and particle nucleation can be hindered. Besides low particle yields, breakouts from the films join back the flow stream continuously and decrease the purity of the final nanoparticle product. One of the common solutions to this problem, as detailed in the next section, is switching from methane to acetylene, since the latter favors particle nucleation more than the former [42], [43], [44]. However, acetylene chemistry is different and it is commonly seen to yield low quality carbon materials, especially due to low crystallinity [45]. In this thesis, the formation of the carbonaceous nanoparticles was investigated in a

continuous-flow capacitively-coupled radio frequency non-equilibrium argon/methane plasma reactor.

The effect of operational parameters such as reactor pressure, argon to methane ratio, plasma power and residence time was explored on the crystallinity of in-flight synthesized nanoparticles, thanks to a custom-designed vacuum-compatible Stairmand-type cyclone separator which removes the interference of film breakouts. Therefore, nucleation and the evolution of the particle morphology in the plasma was observable, and produced particulate materials were characterized ex situ through a variety of methods, such as X-ray diffraction (XRD), Raman spectroscopy, thermogravimetric analysis (TGA) and electron microscopy.

CHAPTER 2

LITERATURE REVIEW

In this chapter, classification of carbonaceous nanoparticles was summarized for a better understanding of the structural features, properties and applications. The alternative carbon sources were investigated for both thermal and non-equilibrium plasma-based processes. The fundamentals of non-equilibrium plasma reactors and particle formation mechanism were shown. Finally, the role of continuous flow non-equilibrium plasma reactors in nanomaterial synthesis was given along with the basics of characterization methods for plasmas and carbonaceous nanoparticles. This review provides the necessary background for this study, it identifies the existing research and knowledge and gaps. By putting together the previous work, it provides the rationale and context for the experimental findings discussed in the upcoming chapters.

2.1 Carbonaceous Nanoparticles

2.1.1 Classification and Properties

Carbonaceous nanoparticles are a wide class of carbon materials whose chemical and physical properties strongly determined by atomic bonding configuration and crystallinity. Carbon can exist in a number of allotropes which differ from each other due to the hybridization of the atomic orbitals, sp^2, sp^3 and mixed sp^2-sp^3 states. The unique structural features come from the proportion of sp^2 and sp^3 bonds within the material [46], [47], [48]. Currently known allotropes are graphene, graphite, diamonds, fullerenes, carbon nanotubes and amorphous carbon,

where graphene, fullerenes and nanotubes are inherently nanomaterials, whereas graphite, diamond and amorphous carbon can exist in either submicron or ~mm sized materials. This work mainly focuses on amorphous carbon, graphene and graphite that are allotropes expected to form during transition from gas phase hydrocarbons in a non-oxidizing environment. We will later show that such a transformation occurs also in non-equilibrium plasma reactors when methane is the feedstock.

Graphene is the simplest carbon structure that is a single layer of only sp^2-bonded carbon atoms bound in a honeycomblike structure in two-dimensional domain [49]. It was believed to be not existed due to being such 2D crystal [50]. It was first synthesized as free-standing layers by micromechanical cleavage method, a technique where an adhesive tape is used to peel of the thinnest layer of graphene from bulk graphite [51]. Graphene has exceptional electrical conductivity due to low scattering of electrons [52], and it shows extreme mechanical strength and sometimes regarded as the strongest material ever measured [53]. When graphene layers stack on each other in a hexagonal ABAB layers that are linked with weak van der Waals forces, they form the bulk crystal graphite [54]. Graphite has soft and lubricating properties that come from van der Waals forces between the graphene planes [54]. Van der Waals forces between adjacent layers and the sp^2-hybridized honeycomb network makes graphite an inherently anisotropic material [54]. Crystal structure of graphite is defined by two crystal sizes: L_a in the planar direction (111) and L_c (002) in the stacking direction [55]. Hexagonally stacked graphene sheets in graphite form the (002) planes and are separated by 3.35 Å distance, but the distance between planar (111) and similar planes are at least 40% smaller [56]. Therefore, graphite shares similar electrical and thermal conductivity properties as graphene in the planar direction but not in the stacking direction due to this anisotropy [57].

Amorphous carbon (a-C) is composed of a mixture of sp^2- and sp^3-hybridized orbitals together with varying hydrogen content from 0% to 60% [48]. a-C is referred to as diamond-like carbon when sp^3 bonds are at a significant fraction compared to sp^2 bond, and graphite-like in the opposite case [58]. a-C shows lower electrical and thermal conductivity due to defects in the crystal structure compared to graphite.

Mechanical properties change upon the bonding content of the material: diamond-like carbon shows higher hardness and wear resistance whereas graphite-like carbon shows softer and lubricating properties [9], [59].

2.1.2 Structural Evolution of Carbonaceous Nanoparticles: The Ferrari-Robertson Model

The transition from a-C phases to graphene and graphite is explained by the three-stage model by Ferrari and Robertson [48]. The model describes how carbon nanoparticles structurally evolve upon changing sp^2-sp^3 ratio. In stage 1, a-C can have various forms, as shown in Figure 2.1. Based on the hydrogen content and the extent of dehydrogenation, a-C can either convert into diamond-like carbon, or nanographite (nc-G) in stage 2. In stage 3, graphite flakes can grow into larger crystal sizes.

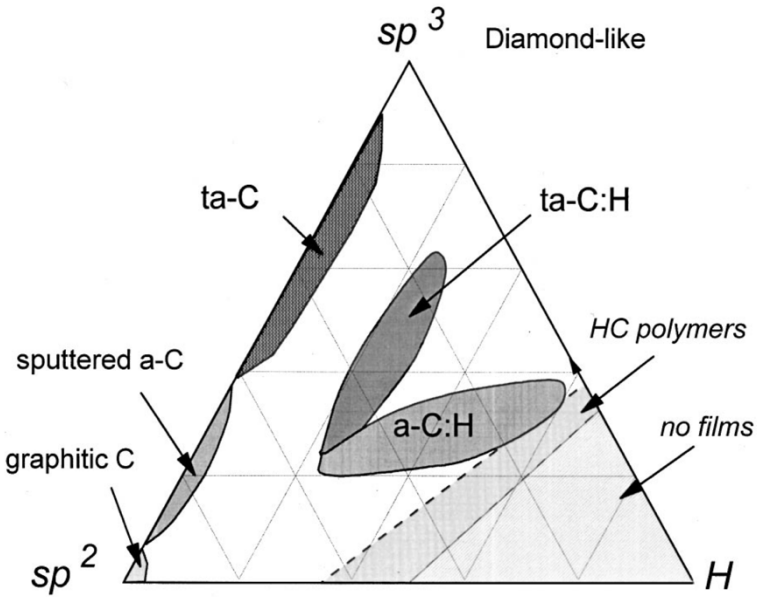

Figure 2.1. Ternary diagram of amorphous carbon based on sp^2, sp^3 bonds and H content. Reprinted figure with permission from A. C. Ferrari and J. Robertson,

Physical Review B, 61, 14095 (2000). Copyright (2000) by the American Physical Society.

In addition to depicting the possible trajectories of carbon evolution on the ternary diagram shown in Figure 1, the Ferrari-Robertson model links the in-plane crystal size, L_a, with Raman spectroscopy. The model extends the framework originally suggested by Tuinstra and Koenig for a-C and graphite [60]. It is closely related to the fundamentals of Raman spectroscopy of the materials, which will be examined in greater detail in the following chapters.

2.1.3 Applications

The structure of the carbon affects its potential uses tremendously. Graphene is used in supercapacitors due to extraordinary electrical conductivity, which enables fast charging [61]. Graphene-silicon composite materials enable ultra-thin batteries with high cycle discharge capacities [62], [63]. Iron- and nitrogen-functionalized graphene is used as oxygen reduction reaction catalyst for microbial fuel cells [64], whereas graphene oxide membranes showed a performance in water purification exceeding reverse osmosis membranes [65]. Unlike graphene, graphite, is one of the oldest materials known, and has been used in industry as lubricants [66], refractories [67] and in carbon brushes of electric motors [68]. High electrical conductivity, low density and corrosion resistance properties of graphite makes it a suitable material for electromagnetic interference shielding [69]. Anisotropic thermal properties of graphite make it function as heat spreader and a partial insulator at the same time [70]. In addition to its uses as a standalone material, graphite performs as a support material as well and is the standard anode material for lithium-ion batteries since it allows reversible intercalation of lithium ions between its graphene layers. [71]. It has a medium to high theoretical capacity of 372 mAh g^{-1} [72]. Graphite is classified into two categories in lithium-ion battery production: artificial and natural. Natural flake graphite performs better than microcrystalline natural graphite and natural

graphite is superior to artificial graphite due to bigger crystal domains [72]. Graphite can be recycled from lithium-ion batteries that have ended their service lives [73].

Due to its complex structure and hydrogenation levels (Figure 1), a-C is expected to have multiple uses. Applications and natural occurrences are predominantly determined by classifying a-C into two major groups, low-crystalline amorphous carbons such as carbon black, furnace black and soot, and high-crystalline amorphous carbons. Carbon black is a reinforcing additive for industrial rubber and tire production [74]. Together with soot-derived materials, they are used as conductive pigments in paints and inks [75]. High-crystalline amorphous carbons are used in battery production similar to graphite but perform poorly when used in lithium-ion batteries, but can outperform in sodium-ion batteries with a capacity of 391 mAh g^{-1} [76], [77].

Diamonds are used in cutting tools due to their exceptional hardness [78]. However, recent studies are focused on doped nanodiamond particles due to their optical features [79]. Nitrogen-doped nanodiamonds are fluorescent with similarities to quantum dots, however, due to non-toxicity fluorescent nanodiamonds are used in bioimaging [80]. One of the configurations of nitrogen-doped nanodiamonds is called NV^- center which has a photoluminescence around ~637 nm [81], [82]. NV^- center's photoluminescence being directly related to its spin state allows it to be used in quantum computing [82]. Such applications require bright NV^- centers that need specific amount of nitrogen doping (in the order of several tens of ppm) and tunable particle sizes [83]. Milling down diamond films harms brightness of NV^- centers due to heterogenous distribution of nitrogen impurities [83], therefore, direct nucleation of these particles from gas phase in to solid particles may be the solution for synthesizing free-standing fluorescent nanodiamonds.

2.2 Synthesis of Carbonaceous Nanoparticles from Gas-Phase Precursors

Solid carbon can be produced as carbonaceous nanoparticles through gas phase decomposition of hydrocarbon precursors. We will focus on the simplest precursors, namely methane (CH_4) and acetylene (C_2H_2). These compounds are widely used feedstock for many gas-to-solid conversion process and they have a rich literature on reaction kinetics, chemistry and particle growth mechanisms. The growth of the solid phase can either be thermal, or non-thermal, i.e. conducted in a non-equilibrium environment.

2.2.1 Thermal Processes

Thermal processes focus on breaking C-H bonds in a high-temperature environment. CH_4 has a high average bond energy of 397.5 kcal/mol, which is also called the enthalpy of atomization [84]. This energy is shared between the four C-H bonds, making each C-H bond energy to 99.4 kcal/mol. Without any catalyst, CH_4 can be cracked around 1400 °C, as demonstrated in moving carbon beds for CH_4 pyrolysis [83]. The need for high temperatures can be reduced with the use of catalysts, to temperatures as low as 500 °C, for example using a Ni catalyst [86]. An interested route is to use molten metals, and by bubbling CH_4 through a molten metal bath at or above 1000 °C, methane can be cracked into solid carbon and hydrogen [87]. In such reactors, hydrogen production is the primary focus rather than carbon production, which stays in the bed and is often contaminated with metals [88]. Unlike these options, thermal plasma-based methods can provide continuous product streams of hydrogen and carbon black [27]. Thermal plasmas are commonly generated with direct current (DC) plasma torches or three-phase alternating current (AC) arc plasmas [31].

In contrast to CH_4, C_2H_2 is highly unsaturated and is mainly responsible for soot formation in combustion processes. Particle formation starts by formation of polycyclic aromatic hydrocarbons (PAH) (Figure 2.2). After these molecules form, they grow by the hydrogen-abstraction-acetylene-addition (HACA) mechanism [89].

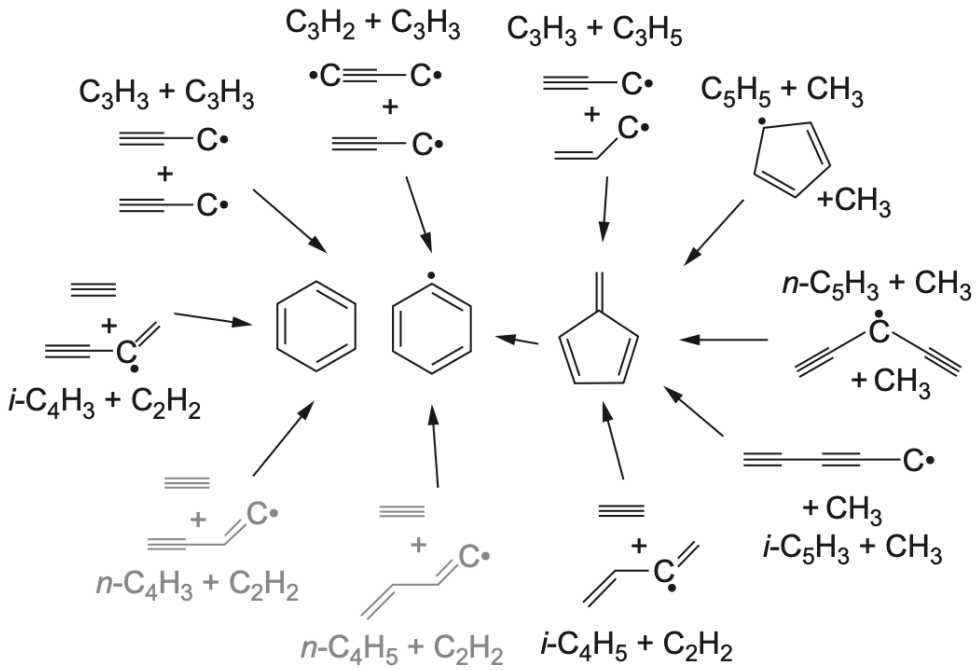

Figure 2.2. Schematic of formation of polycyclic aromatic hydrocarbons. Radicals formed from acetylene and methane precursors. K. Hassouni, F. Mohasseb, F. Bénédic, G. Lombardi, and A. Gicquel, "Formation of soot particles in Ar/H2/CH4 microwave discharges during nanocrystalline diamond deposition: A modeling approach," *Pure Appl. Chem.*, vol. 78, no. 6, pp. 1127–1145, Jan. 2006.

HACA cycles promote the growth of polycyclic aromatic hydrocarbons by first abstracting hydrogen from the PAH with a radical and adding an acetylene to that radical with several repetitions (Figure 2.3). This mechanism leads to formation of turbostratic and graphitic layers when number of these molecules reach 15-20 [27].

For hydrogen-rich precursors such as methane (low C:H) hydrogen is more abundant and more radical termination is needed. Radical sites get quickly saturated which lead to less acetylene addition [90]. This results in slower PAH growth as opposed to efficient PAH growth with hydrogen-poor precursor as C_2H_2. Particles synthesized from acetylene has higher particle sizes compared to methane carbon blacks [91].

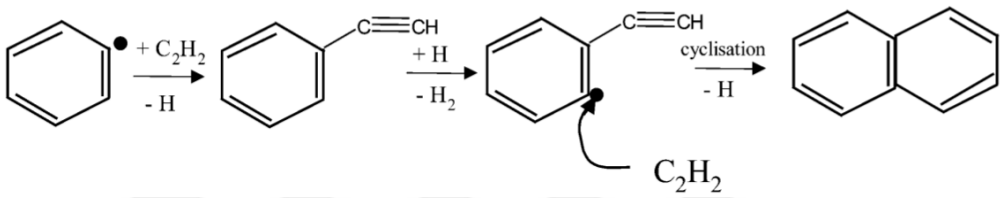

Figure 2.3. HACA mechanism. Growth of polycyclic aromatic hydrocarbon at first cycle. K. Hassouni, F. Mohasseb, F. Bénédic, G. Lombardi, and A. Gicquel, "Formation of soot particles in Ar/H2/CH4 microwave discharges during nanocrystalline diamond deposition: A modeling approach," *Pure Appl. Chem.*, vol. 78, no. 6, pp. 1127–1145, Jan. 2006.

2.2.2 Non-equilibrium Processes

Non-equilibrium processes permit the synthesis of nanoparticles of carbon at significantly low temperatures compared to thermal pyrolysis methods. The predominant route is to utilize a low-temperature, non-equilibrium plasma (NEP), which has highly energized electrons and cooler background gas and ions, hence the thermal nonequilibrium. The extent of nonequilibrium, or the discrepancy between species temperatures, is rather difficult to measure, but seen to affect carbon formation significantly. This can be seen by looking at CH_4 or C_2H_2 conversion in different NEPs. For example, arc discharges and gliding arc reactors operating at atmospheric pressures can produce amorphous particles and graphitic particles [92].

Dielectric barrier discharges, which a gas temperature very close to room temperature, allow methane decomposition but instead of particle formation oligomerization and the synthesis of larger volatile hydrocarbons are favored [93].

On the opposite side, radio-frequency plasmas enable the synthesis of diamond-like carbon films in chemical vapor deposition reactors from acetylene [94]. Both high-hydrogen-content a-C and nanocrystalline graphite can be synthesized with DC discharge chemical vapor deposition reactors [95]. These observations indicate that plasma configuration, plasma parameters, gas temperatures and residence times are crucial in determining the trajectory and products of gas-phase synthesis of solid carbon in NEPs. Therefore, we will elaborate NEPs, their fundamentals and reactors further.

2.3 Non-equilibrium Plasma Reactors and Fundamentals

Nonequilibrium phenomena arises from two complimentary views which are imbalance and instability (Figure 2.4). Imbalance arises locally such as electric voltage difference causing acceleration of charged particles. Instability is more macroscopic view which related to response to perturbations to the system [96].

Non-equilibrium plasmas, also referred as cold or low temperature plasmas (LTP), are capable of synthesizing group IV [97] and III-V [35] semiconductors, metal oxides [98] and pure nanometals from simple precursors. Beyond particle formation, low temperature plasmas are also capable of treatment of the surface morphology, pore structure and surface chemistry of carbonaceous materials [99].

Non-equilibrium plasmas are comprised of highly energized, hot electrons with temperatures in the range 10^4 K-10^5 K (1-10 eV) and cold ions and neutrals that are 300 K-1000 K. In contrast, thermal plasmas operate at local thermodynamic equilibrium where all species are at the same temperature which can be 10000 K or above [100]. Thermal plasmas also contain high concentration of ionized species in

the order of 10^{23} - 10^{28} m^{-3} [101]. However, the fraction of ionized species is low in NEPs, usually between 0.001-0.1% [102].

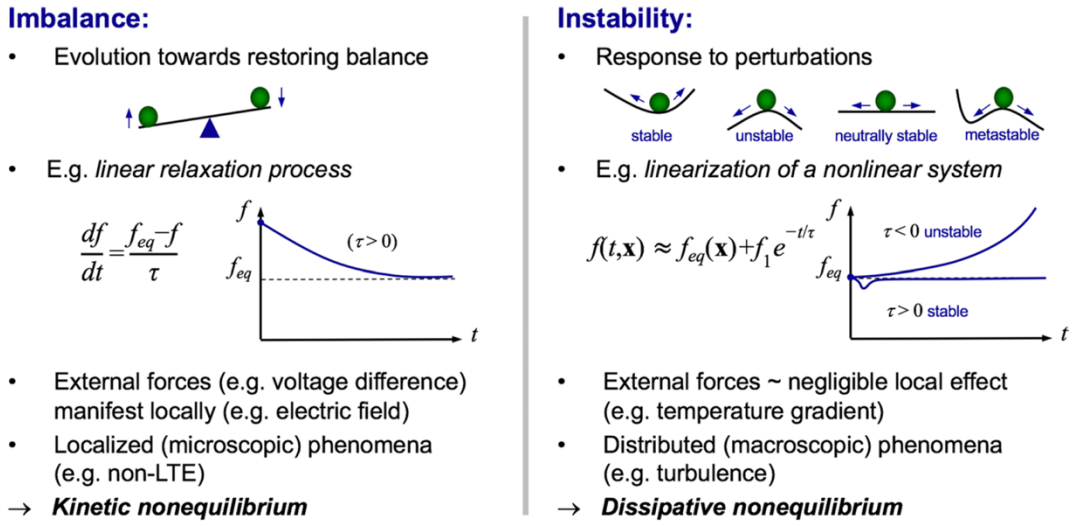

Figure 2.4. Complementary views of nonequilibrium phenomena. Reproduced with permission from Trelles (2020), Plasma Chemistry and Plasma Processing, 40, 727–748, © 2020 Springer Nature [96].

Although the number of ionized species fraction is low, NEPs also contain vibrationally and electronically excited species that can also drive chemical reactions. These reactions take place in various NEP reactors that differ in power delivery, precursor feed and other operating conditions.

2.3.1 Reactor Types

2.3.1.1 Atmospheric Pressure Reactors

Atmospheric pressure non-equilibrium plasmas are cost-effective alternatives to low pressure counterparts due to lack of requirement of vacuum equipment, however, they suffer from a small plasma size. Although the electron-neutral collision frequency of several order of magnitudes higher than low pressure plasmas, atmospheric plasmas have less energetic electrons due to increased collisionality [103]. Increasing size usually requires a significant increase in power, which is also coupled with increasing gas temperature, bringing those plasmas closer to thermal plasmas. For example, a compact non-equilibrium plasma torch process was operated at atmospheric pressure to synthesize carbonaceous nanoparticles with acetylene and ethylene precursor injection [104]. The reactor generated an arc discharge between the electrodes by injecting a high-velocity sweeping gas tangentially, as shown in Figure 2.5. These discharges are sometimes labeled as warm, meaning that they possess both the properties of thermal and nonequilibrium plasmas [105].

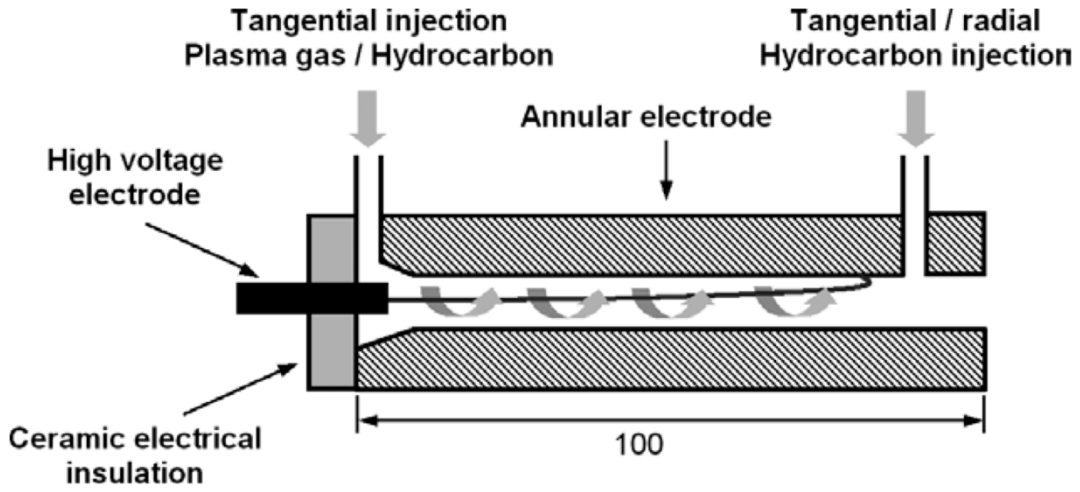

Figure 2.5. Scheme of a compact non-thermal plasma torch for carbonaceous nanoparticles synthesis [104]. © IOP Publishing. Reproduced with permission. All rights reserved.

As another member of this family, gliding arc reactors are increasingly studied reactors which use two blade-shaped electrodes to generate arc cycles. Cycle begins by the inception of the first arc near the minimum gap between the blades. Feed gas, containing precursor and carrier gas, propagates the arc to the end of the blades to make up room for the upcoming arc [106].

Aside from a few torches and arcs, it is also possible to create plasmas with fully nonequilibrium properties at atmospheric pressure. A major example is the dielectric barrier discharges, which can operate at a wide temperature and pressure range. These discharges run with high frequency AC power (1-100 kHz), and power coupling is capacitive through a dielectric covering the powered electrode [107]. When charge is stored in the dielectric barrier within an AC cycle, breakdown occurs due to this charge in the form of numerous short-lived thin filaments. These discharges have enough energy to excite or dissociate molecules [108]. Somewhat similar to the barrier discharges, Coronas are relatively low power discharges take place in the vicinity of atmospheric pressure range. Strong electric fields generate a corona, a zone of ionized gas, usually around small wires and sharp edges [109].

This configuration can be generated with either DC or AC, and they are mainly used for water and air purification processes coupled with ozone generation. [110]

2.3.1.2 Low Pressure Reactors

At low pressure, the mean free path of electrons increases due to reduced collisions with the gas. Accordingly, electrons can accelerate further in a field and achieve higher kinetic energies, i.e. temperatures. Since momentum transfer between electrons and ions or neutrals are inefficient due to a large discrepancy in mass, gas heating is much less. Therefore, a voluminous NEP is easier to form at low pressure, and these low-pressure plasmas are either utilized in batch or continuous flow-through reactors [111]. As an example, for the batch reactor, plasmas can be used to produce Si nanocrystals at a very high excitation frequency of 144 MHz from silane and hydrogen precursors. The process is batch since synthesized nanoparticles are collected as a thin film in a separate vacuum chamber when the desired particle size is achieved [112].

Plasma enhanced chemical vapor deposition reactors (PECVD) are used to deposit films on heated substrate where it is heated to much lower temperatures than that of thermal chemical vapor deposition (Figure 2.6) [113]. Power is typically delivered via radio frequency (RF), microwave (MW) or DC.

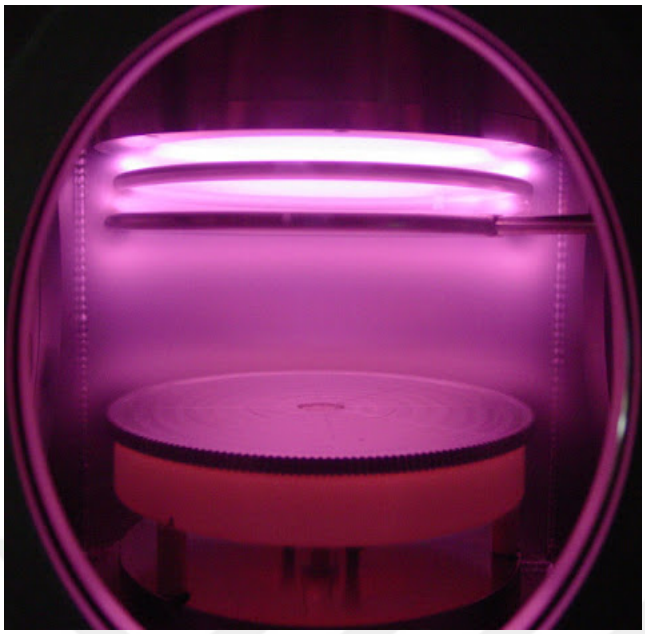

Figure 2.6. Plasma enhanced chemical vapor deposition reactor during operation.

In continuous flow-through configurations, NEPs are generated with radiofrequency (RF) power (>500 kHz), coupled either inductively or capacitively, or microwave (usually 2.45 GHz) power supplies. Inductive coupling transmits power through an inductor wrapped around a dielectric tubular reactor, whereas capacitive coupling is similar to that of a dielectric barrier, that is, the power is deposited at high frequency inside the sheath of an electrode sometimes behind an additional capacitive barrier, only that at low pressure, and hence a uniform glow-like discharge can be formed (see Figure 1.1). Silicon nanocrystals have also been synthesized in all these three power delivery modes with smallest particles synthesized in capacitively coupled RF plasmas and largest particles in inductively coupled RF plasmas [111]. Reactor, i.e. plasma, length is an important parameter in capacitively couple plasmas since particle size is directly related to residence time [114]. Synthesis of sub-10 nm silicon nanocrystals require several milliseconds of residence time in the reactor [37].

2.4 Non-equilibrium Flow-through Reactors for Nanomaterial Production

Flow-through non-equilibrium plasma reactors have gained attention due to their ability to produce high-value semiconductor nanomaterials, metal oxides and alloys directly from gas-phase [115]. These reactors often use microwave or radio frequency power sources. RF power supply is easier to build, simpler and more flexible compared to microwave power supply. Power inputs are in the range of 10^1 - 10^2 W. Power input controls the nanoparticle heating and negative charged particles causing Coulomb repulsion helps achieving narrow size distributions by preventing particles from agglomerating [111]. These reactors capable of synthesizing group IV [97] and III-V [35] semiconductors, metal oxides [98] and pure metal nanoparticles from simple precursors. The formation of these particles is fairly complicated and they are expected to have different chemistry. However, some of the physical processes, such as nucleation, charging and surface growth should be present in the formation of most solid materials. Therefore, the synthesis of silicon nanoparticles is presented below as an exemplary overview of the underlying physical processes in gas-to-solid conversion via NEPs.

2.4.1 Silicon Nanoparticle Formation Mechanism from Silane as an Example to Gas-to-Solid Conversion

Gas-phase synthesis of Si nanoparticles in Si/Ar NEPs is a well-studied process due to discovery of dusty plasmas in electronics processing and need for decreasing the contamination of semiconductors [116], [117], [118].

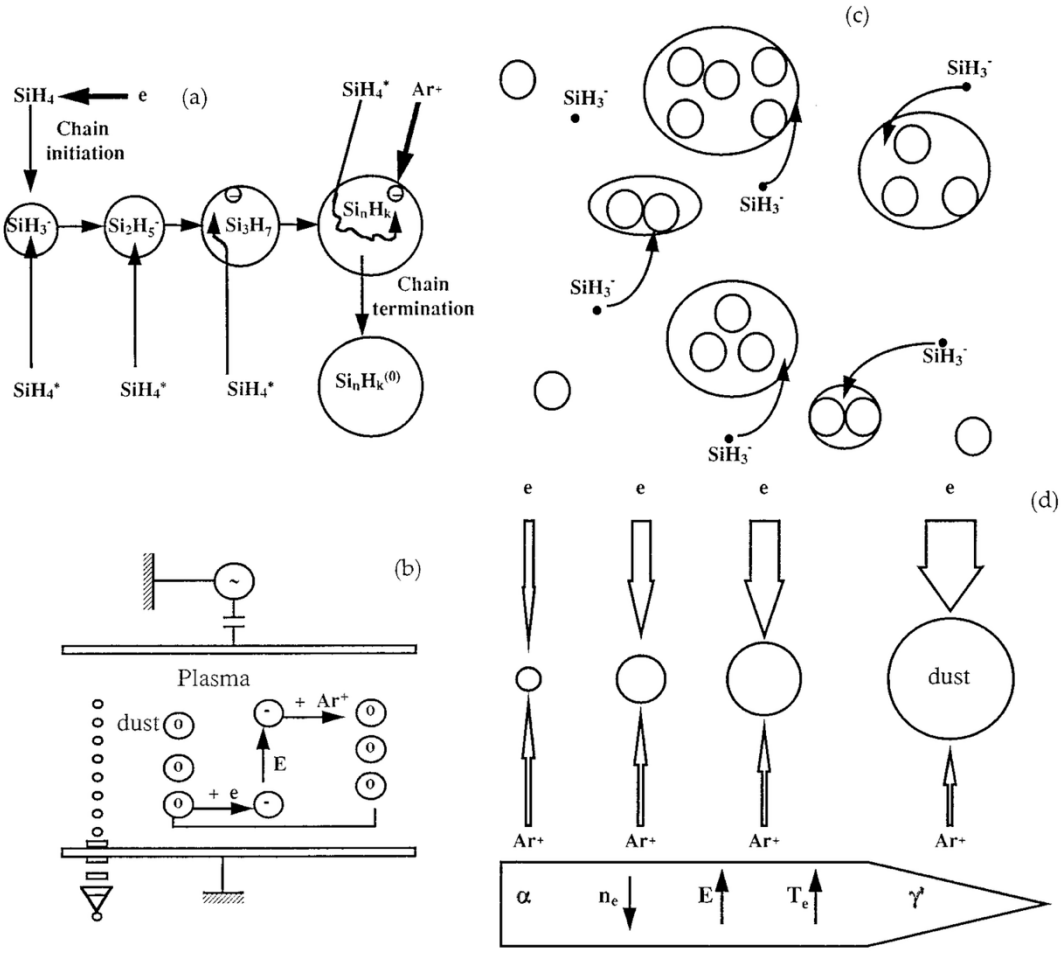

Figure 2.7. (a) Physical scheme of inception of cluster growth. (b) Physical scheme of trapping of neutral particles. (c) Particle coagulation mechanism. (d) Physical scheme of α-transition [119]. Reprinted with the permission of AIP Publishing.

Particle formation in dusty plasmas are categorized into four steps by Fridman et al. [119]: inception of clusters from molecules (kinetic nucleation), selective trapping of neutral particles, coagulation and α-γ transition (Figure 2.7). First step begins with SiH_3^- ion formation by dissociative electron attachment and due to a chain of ion-molecular reactions cluster grows to $Si_3H_7^-$, by a process called Winchester mechanism. Reaction time is in the order of 0.1 ms which is one order of magnitude smaller than time required for ion-ion recombination (1-3 ms), but this time depends on plasma density. Increased size of the negative cluster decreases the probability of reactions with the vibrationally excited species due to relaxation at the

surface. When particle size reaches 2 nm critical size value, ion-ion recombination process becomes more dominant and stops the chain reaction which takes 1 ms at room temperature.

Second step is the selective trapping effect where negatively charged particles are trapped due to repelling forces at the plasma boundary. This depends on flows and therefore on the balance between drag and electrical forces in a flow reactor. Electron attachment time is much longer than ion-ion recombination, thus, only negative particles are trapped. Particles larger than 2 nm are only trapped since particles smaller than 2 nm since they spend less time in the reactor than their attachment time. This step explains why the first grown particles are well-defined crystals.

Third step is the rapid coagulation when the density of 2 nm particles reaches a critical value (10^{10}-10^{11} cm^{-3}) where negative ions such as SiH_3- attach to 2 nm particles since it is faster than generating new particles. Dust formation due to new chains hinder and overall particle mass remains unchanged. At these increased particle density, multibody reactions become more probable.

At the final step, fast charging of discharge parameters takes place when particles get larger and density decreases. When electron losses from the surface of particles become greater than from the reactor walls, the α-γ transition occurs. The transition leads to an imbalance in the plasma and to overcome it the electron temperature rises but its concentration decreases sharply. Negative charging of the particles is explained by this phenomenon (the plasma electron catastrophe) since the effective surface area growing increases the probability of electron attachment to the particles.

Similar mechanism is expected to occur for CH_4/Ar mixtures in RF discharges for the formation of carbonaceous particles, but such a dusty plasma and particle formation mechanisms have not yet been fully modeled [120]. A semi-empirical experimental study would therefore focus on investigating the effects of the tuning knobs of a NEP reactor, which are summarized below.

2.4.2 Operational Parameters

Capacitively-coupled plasma reactors are tuned principally by reactor pressure, input power, power supply frequency, feed gas composition and flow rate, which directly influences residence time.

2.4.2.1 Reactor Pressure

Reactor pressures usually span between several mTorr to 100 Torr in capacitively-coupled flow reactors. Increasing pressure shortens mean free path of charged particles due to enhanced collisions, results in narrow sheaths and increased gas temperature. In addition, at elevated pressures filamentations in the plasma are observed due to either matching network hysteresis [121], or due to the population and energetics of the excited species [122].

2.4.2.2 Power Supply

Through the power supply, power sent into the reactor and sometimes the frequency can be adjusted. Increasing the applied power input increases ionization with higher electron density and reduced sheath thickness [123]. Higher power can therefore elevate production of dust in the plasma while increasing gas temperatures and wall fluxes: migration of species to the reactor walls due to thermophoresis induced by temperature gradient between the gas and the reactor walls.

CCPs generally operate 13.56 MHz frequency, however, high frequency operations up to 200 MHz are also common where higher plasma densities and particle deposition is observed [124]. Higher frequency produces higher plasma density and gives rise to reduced ion bombarding energy which is a requirement for processing of integrated circuits with smaller dimensions [125].

2.4.2.3 Electron Source / Precursor Ratio

Feed to the reactors generally accompanied with inert gases such as Ar, He or rarely Kr [126], [127], that act as electron sources. These gases do not have rotational and vibration degrees of freedom, therefore their plasmas are easier to form and more electrons can be generated at a given power. Because of this reason, dilution of the reactive gas increases nucleation rates, especially in the case of argon, due to a larger number of electrons generated [128].

2.4.2.4 Residence Time

In flow-through reactors, akin to a conventional flow reactor, residence time (τ) defines the amount of time the molecules or particles subject to a reactive environment, and for plasma reactors, the reactive environment is the plasma itself, from which the volume of the reactor can be visually determined. For any flow reactor, the mean residence time can be estimated from the following relation:

$$\tau = \frac{\text{Reactor Volume}}{\text{Total Flow Rate}}$$

At pressures and temperatures other than that of the standart temperature-pressure (STP) conditions, flow rate of a compressible gas needs to be corrected:

$$\text{Actual Flow Rate} = \left(\text{Flow Rate in STP}\right)\left(\frac{T}{T_{STP}}\right)\left(\frac{P_{STP}}{P}\right)$$

The flow rate in STP is the flow rate provided by the MFCs. Residence time can be adjusted with reactor length or flow rate externally, or by reactor pressure and temperature internally in the plasma. Longer exposure to the plasma have generally seen to result in larger particle sizes and more polydisperse particle size distributions in gas-phase synthesis [35], [129]. If residence time of molecules is shorter than the required reaction times for inception of clusters, nucleation does not take place [119].

2.4.3 Advantages and Limitations

There are a number of advantages of flow-through capacitively coupled reactors for nanoparticle synthesis. These reactors enable particle formation from simple precursors, such as silane, methane or aerosols of metals, such as gallium and nitrogen in GaN synthesis [35]. Crystalline nanoparticle formation is possible due to an increase in particle temperatures up to 1000 °C through ion bombarding [37], [130]. Parameter space obtained through the tuning knobs given above allows fine tuning of particle properties and continuous flow enables mg/h to g/h production rates [131].

The limitations to these reactors include the propensity to polydisperse particle size distributions due to broad residence time distribution in laminar flow in tubular reactors [132]. Especially in synthesis involving solid carbon, polymerized by-products deposit on the reactor walls decrease stability of the plasma [133]. Although particles are negatively charged in the plasma, they can still coagulate depending on gas temperature and their number density due to diffusion [134].

2.5 Carbonaceous Nanoparticle Formation in Capacitively-coupled Flow-through RF Plasma

Although an empirical study on solid carbon synthesis with the aforementioned tuning knobs can be conducted, growth of carbonaceous nanoparticles in NEPs is a research area that received less attention and achieved limited success. The main issue faced for this process is the rapid film formation on the reactor walls when CH_4 is used as the precursor, rather than particle nucleation [29]. For this reason, acetylene is used as precursor for the reactions, which has a much higher particle yield. Woodard et al. used an in-situ FTIR analysis to measure the effect of temperature on the graphitization of the carbonaceous particles in an $Ar:C_2H_2:H_2$ plasma operated at 7.5 Torr and 20 W – 100 W [135]. The work claims that particles were heated up to 2000 K in the discharge which led to increased

crystallinity of the material supported with Raman spectroscopy and TEM analysis. It was concluded that future work is needed for describing accurate particle temperature measurements and nucleation pathways for carbon nanoparticles.

A recent work by Belamkar et al. attempted to convert methane into graphitic carbon nanoparticles while emphasizing the difficulty of direct nucleation of particles in methane low-pressure discharges and growth of highly crystallized carbon nanoparticles [29]. The experimental setup uses a two-step precursor feed to the reactor where the first feed nucleates nanoparticles from acetylene or toluene, then the second feed comprised of methane is introduced resulting in synthesis of carbonaceous nanoparticles. First feed and second feed are introduced to two different reactors effectively, using separate power supplies and matching networks. Although particle nucleation and growth are achieved, particles have low graphitization with moderate particle production rate at 200 mg/h.

Another recent work by Nikhar et al. uses Ar/CH_4 plasma in order to synthesize nanodiamond particles [40]. The resulting synthesized particles were amorphous carbon from microscopical and spectroscopic measurements. Since changing various macroscopic reactor settings did not have an influence on diamond formation, laser-induced fluorescence and optical emission spectroscopy measurements were carried out. Results showed strong temperature gradient of 100 K/mm from reactor center to the walls which caused the bulk gas temperature to be not hot enough for nanodiamond formation. The set of experiments were conducted again with the addition of H_2 and no output material was detected, which indicated etching of all sp^2 hybridized material and absence of sp^3 hybridized particles. The hypothesis was supported by replacing RF power supply with microwave source and traces of sp^3 hybridized particles were found.

Prior research has produced carbonaceous nanoparticles in non-equilibrium flow-through plasma reactors, however, a systematic treatment of methane as the carbon source is limited. The main challenges are difficulties in particle nucleation

due to methane being a stable molecule and its proneness to rapid film formation which causes contamination in the final product. Plasma diagnostics were previously used to determine the influence of particle and gas heating on the particle growth but the effect of operating parameters was not investigated properly by common bulk characterization methods in part because *in situ* and *ex situ* analyses are dominated by fragments of film rather than in-flight synthesized particles.

In this thesis, it is aimed to achieve methane conversion into carbonaceous nanoparticles -although direct nucleation of methane claimed to be not possible [29]. Firstly, it is needed to overcome the consequences of film formation by employing a size separation method. Secondly, quantify and develop an understanding for which operational parameters- pressure, power, gas composition and residence time- effect graphitization processes of particles through plasma diagnostics and intensive particle characterization which prelude to nanodiamond synthesis.

CHAPTER 3

EXPERIMENTAL METHODS

3.1 Experimental Setup

The experimental setup used in this thesis was comprised of four main parts (Figure 3.1). These parts are namely the gas feed, the plasma reactor, the particle separation and particle collection units. The entire assembly was mounted on T-slot aluminum frames to maintain integrity of the setup.

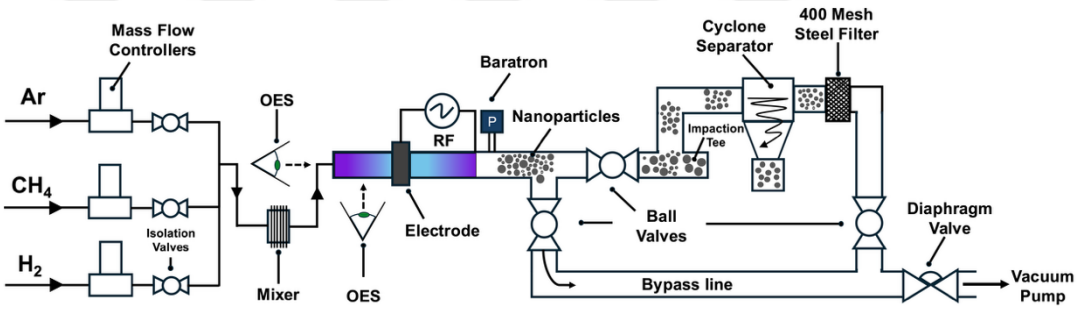

Figure 3.1. **Schematic drawing of the experimental setup.**

3.1.1 Gas Feed

Ultra-high purity argon and hydrogen (99.999%, Ankara Gaz) and high-purity CH_4 (99.995%, Mitan Gaz) cylinders were connected to separate mass flow controllers (MFCs) through stainless-steel 1/4” OD tubing. All cylinders used high-purity pressure regulators (5651, Linde), but the flow paths, flow elements and MFCs for each gas slightly differed. For CH_4 and H_2, flashback arrestors (2601, Yıldız Gaz) were placed to prevent backflow of any gases to the cylinders. 1/4” OD tubings were connected with compression fittings and MFCs were protected upstream via inline

dust filters. CH_4 was connected to an MFC with a flow capacity of 100 sccm CF_4 (model 8161, UNIT Instruments), H_2 was connected to an MFC with a flow capacity of 650 sccm Ar (SEC-E440J, Horiba), and Ar was connected to an MFC with flow capacity of 1300 sccm Ar. Through a two-gas calibration procedure, these MFCs were calibrated for the working gas with a bubble-flow meter. CH_4 had a second MFC (MCE-1, Alicat) with built-in gas correction capability to send very small amounts of gas into the system (1 sccm full-scale range). This MFC was connected to reactor feed manifold with 1/8" OD tubing to fill the delivery lines rapidly and decrease response times at these low flow rates.

All MFCs were powered and regulated through a custom-made Arduino Mega microcontroller chip where the detailed circuit design is shown in Appendix A. The MFC control box containing the microcontroller and electrical elements was placed in a Faraday cage with made with stainless-steel 400 mesh wire gauze to shield the RF signal interference (*vide infra*) from the power supply unit.

3.1.2 Plasma Reactor

Gases were mixed in a chamber containing stainless steel wool to ensure the uniformity of the feed and were sent into a plasma reactor. The reactor is comprised of a fused silica tube with 12 mm OD, 8 mm ID and 200 mm length. The tube was connected to the upstream and downstream metal flanges via KF-16 glass tube adapters, i.e. quick couplings, sealed with graphite O-rings, which were found to be durable and leak-free at high temperatures (> 200 °C). The plasma was generated via a stainless-steel (SS) ring electrode positioned 44.25 mm upstream of the grounded quick coupling. 13.56 MHz radiofrequency power was capacitively coupled to the SS electrode with a power supply (RF-6-XIII, RF VII, Inc) through an automatic L-type network (ATN-10, RF VII, Inc.) to match the impedance. A second Faraday cage was built around the plasma reactor from a 100-mesh wire gauze to provide additional RF shielding (Figure 3.2).

The SS electrode was painted with a high-temperature black paint (690 °C, Motip) to accurately measure its temperature with an IR thermometer (42570, Extech). Such temperature measurements were conducted to implicitly monitor the consistency of power coupling.

Reactor pressure was measured immediately downstream of the grounded quick coupling by using a capacitive diaphragm gauge (Baratron 722C, MKS) and its digital readout was placed in the Faraday cage next to MFC control box.

Two quartz viewports were present in the vicinity of the reactor. The first viewport was installed at the upstream of the fused silica reactor to perform axially integrated optical emission spectroscopy, which was conducted with a fiber-coupled spectrometer (BLACK-Comet-SR, StellarNet Inc.). The second viewport was installed at the downstream of the reactor to observe the plasma length for estimating residence time. During operation the reactor was continuously cooled with two fans positioned above and below the ring electrode.

Solid carbon material leaving the reactor was either sent to a bypass line which was directly connected to a large inline filter and a rotary vane vacuum pump (E2M28, Edwards), or through the line on which a series of particle mobility separation and collection operations were conducted (Figure 3.1).

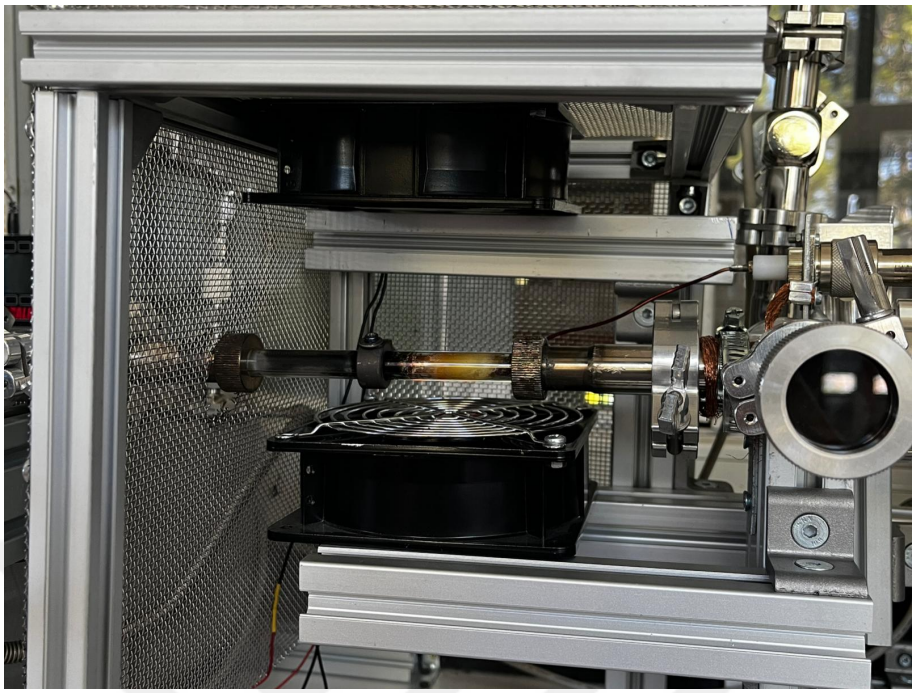

Figure 3.2. **Plasma reactor image with the RF shielding.** Shield protects electronics from interference with radio frequency signal emitted from the powered electrode and the plasma.

3.1.3 Particle Separation

Due to rapid film formation on the reactor walls and continuous detachment of film drop-outs mentioned in Chapter 1, a particle separation method was needed for collection of the in-flight synthesized particles. Particle separation was achieved in two steps by exploiting the differences in mobility of particles since solid film fragments have low mobility and nanoparticle aggregates have high mobility.

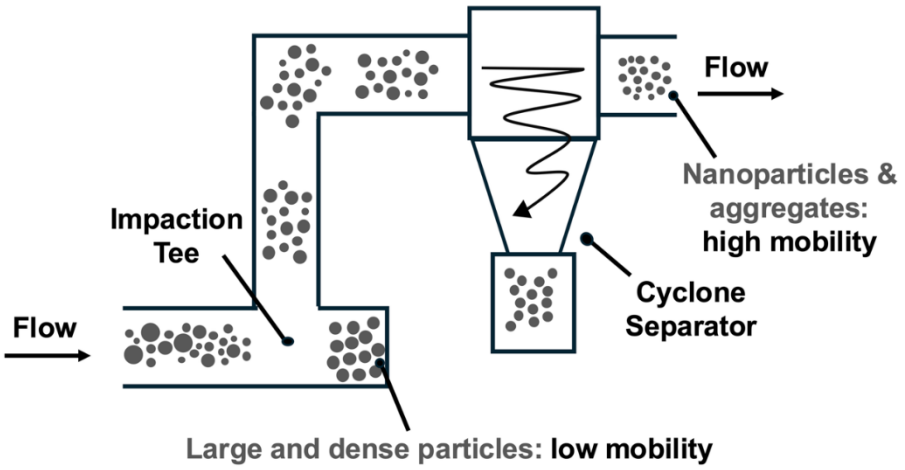

Figure 3.3. Zoomed-in portion of particle separation equipment in the experimental setup. Mobility separation of particles was demonstrated.

At the downstream of the reactor, particles were first subjected to a 90° turn with a tee. Since film drop-outs coming from the reactor walls were solid, large and less mobile than in-flight synthesized particles, their stopping distance was large and therefore they could not follow the flow as easily as the small, in-flight synthesized particles [136]. Most of those drop-outs were deposited at the dead end of the tee via impaction. For further separation of particles, cyclone separation was determined as the most practical and cost-efficient option for vacuum-compatible separation among available particle separation methods such as electrostatic precipitators, wet separators and filters.

A cyclone was machined in-house from aluminum, following a Stairmand-type design [137]. The dimensions are designed such that the cyclone has an expected cut-size of particles in the range of 1-20 μm across a range of flow rates utilized in the reactor. The cyclone was integrated to the experimental setup through KF25 quick coupling flanges and sealed through vacuum-greased threaded connections. The detailed design of the cyclone separator is presented in Appendix B.

3.1.4 Particle Collection

Synthesized particles were collected with help of 400-mesh SS wire gauzes and analyzed ex-situ by a variety of characterization methods (Figure 3.4). For bulk analyses, particles escaping from the cyclone were collected on removable filters made from the SS wire gauzes mounted on KF40 centering rings. The overall collection efficiency of filters was measured 73% by mass through experiments conducted for different flow rates. Measurements and experiments for determining particle this collection efficiency are presented in Appendix C.

The carbonaceous powder collected on the filters were scraped off and stored in 1.5 mL Eppendorf vials. Characterization of the powder was made in dry form via XRD, Raman spectroscopy, SEM and TGA.

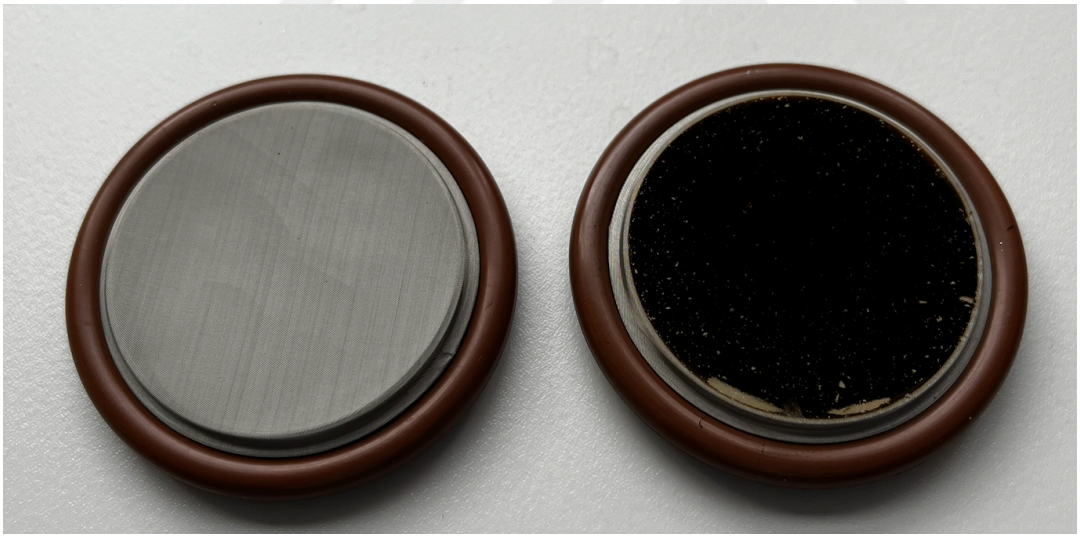

Figure 3.4. Removable 400-mesh stainless steel wire gauzes. Left: clean filter; right: particle deposited filter.

For TEM sampling, filtering assembly was slightly modified. 400-mesh stainless steel wire gauze was mounted in smaller KF25 centering rings. To capture the in-flight synthesized particles directly on the TEM grid; first, a small square of double-sided tape was applied to the filter followed by the equally sized sticky note with adhesive facing outward. Carbon film-supported, 300-mesh copper TEM grid was installed halfway to the sticky note piece, protecting the carbon film during installation and removal (Figure 3.5). This assembly was placed downstream of the cyclone, and particles deposited on the TEM grids via diffusion [35].

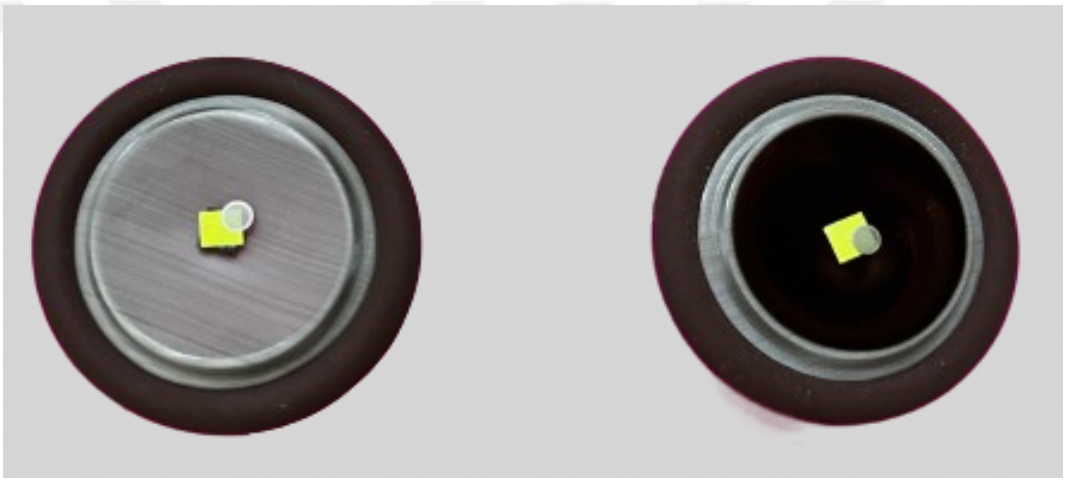

Figure 3.5. TEM grid installed removable mesh filters. Left: clean, right: particle deposited filter.

3.2 Powder Characterization Methods

3.2.1 X-Ray Diffraction

X-ray diffraction (Miniflex, Rigaku) was conducted by placing the synthesized powder on a low background silicon sample holder. XRD patterns were collected from 10° to 90° 2Θ at scan rate of 2° per minute. The full-width-at-half-maximum (FWHM) of the diffraction peaks were measured by subtracting the background signal coming from the silicon sample holder first and then applying a smoothing algorithm to the XRD spectra so that the half maximum can be accurately determined.

Degree of graphitization ($\bar{g}$) was calculated using the following relationship by Seehra and Pavlovic [138]. d_{002} is in A and found by Bragg equation using XRD spectrum using x-ray excitation wavelength and peak angle where diffraction occurs.

$$\bar{g} = \frac{3.440 - d_{002}}{3.440 - 3.354}$$

$$d_{002} = \frac{\lambda}{2\sin\Theta}$$

3.2.2 Raman Spectroscopy

Raman spectra were collected under 532 nm laser excitation (inVia, Renishaw) on at least three different locations for every powder sample. Smoothing and baseline correction algorithms were applied to the spectra. From the resulting refined spectra, intensity ratio of the D band (~1350 cm^{-1}) to G (~1580 cm^{-1}) band, i.e. I_D/I_G, was calculated. I_D/I_G is particularly important because D band arises from the defects and disorder in carbon atoms whereas G band arises from stretching of sp^2 C-C bonds which directly related to graphitization of the material.

3.2.3 Thermogravimetric Analysis

Powders were subjected to thermogravimetric analysis (DTG-60H, Shimadzu) to assess their thermal stability and to infer about the carbon structure of the particles. Samples were heated from 20 °C to 1000 °C with a temperature increase of 2 °C per minute under 50 ccm air flow. Temperature derivative of mass loss curve was obtained using a finite-difference algorithm.

3.2.4 Optical and Electron Microscopy

Optical microscope images of removable stainless-steel filters were acquired using a biological microscope (No. 1864, Southern Precision) with 4× and 10× zoom lenses and equipped with a generic 5-megapixel CMOS camera. Scale bars of the images were prepared using calibration slides.

Scanning electron microscopy was performed on scraped-off powder samples prepared on carbon-adhesive tapes. 20 kV accelerating voltage and 125× to 500x magnification were used (SEM, Vega, Tescan).

Transmission electron microscopy (TEM) was performed on 300-mesh carbon film-supported copper grids. Particle and aggregate morphologies were examined using a high-contrast transmission electron microscope (HCTEM, Tecnai G^2, FEI) with a LaB_6 filament operated at 120 kV accelerating voltage. Particle sizes for particle size distributions were measured using ImageJ software from images taken from multiple spots on the grid. At least 130 particles were sampled for obtaining size distributions.

Lattice fringes were imaged with a high-resolution transmission electron microscope (HRTEM, JEM-2100F, JEOL) equipped with a Schottky-type field emission gun at 200 kV accelerating voltage. Crystal lattice dimensions were measured via ImageJ software.

3.3 Plasma Diagnostics

Optical emission spectroscopy (OES) is a commonly used diagnostic tool which analyzes the light emitted by excited species in a plasma due to electron impact excitation followed by relaxation to a lower energy state. Analysis of the photon energies can be used to infer the composition of the emitting medium [139]. In addition to being non-intrusive and inexpensive, OES can be easily integrated to existing plasma processes. It can provide information about the plasma quantitatively, however, qualitative uses of it are common. For example, it can be used as a *fingerprint* for a process operating at its set point, and measurements can be compared to this reference for process control.

OES was performed from the quartz viewport located at the upstream of the reactor for axially integrated spectra. The collimating lens of the fiber spectrometer was aligned in line to the central axis of the fused silica reactor (Figure 3.6, configuration 1). Radially integrated and axially resolved emission spectra were also collected, at 5-mm intervals along the reactor axis (Figure 3.6, configuration 2).

Actinometry [140] was used to qualitatively estimate the relative concentrations of excited species in the plasma such as CH, C_2 and H-α Balmer line. Swan band emissions (Figure 3.7) [141] of CH, C_2 and H-α Balmer line were monitored using the Ar I emission at 811.5 nm as the actinometer that served as a reference for normalizing the emission intensities.

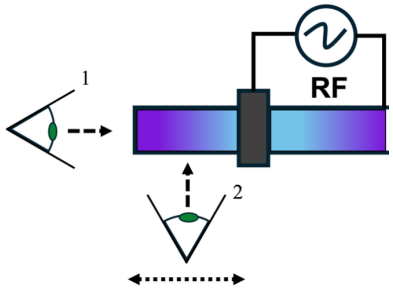

Figure 3.6. Configurations of OES. The eye stands for the collimating lens that collects the emitted light. Configuration 1 is the axially integrated, and configuration 2 is the radially integrated, axially resolved setup for acquiring spectra.

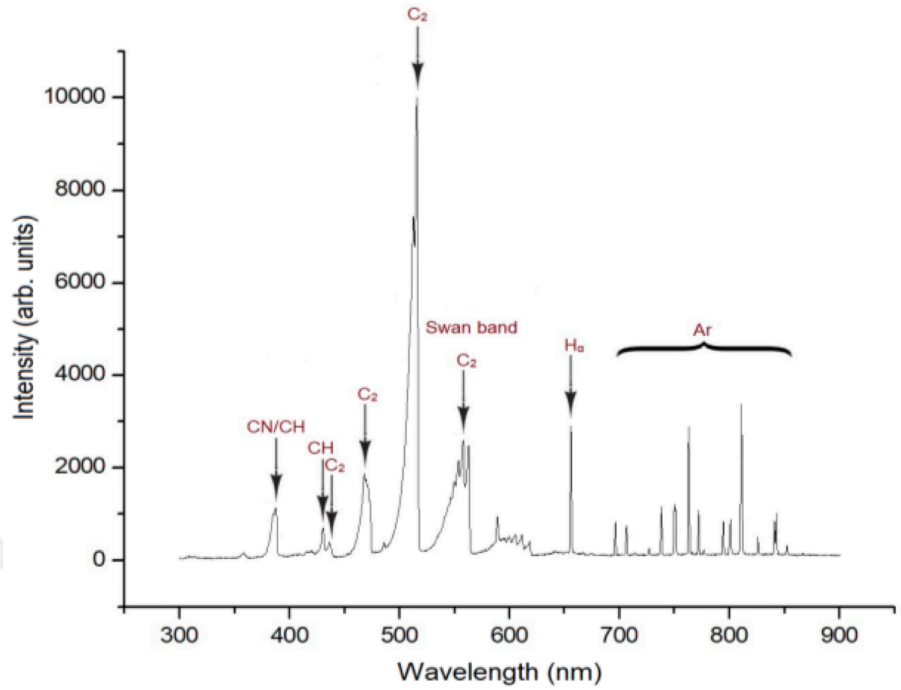

Figure 3.7. Optical emission spectrum showing Swand bands and argon emission lines [142].

CHAPTER 4

RESULTS AND DISCUSSION

4.1 Particle Separation Performance

During the operation of the plasma reactor, a carbonaceous thin film appeared on the reactor walls due to deposition of PAHs. Thickness of this film varied along the reactor axis, thicker in some parts and thinner in others as evidenced by greenish, brownish and black colors in Figure 4.1. As the operation continued, parts of the film, with sizes of hundreds of microns, continuously detached and joined the flow with the in-flight synthesized particles. Due to order of magnitude differences in residence time of the particles, detached particles caused contamination in the final product.

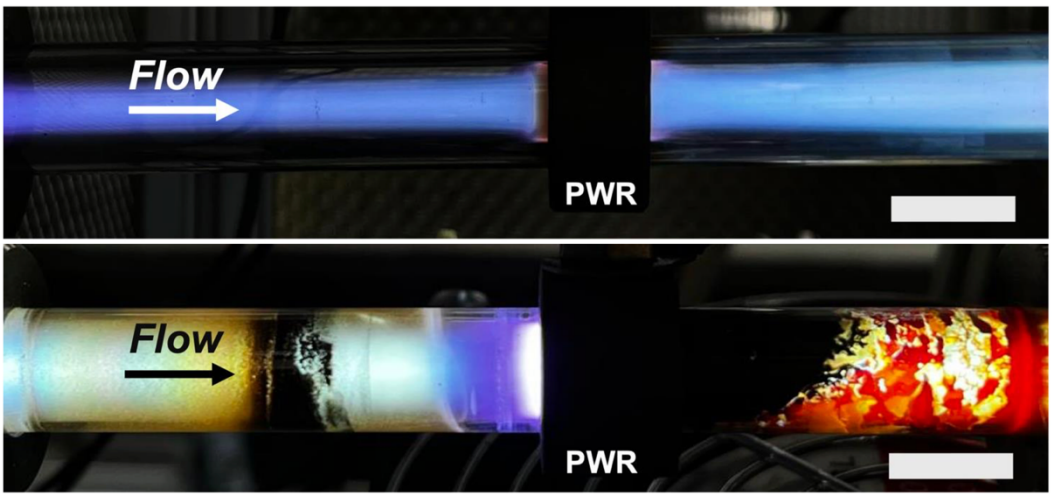

Figure 4.1. **Plasma reactor images.** Top image: Pristine quartz plasma reactor at the beginning of the synthesis, bottom image: contaminated reactor walls after several hours of operation. PWR signifies the powered electrode. Scale bar is in 12 mm width.

A two-step mobility separation was applied to the particles prior to collection. Performance of the separation of particles was evaluated by placing removable stainless-steel mesh filters at three different locations in the setup; upstream of the impaction stage, upstream of the cyclone and downstream of the cyclone. Particles collected on these filters were examined under optical and electron microscopy. Pressure drop (ΔP) for the system was calculated 0.90 Torr for 2 meters of flow length from Hagen-Poiseuille equation for an average flowrate of 600 sccm and at 30 Torr. ΔP between the filter locations corresponded to 50 mTorr. ΔP in the cyclone separator was calculated ~5.5 mTorr from Euler number of 46, which was selected in the design process. Therefore, from the beginning of synthesis to collection, pressure drop was kept constant during particle collection.

Optical microscope image of the filter placed at the upstream of the impaction stage (i.e., at directly downstream of the reactor) showed (Figure 4.2) that there were particles visible even at 4× magnification. Visible particle sizes were in the range of 500 microns down to several microns. SEM image of the scraped off particles from the same filter were in agreement with the optical micrographs, showing several hundreds of microns sized particles at 125× magnification.

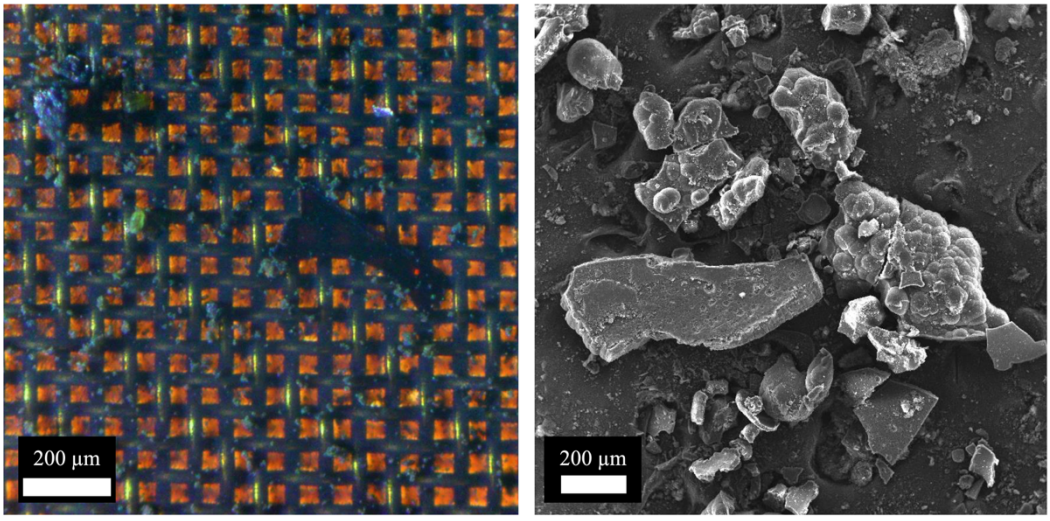

Figure 4.2. Particles collected at the upstream of the impaction stage. Optical microscope image on the left, SEM image on the right.

For the first step of particle separation, removable mesh filters were placed to the upstream of the cyclone (i.e., downstream of the impaction stage). Optical microscope image revealed (Figure 4.3) no evidence of the hundred-micron sized solid particles, though coarse particles remained visible at 4× magnification. Carbonaceous powder was much finer with particles of 50-micron size at 500× magnification under SEM. Aggregates were now visible under TEM, showing a 10-micron sized agglomerate, which also revealed much smaller particles in the background.

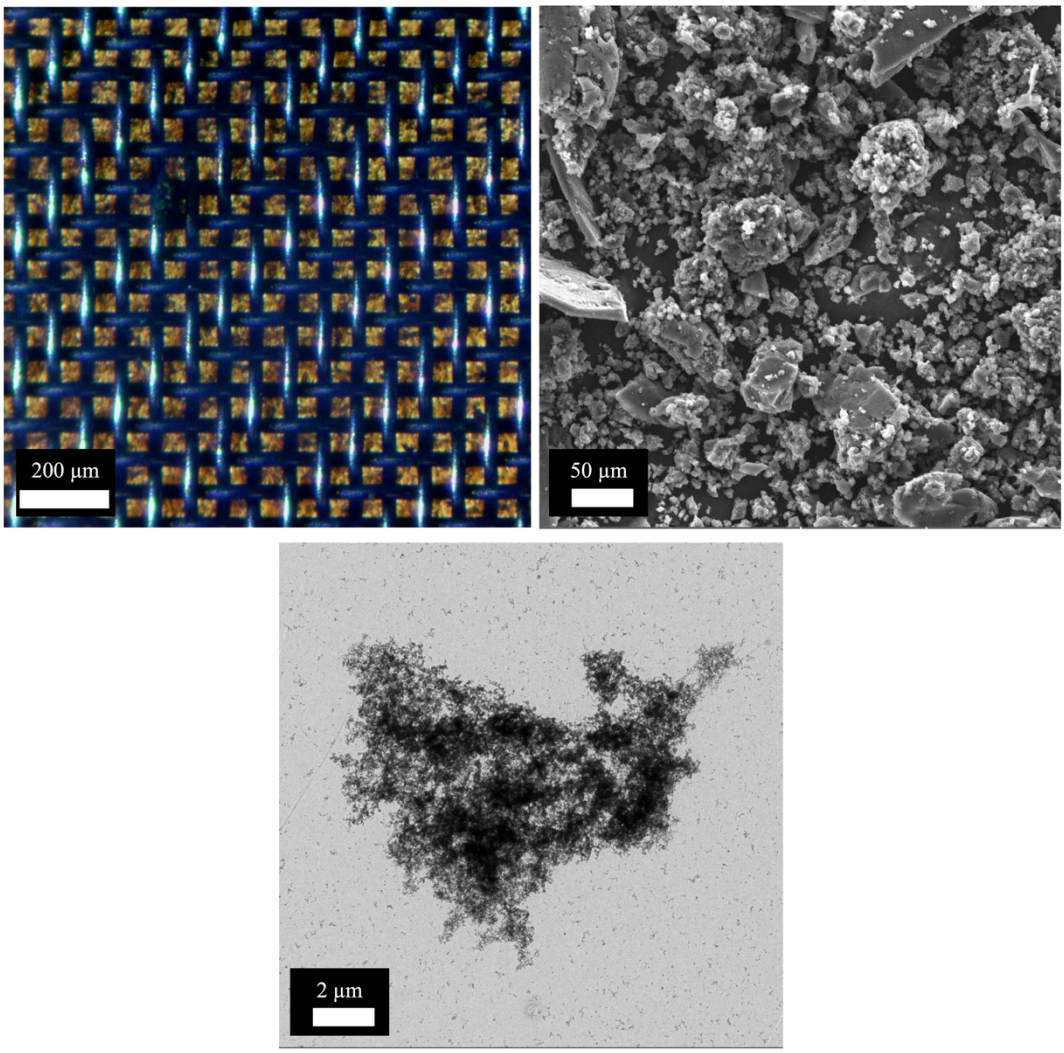

Figure 4.3. Particles collected at the upstream of the cyclone. Optical microscope image on top-left, SEM image on top-right, TEM image at the bottom.

The removable mesh filter placed at the downstream of the cyclone did not contain any visible solid and large particles under optical microscope. SEM image of the particles showed nothing but a fine powder or carbonaceous particles in submicron size. TEM image contained only several hundred nanometer sized agglomerates. From these particles, it was possible to obtain a selected area electron diffraction (SAED) pattern with concentric rings.

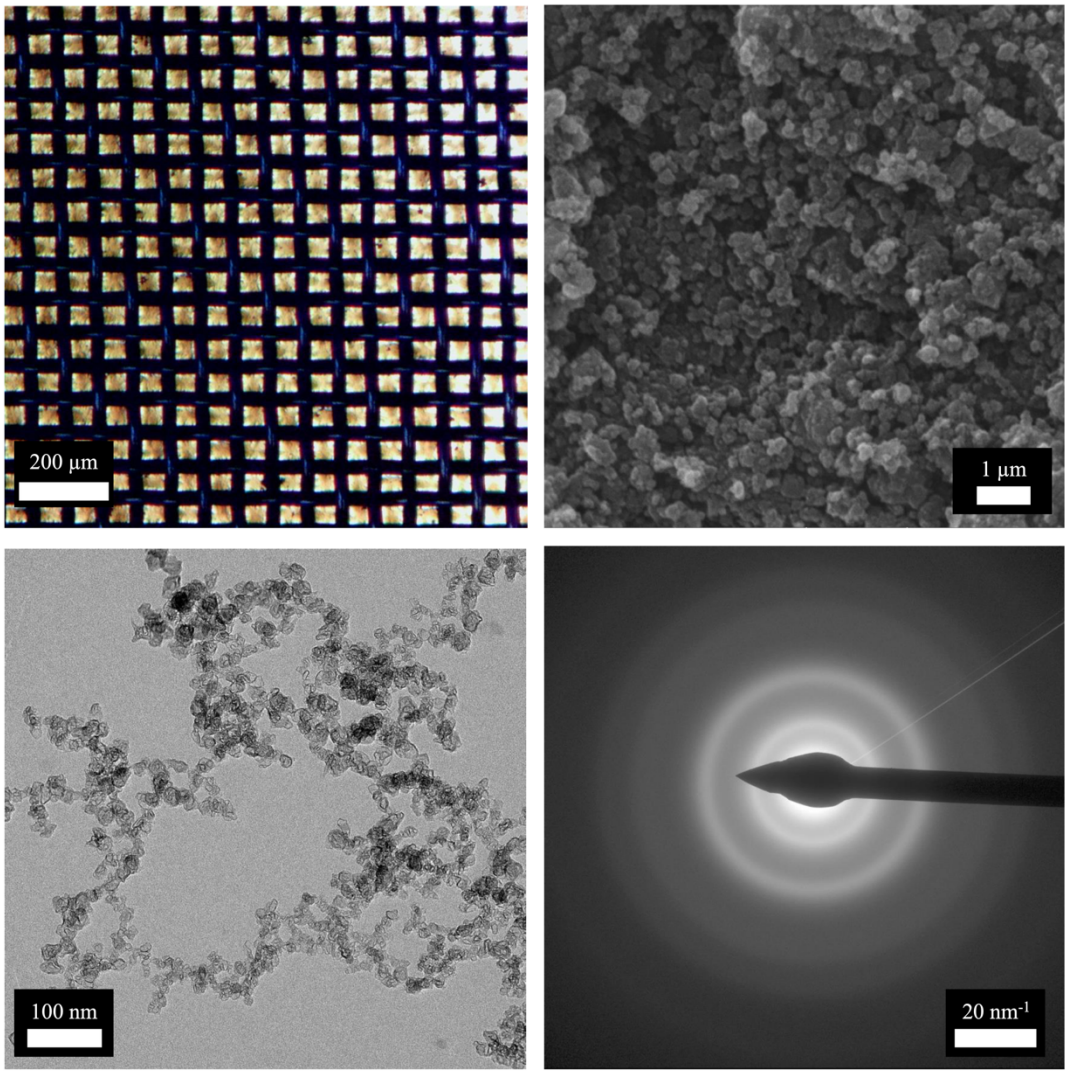

Figure 4.4. Particles collected at the upstream of the cyclone. Optical microscope image on top-left corner, SEM image on top-right corner, TEM image on bottom-left corner, SAED image on bottom-right corner.

Filter images taken at successive locations in the experimental setup verified impaction stage and cyclone separator were operated as mobility separators. Furthermore, TGA performed on powders collected from upstream of the impaction stage and downstream of the cyclone also showed a clear difference. Particles coming straight from the reactor at the upstream of the impaction stage showed three peaks in derivative thermogravimetry (DTG) curve indicating three mass loss events, hence three different types of carbon, shown in Figure 4.5. By contrast, size separated particles had a single DTG peak with small shoulders, clear evidence of more uniform powder chemistry. This result showed that the cyclone not only performed particle separation, but purified the product. Shoulders of this peak were on the two sides which implied poorly graphitized polycyclic aromatic hydrocarbons around 350 C° and highly graphitized particles around 600 C°, possibly came from the wall film beneath the powered electrode, which is subjected to the plasma with high temperatures and ion bombardment rates. TGA curve of unpurified particles were not fully oxidized at 1000 C°, possibly due to contamination related to residual carbon from incomplete combustion or fragments of reactor material, likely fused silica, that are thermally stable.

Successful operation of the cyclone was also evidenced by the particle accumulation at the bottom of the cyclone shown in Figure 4.6.

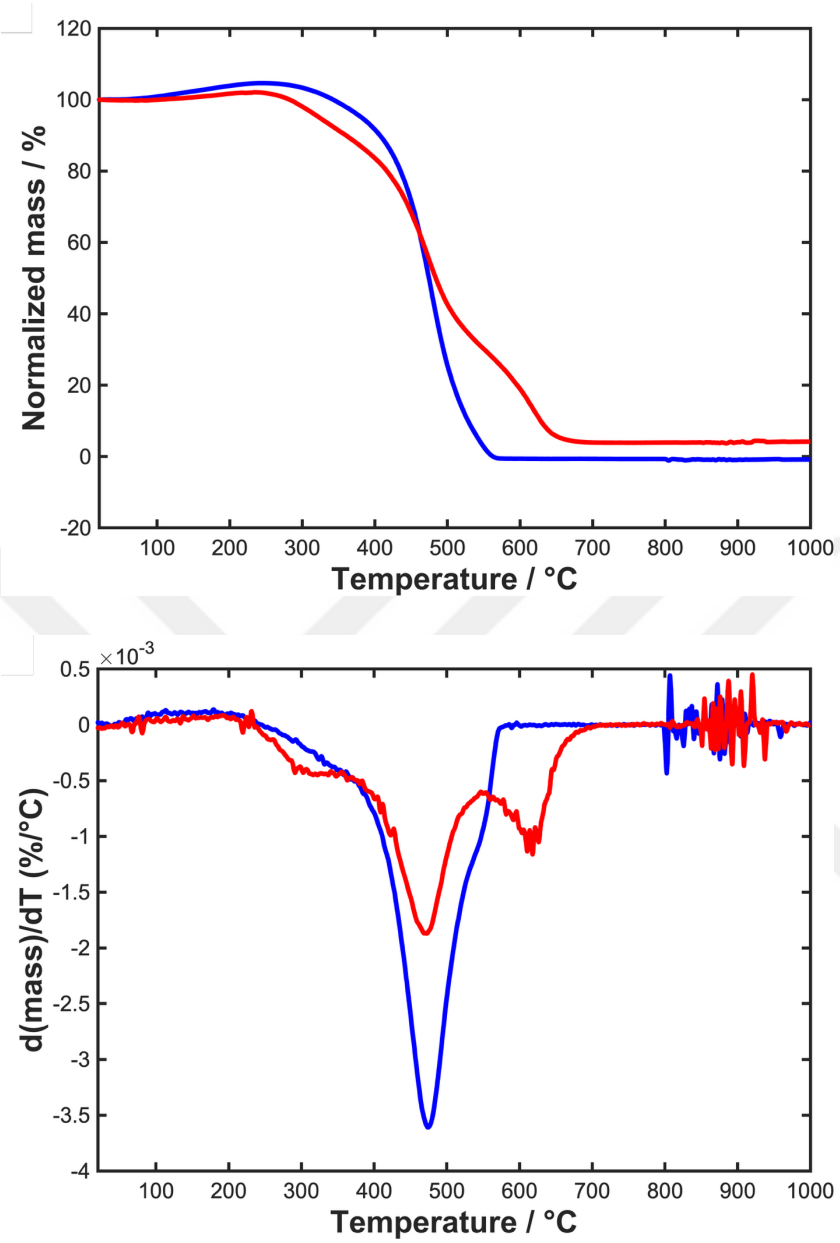

Figure 4.5. TGA and DTG curves of powders collected from two locations in the setup. A: TGA curve and b: DTG curve where blue color is for particles collected at the downstream of the cyclone and red color is particles collected at the upstream of impaction stage.

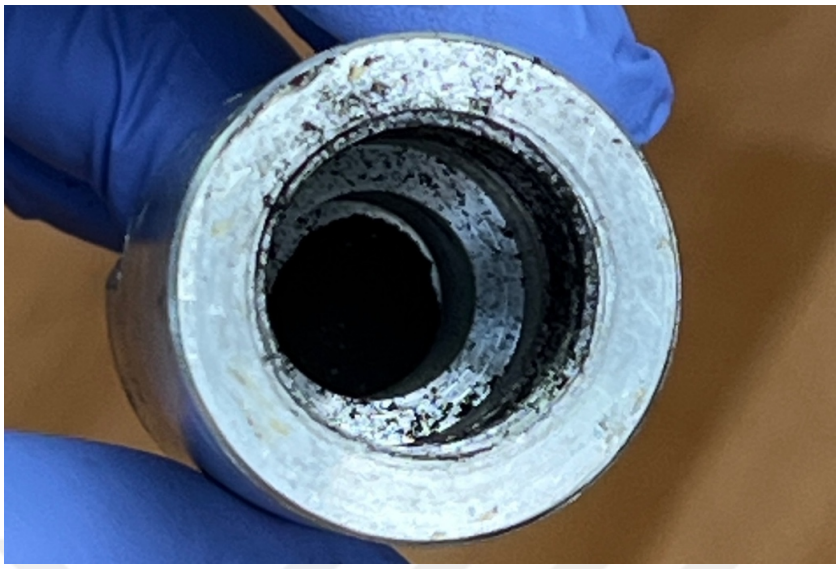

Figure 4.6. Particle accumulation at the cyclone dust pot. Middle sized particles were collected in the cyclone.

4.2 Effect of Reactor Pressure and Residence Time on OES

Optical emission spectroscopy was carried out to track the forming of Swan bands during synthesis. Predominantly, a broad emission spectrum of CH (429 nm) and C_2 (514 nm) lines coming from Swan system [141,142], H-α emission (Balmer-α, 656 nm) [144] and Ar I lines [145] were observed.

OES spectra were collected at two pressure settings to the determine an optimum operating pressure direction for future experiments. Since presence of the C_2 peak indicated dissociation of methane and forming of carbonaceous particles, by selecting the Ar I emission at 811 nm as the actinometer, C_2 peak intensity to argon peak intensity ratios were calculated for every 5 mm point along the reactor length. At relatively high pressure of 13.7 Torr, C_2-to-Ar ratio was higher compared to lower pressure of 5.5 Torr in all axial positions (Figure 4.7). This indicated that methane dissociation was started before the electrode and most C_2 species were transformed into particles after they passed the powered electrode due to high plasma density - also evidenced in Figure 4.1. Film formation occurred mostly downstream of the

powered electrode due to inadequate negative charging of small molecules, which led to electrostatic attraction of these molecules to the negatively charged reactor walls.

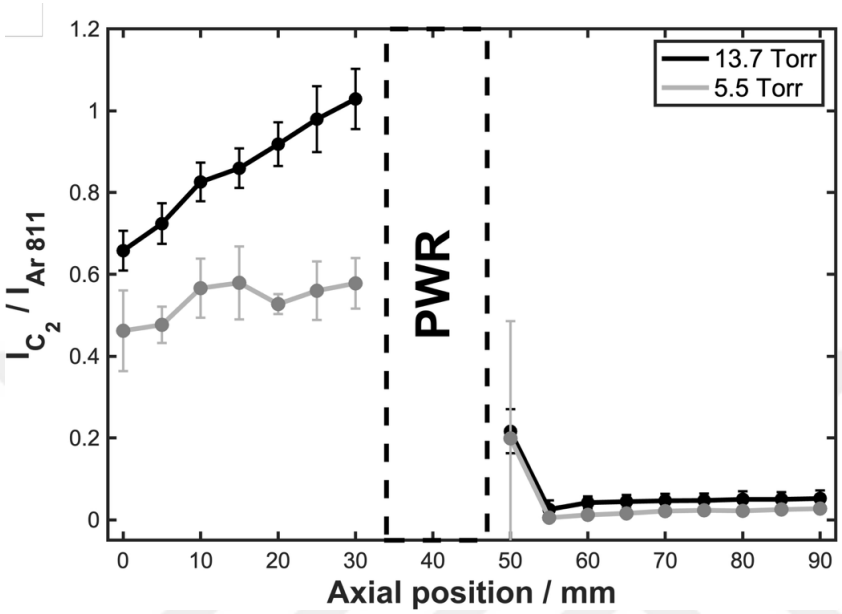

Figure 4.7. Radially-integrated actinometry of C_2 at 5.5 Torr and 13.7 Torr. Experimental parameters: 135 W plasma power, 15 sccm CH_4, 600 sccm Ar.

Although radially-integrated OES initially yielded useful information when used with a clean tube, measurements drifted rapidly with increased runtime due to film formation, which reduced the intensity of light emitted from the plasma. Therefore, axially-integrated OES measurements were conducted from the quartz viewport in-axis with the reactor to reduce the effects of film deposition. Axially integrated actinometric ratio of C_2-to-Ar increased steadily up to 40 Torr, then declined at 50 Torr, potentially due to decreased power and electron density at higher pressure (Figure 4.8). In summary, both axially and radially integrated spectra indicated enhanced performance at high pressures.

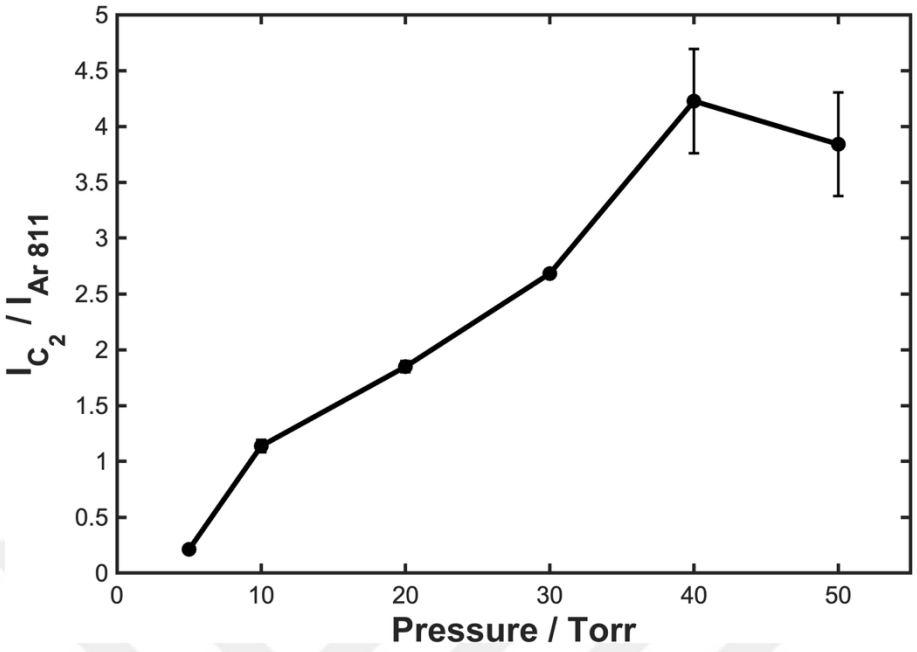

Figure 4.8. Axially-integrated actinometry of C_2 as a function of pressure. Experimental parameters: 135 W, 15 sccm CH_4, 600 sccm Ar.

Upon selecting the reactor pressure, one important parameter, residence time, in flow-through plasma reactors was investigated via OES in axially integrated fashion (Figure 4.9). Actinometric ratio of C_2-to-Ar and CH-to-Ar exhibited a steady decrease up to 46 ms mean residence time. However, both ratios exhibited a sudden increase at 139 ms and showed a gentle decrease toward 544 ms. The unusual change in the trend with increasing residence time was not associated with any particle formation as particle formation rates were unchanged. However, it was observed that film formation on the reactor walls was negligible at residence times larger than 139 ms.

It was hypothesized that film formation and particle formation are two competing processes, and longer residence times favor the latter over the former. Similar to thermal carbon black process [146], residence time is analogous to temperature in a sense that as residence time increases, PAHs undergo dehydrogenation, which results in more crystalline particles, and less film deposition is expected. Here, we see that deposition is generally low upstream of the powered

electrode, and concentrated downstream of the powered electrode (see Figure 4.1). This observation, and the fact that downstream deposition is slowed down at high residence times indicate that processes at the intense zone covered by the powered electrode is playing a major role. Within this zone, PAHs are expected to form due to the presence of the Swan bands and C_2 formation upstream. If the residence time is low within this zone, which is known to have significantly higher plasma densities then the rest of the plasma upstream and downstream [147], PAHs and their fragments may get positively charged upon ion bombardment, and may subsequently deposit on the downstream walls. This deposition is expected to proceed rapidly with help of electrostatic interaction, since walls of a plasma reactor is expected to become negatively charged. However, for sufficiently long residence time within this zone, particle nucleation can happen, which can decrease deposition significantly. Therefore, we see the trench around 50 ms in Figure 4.9 as the minimum residence time required for particle formation withing the powered electrode. Up to this point, there is increased loss of small carbon compounds, but after, only the vapor, CH and C_2 species that is generated from the particles is observed. The amount of that vapor increases first, but then decreases as residence time gets longer, due to diffusion similar to low residence times. The hypothesis was supported with constant increase in H_2 concentration in the plasma, where synthesized particles continued losing hydrogen under ion and electron bombardment within the plasma downstream of the powered electrode.

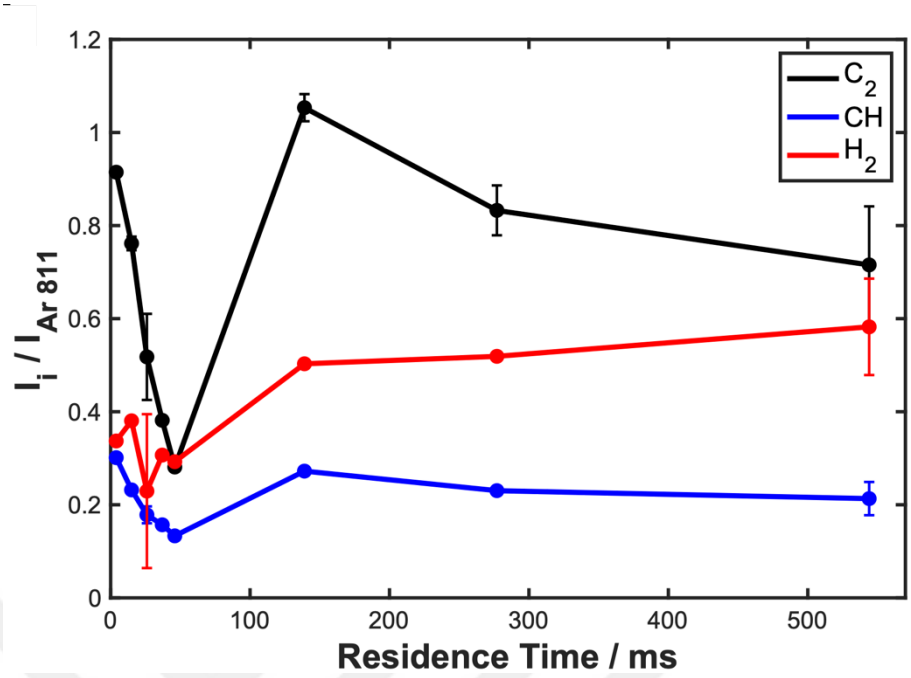

Figure 4.9. Actinometry of C_2, CH and H_2 intensity to Ar I intensity at increasing residence time. Operating conditions: 200 W, Ar/CH_4 = 40, 30 Torr.

4.3 Investigation of Particle Formation via Bulk Characterization

To compliment and further improve the findings from plasma diagnostics, the synthesized powders were subjected to extensive *ex-situ* characterization. These analyses were crucial for establishing an understanding of how morphology and structural ordering of carbonaceous particles change under different operational parameters such as pressure, plasma power, Ar/CH_4 ratio and residence time through XRD, Raman and TGA.

Variations in particle crystallinity with operational parameters were investigated with XRD. The (002) plane at $2\Theta = 26°$ was analyzed since it is the strongest peak for graphite. The full-width-at-half-maximum (FWHM) is inversely related to L_c via Scherrer equation (Equation-1) [147-149]. K is a dimensionless shape factor, λ is the x-ray wavelength, β is FWHM and Θ is the Bragg angle.

$$L_c = \frac{K\lambda}{D\cos\theta} \qquad \text{(Equation-1)}$$

At fixed pressure (20 Torr) and electron source/precursor ratio (Ar/CH_4 = 40), increasing plasma power increased the crystallite size increased from 0.60 nm to 0.85 nm (Figure 4.10-a). Similarly, at fixed pressure (20 Torr) and plasma power (200 W), increasing Ar/CH4 ratio increased the crystallite size from 0.66 nm to 1.07 nm (Figure 4.10-b). The change in FWHM for both conditions were ~5°. However, the most dramatical change was observed upon changing reactor pressure at fixed plasma power (150 W) and (Ar/CH_4 = 40), FWHM decreased from 17.5° to 6.5° which corresponded to crystallite site increasing from 0.49 nm to 1.31 nm (Figure 4.10-c). Crystallite size slightly decreased at 30 Torr due to decreased plasma density

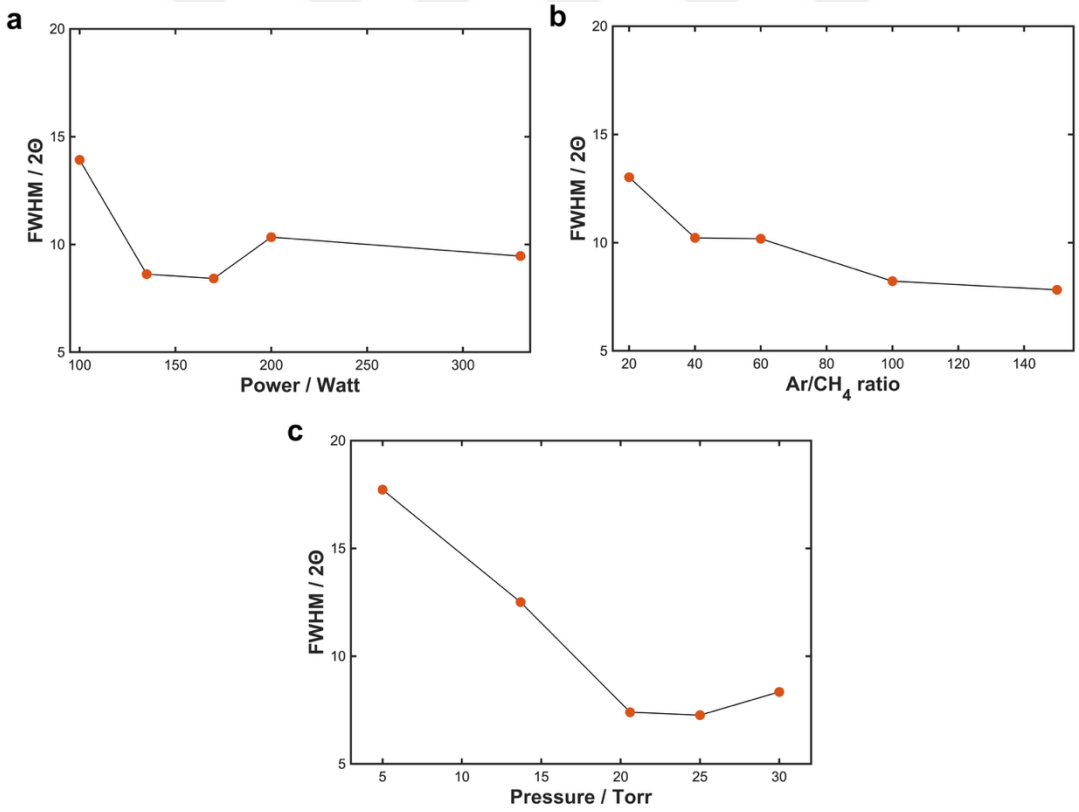

Figure 4.10. FWHM of 2Θ = 26° peak as a function of operational parameters. a) plasma power, b) Ar/CH4 ratio, c) reactor pressure**.** XRD spectra for the plots are shown in Appendix D.

which was most evident at 50 Torr where synthesized material exhibited a soft and polymeric form possibly due to lower plasma density at 50 Torr.

For residence times from 4 ms to 277 ms, Raman spectra evolved according to three-stage model of Ferrari-Robertson [150]. At lowest residence time of 4 ms, I_D/I_G was lowest which corresponded to the smallest crystallite size. I_D/I_G continued to increase up to 277 ms with *D* band getting narrower (Figure 4.12-a). Both features indicated an increase in L_a. In addition, the 2D band emerged after 26 ms at ~2665 cm^{-1}, which implied one or two layers of graphene stacking [151]. At 46 ms, 2D band moved to 2668 cm^{-1} which was a clear indicator of graphene layer increase [152]. At 277 ms, I_D/I_G corresponded to highest lateral crystallite size calculated from Tuinstra-Koenig relation [60] as 2.2 nm, climbing the Ferrari-Robertson type I_D/I_G hill (Figure 4.12-b), where a-C to nc-C transition occurs and 2D band was shifted to 2680 cm^{-1} (Figure 4.12-c), getting closer to 2700 cm^{-1} of commercial bulk graphite which has the highest stacking.

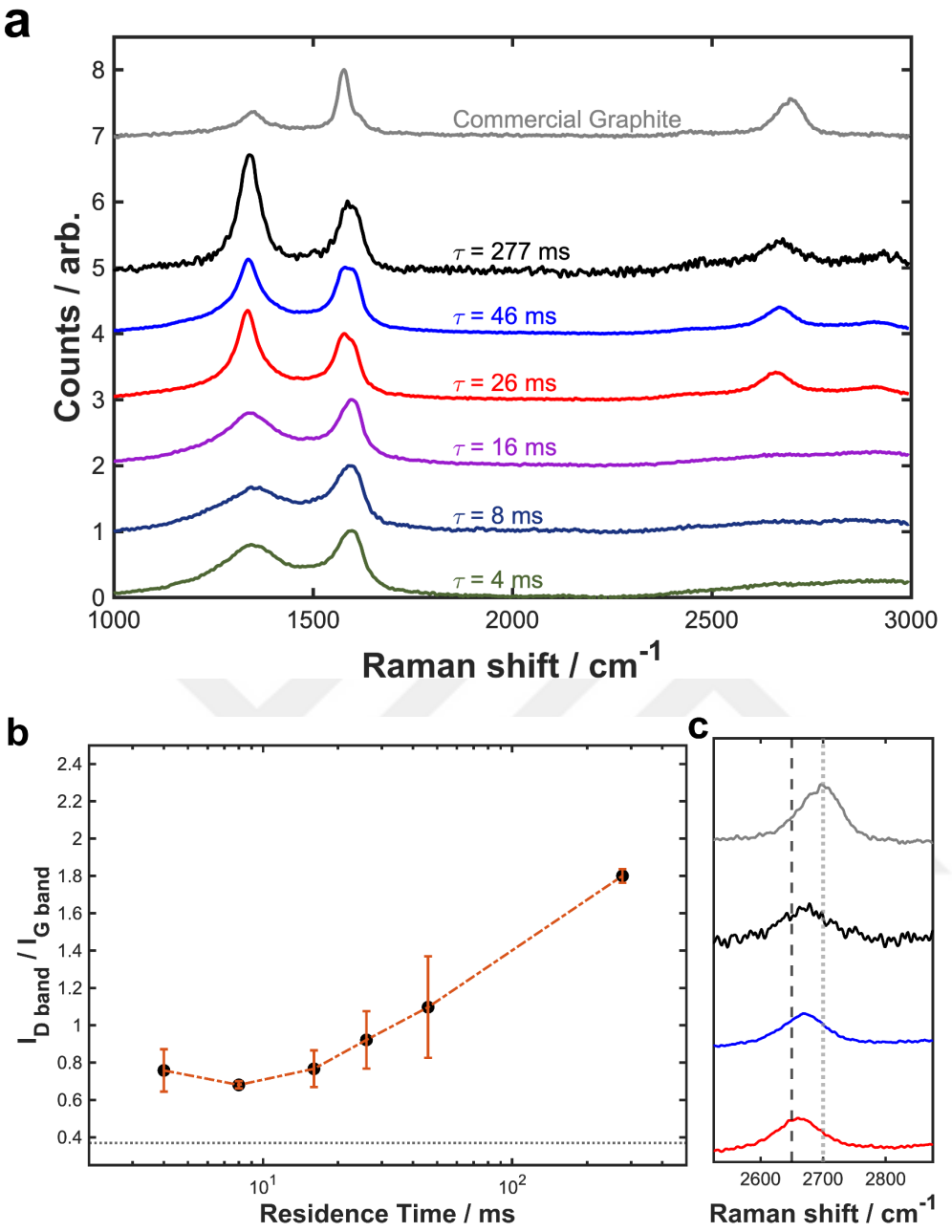

Figure 4.11. Effect of residence time on Raman spectra. a) Full Raman spectra of particles with increasing residence time. Each spectrum was collected at least three times and the spectra shown are averages. b) I_D/I_G with increasing residence time. Error bars correspond to deviations for measurements on different particles of the same batch of powder collected. c) Zoomed-in portion of Raman spectra showing the shift in the 2D band.

Increase in particle crystallinity with residence time was complemented with XRD. The diffraction peak corresponding to (002) plane of graphite became narrower as residence time was increased (Figure 4.13). Maximum L_c was calculated 1.43 nm for 277 ms corresponding to ~4 layers of graphene sheets since $d_{002} = 0.335$ nm [153]. However, for the highest residence time particles, d_{002} was calculated as 0.342 nm from Bragg's Law which corresponded to 21% degree of graphitization, a number close to 30%, implied transition from a-C to nc-G, similar to Raman results. Furthermore, peak corresponding to (111) plane of graphite (2Θ = 44°) became progressively intense with increasing residence time. Demonstrating enhanced crystallization in a-axis, this time L_a was calculated as 2.36 nm from the 44° peak for 277 ms residence time and 330 W power from the Scherrer equation, which agreed with the L_a calculated from Ferrari-Robertson relation from Raman spectrum. Increase in the intensity of (111) peak was observed at both 200 W and 330 W, where intensity ratio of 44° to 26° ($I_{44°}/I_{26°}$) up to 40% showed strong anisotropic growth

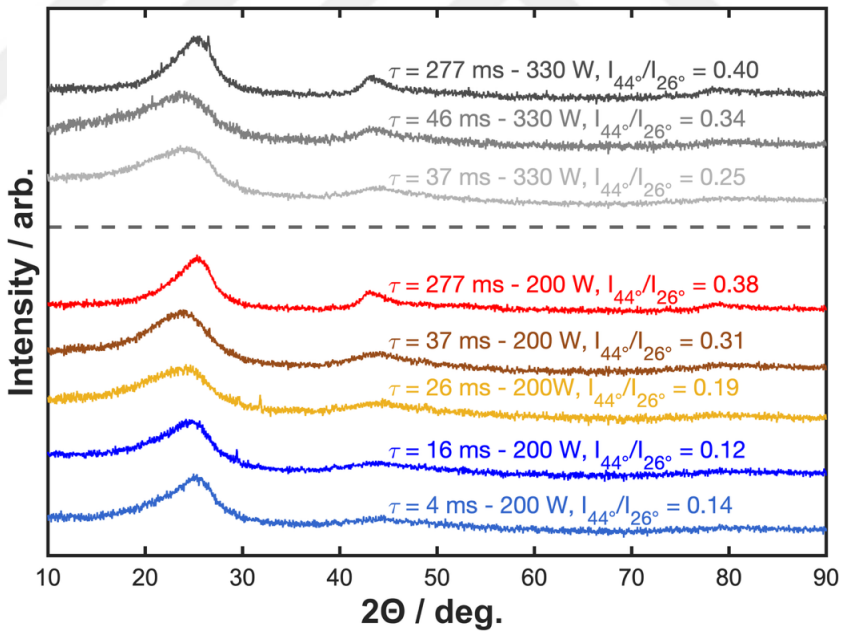

Figure 4.12. **Effect of residence time on XRD spectra.** Illustrating a decrease in FWHM of 2Θ = 26° peak and an increase in the intensity of 2Θ = 44° peak at two plasma power setting.

of particles.

TGA and DTG curves (Figure 4.14a and b) showed progressive evolution in

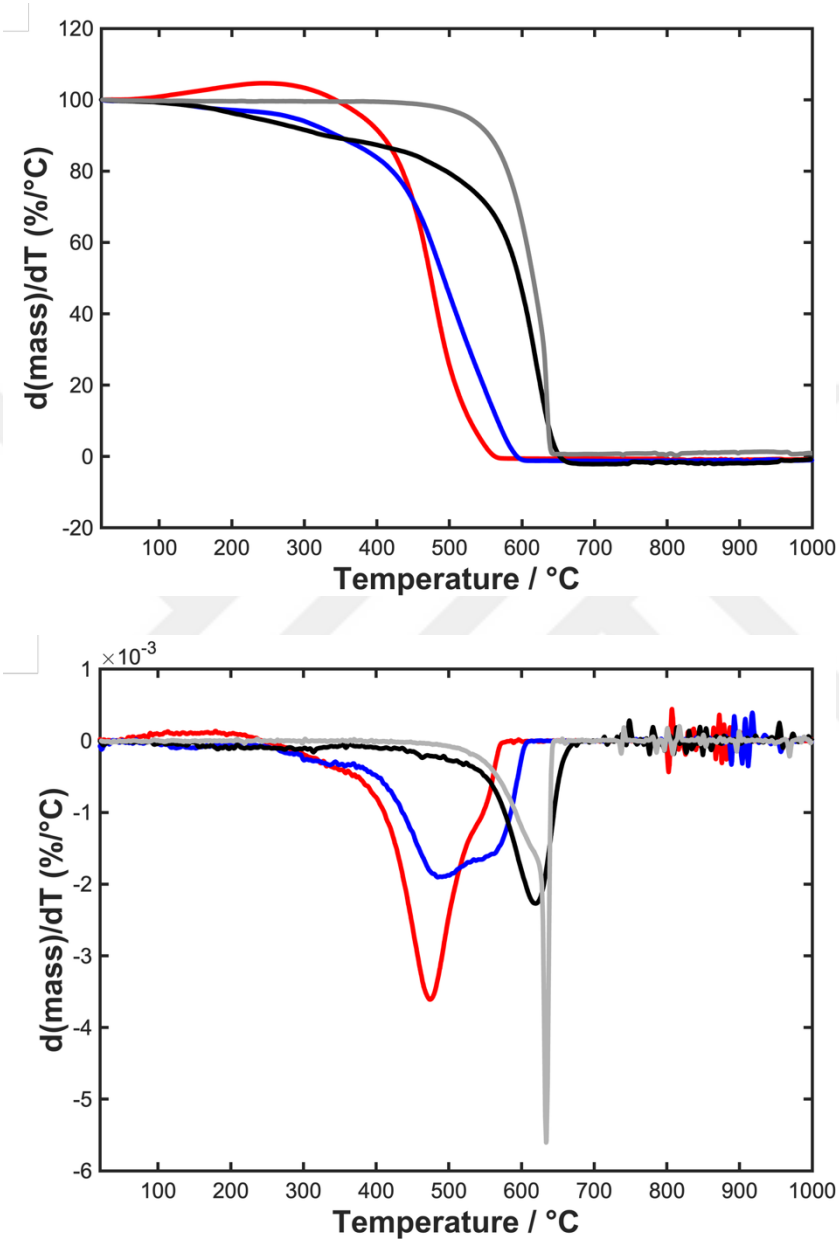

Figure 4.13. TGA (up) and DTG (bottom) curves of particles synthesized with increasing residence time. Red curve: τ = 13 ms, blue curve: τ = 37 ms, black curve: τ = 277 ms and grey curve: commercial graphite. Operating conditions: 330 W, Ar/CH_4 = 40, 30 Torr.

resistance to oxidation with increasing residence time. The main burn-off peak in DTG (Figure 4.14b) shifted from 480 °C for 13 ms to 500 °C for 37 ms and to 630 °C for 277 ms, a net total increase of 150 °C. The upward shift of the DTG peak indicated a progressive graphitization. Initially disordered and hydrogenated carbon formed at short residence times was completely oxidized at lower temperature. Accordingly, the DTG peak showed two overlapping peaks during the transition from amorphous towards more ordered carbon at 37 ms. At the longest residence time, total oxidation temperature was at its maximum approaching commercial graphite, providing strong evidence for enhanced crystallization and larger grain growth with time. DTG trends complemented Raman and XRD results that longer residence time is key for plasma annealing and dehydrogenation to achieve graphitization.

4.4 Evolution of Particle Formation via TEM

To image the pronounced anisotropy and morphology of the carbon synthesized, particles were imaged under TEM for enhanced characterization of particle morphology and growth mechanism. TEM images were obtained at three pressures, 10, 30 and 50 Torr, where we label 30 Torr as an optimum pressure and present its results first. At low residence times, i.e. at the beginning of particle formation, small particles of various sizes began to appear (Figure 4.15-a). As residence time was quadrupled, most of the small particles sintered to form bigger ones (Figure 4.15-b). Further increase resulted in opening up of particles to form an aggregate of carbon sheets (Figure 4.15-c), and a slight increment of τ resulted an increase in agglomerate size due to sintering (Figure 4.15-d). When τ was reached 46 ms, spherical primary particles emerged and pronounced sintering (Figure 4.15-e). After this point (Figure 4.15-f-g), average primary particle diameter was increased from 12.3 nm to 37.7 nm with a geometric standard deviation, σ_g, of approximately 1.1 until 277 ms (Figure 4.16). SAED analysis of the 277 ms particles

revealed well-defined concentric rings that indicate a polycrystalline structure of the aggregates (Figure 4.15-h).

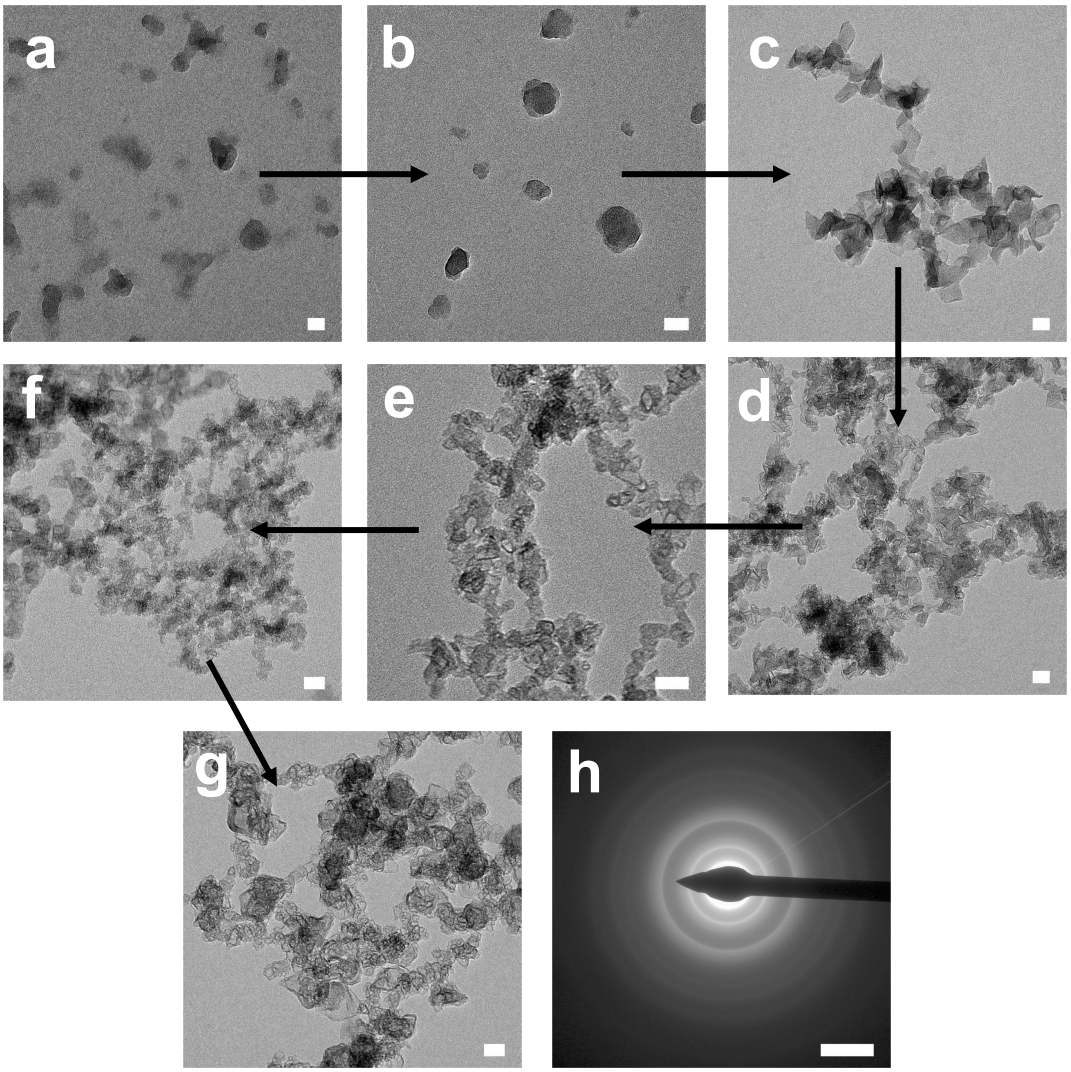

Figure 4.14. Particle formation with increasing residence time at 30 Torr. (a) 4 ms, (b) 16 ms, (c) 26 ms, (d) 37 ms, (e) 46 ms, (f) 139 ms, (g) 277 ms. (h) corresponds to SAED analysis of 277 ms particles. Scale bars for images (a)-(g) are in 50 nm width. Scale bar for SAED image is 20 nm^{-1}. Plasma power was 330 W and Ar/CH_4 ratio was 40.

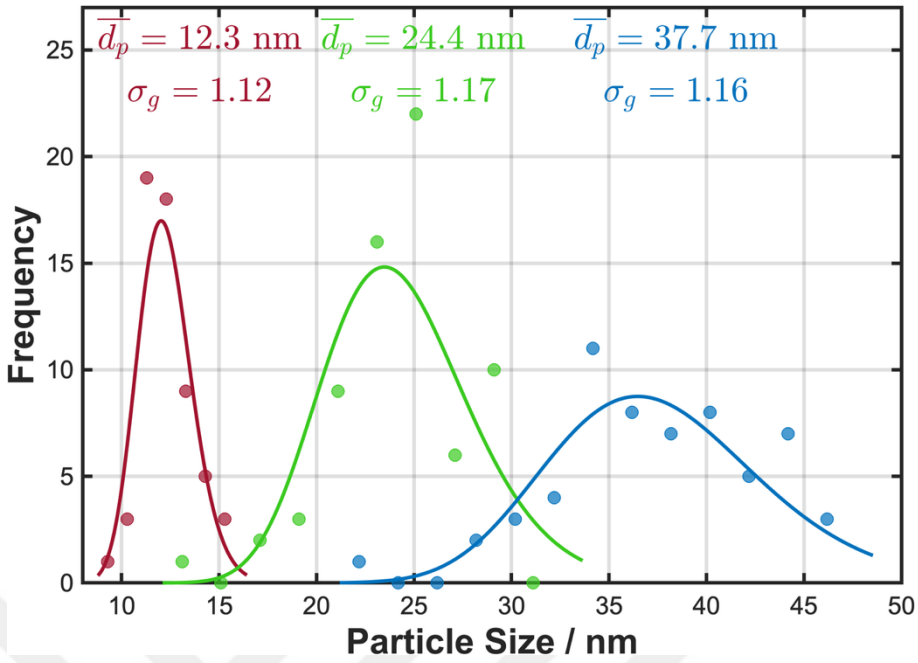

Figure 4.15. Size distribution of the primary particles of aggregates synthesized at 30 Torr. 46 ms (red), 139 ms (green) and 277 ms (blue).

HRTEM image of particles synthesized with 277 ms residence time revealed the crystal structure. Particles contained crystalline grains ≥ 5 nm (Figure 4.17-a). The interplanar spacing was measured as 0.33 nm by applying fast Fourier transform (FFT) on a selected area and generating a clear lattice fringe image via subsequent inverse FFT (Figure 4.17-b). Grain sizes reached up to 8 nm in contrast to the mean crystallite sizes of ~2 nm calculated from Scherrer equation and Tuinstra-Koenig relations, which supported the formation of polydisperse crystal size distribution.

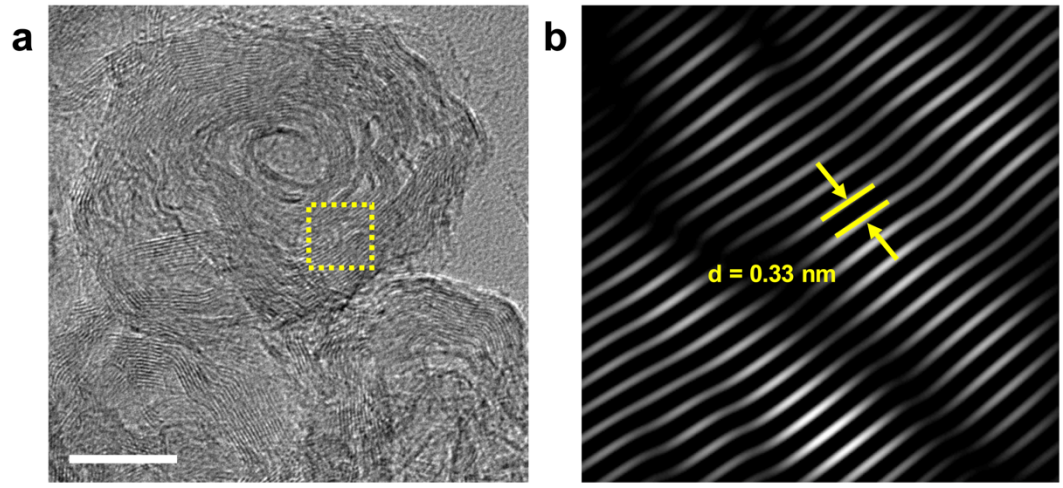

Figure 4.16. HRTEM image of 277 ms synthesized particles at 30 Torr. a) Few-nanometer sized grains are visible, b) lattice fringes with 0.33 nm spacing. Scale bar is 10 nm in width.

At 50 Torr, the exact sequence of particle-formation stages observed at 30 Torr was reproduced but shifted to longer residence times (Figure 4.18). For example, opening of particles as sheets was observed at 77 ms at 50 Torr versus 26 ms at 30 Tor (Figure 4.18-e). Higher pressure not only delayed the sequence but also increased average particles sizes. At the same mass flowrate, the increase in residence time from 277 ms to 660 ms resulted in a further increase in the average primary particle size from 37.7 nm to 42.6 nm (Figure 4.19).

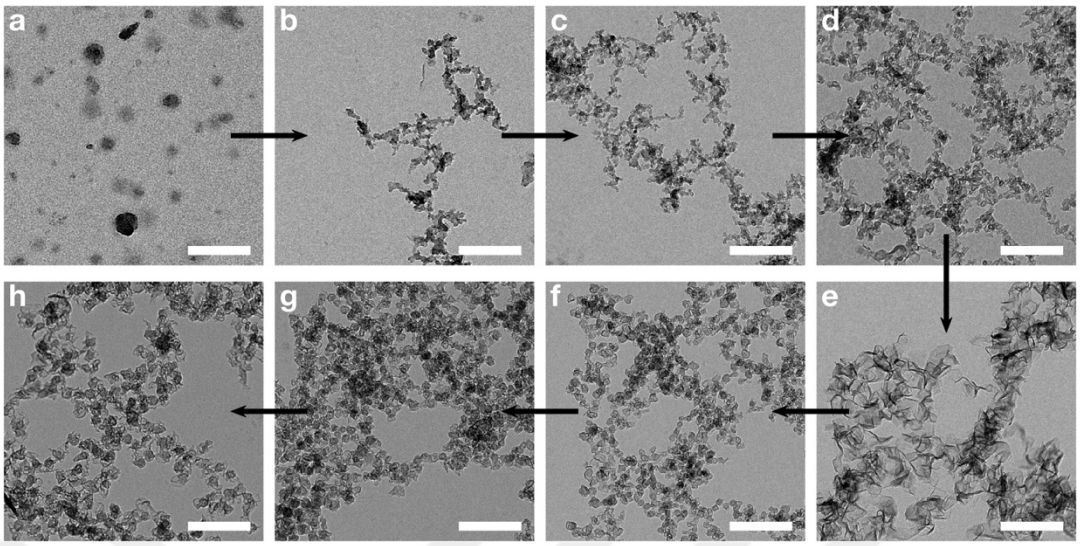

Figure 4.17. Particle formation with increasing residence time at 50 Torr. (a) 8 ms, (b) 16 ms, (c) 39 ms, (d) 57 ms, (e) 77 ms, (f) 231 ms, (g) 308 ms. (h) 660 ms. Scale bars are in 100 nm width.

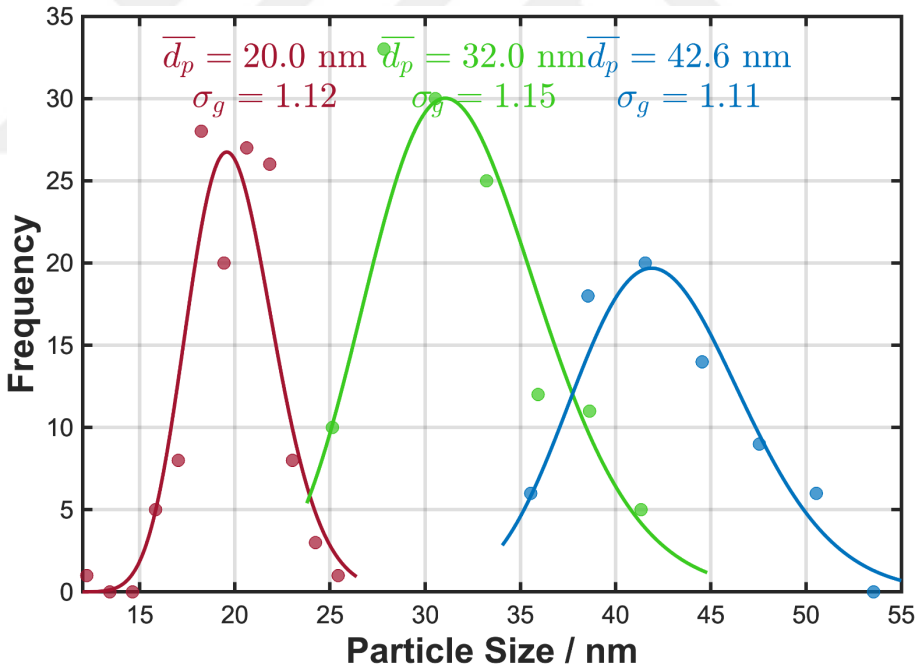

Figure 4.18. Size distribution of particles synthesized at 50 Torr. 231 ms (red), 308 ms (green) and 660 ms (blue).

At lower pressure (10 Torr), agglomerates appeared as early as 4 ms compared to 30 Torr, indicating a faster formation rate (Figure 4.20-a). At 16 ms spherical primary particles were apparent (Figure 4.20-b), however, unlike higher pressure cases, opening up of particles as graphene sheets did not lead to formation of onion-like hollow spheres at low pressure. This behavior underscored the need for higher pressure for synthesizing crystalline carbonaceous particles as the SAED pattern of particles synthesized at 220 ms showed very diffuse concentric rings, which implied low degree of crystallization (Figure 4.21).

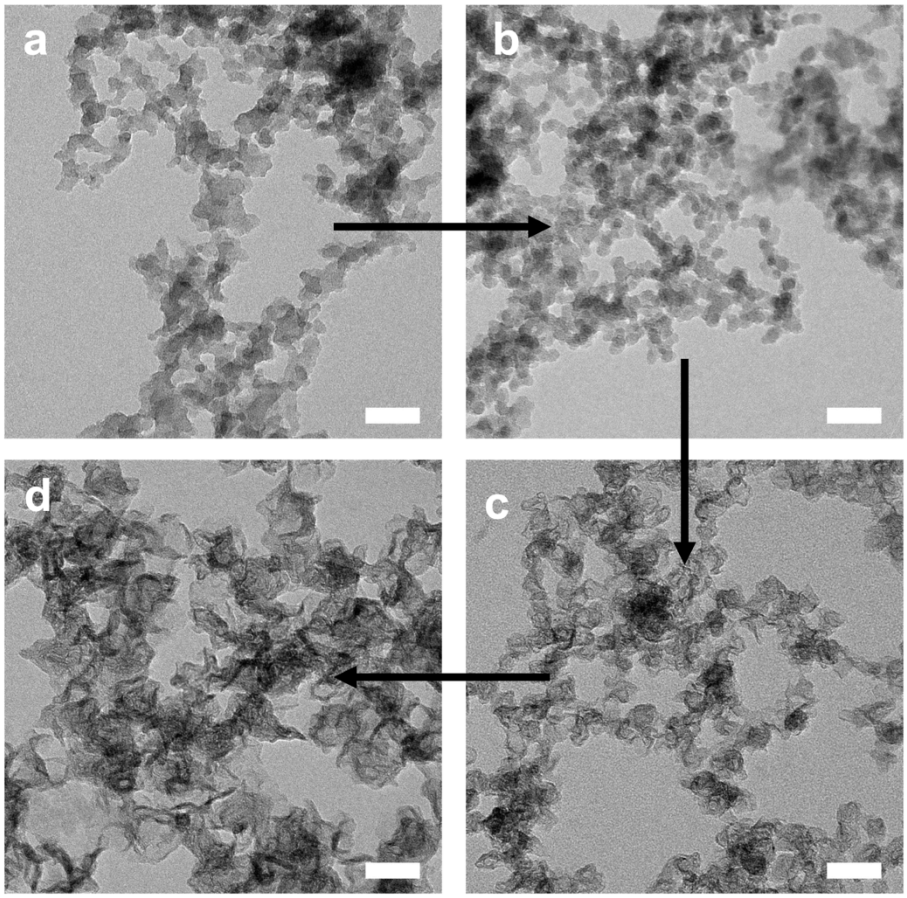

Figure 4.19. Particle formation with increasing residence time at 10 Torr. (a) 4 ms, (b) 15 ms, (c) 61 ms, (d) 220 ms. Scale bars are in 50 nm width.

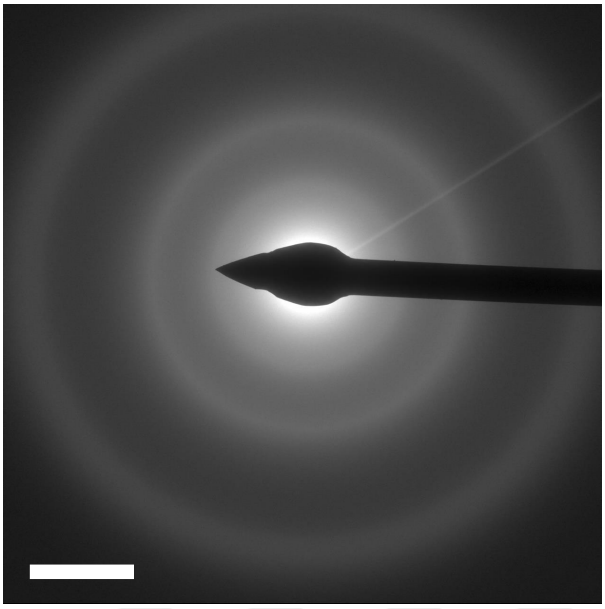

Figure 4.20. **SAED pattern of particles synthesized at 10 Torr and 220 ms.** Scale bar is in 10 nm^{-1} in width.

SAED patterns of particles synthesized at increasing pressure with similar residence times show that the sharpest rings were obtained at 30 Torr (Figure 4.22-b), where particles synthesized at 10 Torr yielded the most diffuse rings (Figure 4.22-a) and crystallinity of particles synthesized at 50 Torr was intermediate (Figure 4.22-c).

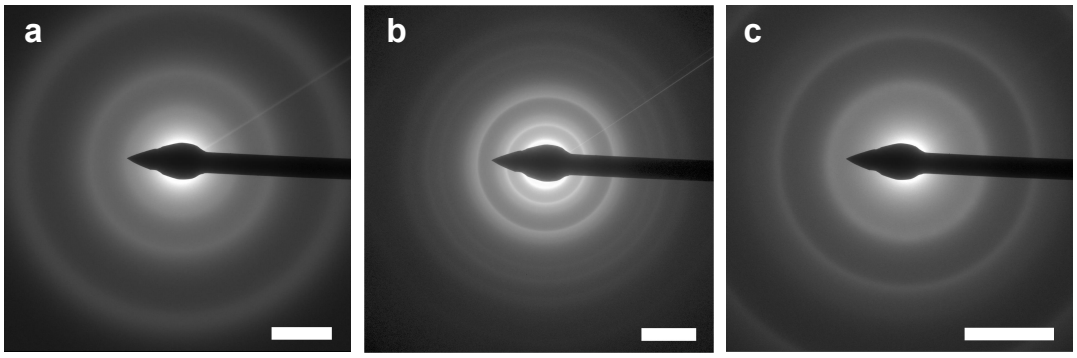

Figure 4.22. SAED pattern comparison of particles synthesized at high residence times. Particles were synthesized at a) 10 Torr, b) 30 Torr and c) 50 Torr. Scale bar is 10 nm^{-1} in width.

CHAPTER 5

SUMMARY, CONCLUSION AND FUTURE WORK

5.1 Summary

In this thesis, synthesis and evolution of carbonaceous nanoparticles in capacitively-coupled, non-equilibrium flow-through plasma reactors were experimentally studied. Experiments were conducted to understand the effect of operational parameters on particle formation from gas phase synthesis of carbonaceous nanoparticles from methane, but more importantly the graphitization of these particles. The effects were investigated through visual observation, simple OES diagnostics and *ex-situ* powder characterization, the latter of which was made possible thanks to a custom-designed and in-house manufactured Stairmand-type cyclone separator. Cyclone separator not only separated particles with respect to their mobilities but also conducted purification, since lowest mobility particles were fragments of wall film and highest mobility particles were in-flight synthesized particles. Preliminary plasma diagnostics and bulk characterization methods showed the importance of two main parameters: pressure and residence time.

TGA results showed approach of oxidation peaks of synthesized particles to bulk graphite with increased residence time. Furthermore, a mechanistic particle formation study was developed through TEM images with a set of residence time and pressure series where highest quality synthesized particles consisted of grains sized up to 8 nm and showed a crumpled graphene sheet-like structure at 277 ms and 30 Torr. These crystal sizes were apparently polydisperse and XRD and Raman relationships suggested a mean size of sizes ~2 nm, which is also partially due to the anisotropy of the crystals formed.

5.2 Conclusion

Implementing a cyclone separator to isolate in-flight synthesized material from film dropouts was shown to be crucial for material characterization through microscopy and thermogravimetric analysis. Particle nucleation, growth and crystallization in Ar/CH_4 plasma was observed to be possible, however, when compared to metal oxides, Si and other nanocrystals, particles did not become fully dense even at high power density. Required power densities appeared to be a few times greater for similar mass feeds. Crystal sizes were smaller as observed via XRD, Raman and TEM. In addition to high power (~330 W), higher pressures (~30-50 Torr) and much longer residence times (~300 ms) were required for enhanced particle graphitization.

Particles synthesized in this thesis were more crystalline compared to particles synthesized with similar experimental set-ups which were mentioned in the literature review chapter as evidenced by Raman and XRD results. In addition, TEM images provided valuable insights on how particles were formed and evolved in a span of varying pressure and residence time.

5.3 Future Work

Since carbonaceous particle formation was hypothesized to be Ferrari-Robertson type of growth with residence time, it should be possible to move around or inside the ternary phase diagram of carbon particles (Figure 2.1). In other words, with appropriate choice of operating parameters, there is a possibility to synthesize highly sp^3 hybridized particles such as diamondlike carbon and nanodiamonds with this experimental setup. To this extent, particle heating in the plasma should be increased by increasing the plasma density with following ways: increasing the plasma power or reducing the reactor diameter. Since crystal size growth was demonstrated to be directly related to residence time, even higher residence times up to order of seconds should be employed to achieve several tens of nanometer sized

nanodiamonds. Together with argon and methane, hydrogen should be supplied to the plasma reactor for enhanced gas heating and to etch sp^2 hybridized particles [154]. Incorporation of nitrogen defect should be accomplishable by introducing high-purity nitrogen feed to the plasma reactor.

In addition to existing characterization methods used in this thesis, X-ray photoelectron spectroscopy (XPS) should be carried out for determining the direction for nanodiamond growth to quantify sp^2 and sp^3 hybridization ratios.

REFERENCES

[1] M. Asplund, N. Grevesse, A. J. Sauval, and P. Scott, "The Chemical Composition of the Sun," *Annu. Rev. Astron. Astrophys.*, vol. 47, no. 1, pp. 481–522, Sept. 2009, doi: 10.1146/annurev.astro.46.060407.145222.

[2] Th. Henning and F. Salama, "Carbon in the Universe," *Science*, vol. 282, no. 5397, pp. 2204–2210, Dec. 1998, doi: 10.1126/science.282.5397.2204.

[3] J. C. Meyer, A. K. Geim, M. I. Katsnelson, K. S. Novoselov, T. J. Booth, and S. Roth, "The structure of suspended graphene sheets," *Nature*, vol. 446, no. 7131, pp. 60–63, Mar. 2007, doi: 10.1038/nature05545.

[4] J. D. Bernal, "The structure of graphite," *Proc. R. Soc. Lond. Ser. Contain. Pap. Math. Phys. Character*, vol. 106, no. 740, pp. 749–773, Jan. 1997, doi: 10.1098/rspa.1924.0101.

[5] W. H. Bragg and W. L. Bragg, "The structure of the diamond," *Proc. R. Soc. Lond. Ser. Contain. Pap. Math. Phys. Character*, vol. 89, no. 610, pp. 277–291, Jan. 1997, doi: 10.1098/rspa.1913.0084.

[6] H. Dai, "Carbon nanotubes: opportunities and challenges".

[7] H. Prinzbach *et al.*, "Gas-phase production and photoelectron spectroscopy of the smallest fullerene, C20," *Nature*, vol. 407, no. 6800, pp. 60–63, Sept. 2000, doi: 10.1038/35024037.

[8] L. Liu, F. Lu, J. Tian, S. Xia, and Y. Diao, "Electronic and optical properties of amorphous carbon with different sp3/sp2 hybridization ratio," *Appl. Phys. A*, vol. 125, no. 5, p. 366, May 2019, doi: 10.1007/s00339-019-2660-3.

[9] J. Robertson, "Mechanical properties and structure of diamond-like carbon," *Diam. Relat. Mater.*, vol. 1, no. 5–6, pp. 397–406, Apr. 1992, doi: 10.1016/0925-9635(92)90137-D.

[10] M. Sevilla and R. Mokaya, “Energy storage applications of activated carbons: supercapacitors and hydrogen storage,” *Energy Environ. Sci.*, vol. 7, no. 4, pp. 1250–1280, 2014, doi: 10.1039/C3EE43525C.

[11] D. S. Su and R. Schlögl, “Nanostructured Carbon and Carbon Nanocomposites for Electrochemical Energy Storage Applications,” *ChemSusChem*, vol. 3, no. 2, pp. 136–168, 2010, doi: 10.1002/cssc.200900182.

[12] Y. Wang, H. Wei, Y. Lu, S. Wei, E. K. Wujcik, and Z. Guo, “Multifunctional Carbon Nanostructures for Advanced Energy Storage Applications,” *Nanomaterials*, vol. 5, no. 2, pp. 755–777, June 2015, doi: 10.3390/nano5020755.

[13] Y. Zhai, Z. Zhu, and S. Dong, “Carbon-Based Nanostructures for Advanced Catalysis,” *ChemCatChem*, vol. 7, no. 18, pp. 2806–2815, Sept. 2015, doi: 10.1002/cctc.201500323.

[14] F. Rodríguez-reinoso, “The role of carbon materials in heterogeneous catalysis,” *Carbon*, vol. 36, no. 3, pp. 159–175, Jan. 1998, doi: 10.1016/S0008-6223(97)00173-5.

[15] Y. Yang, K. Chiang, and N. Burke, “Porous carbon-supported catalysts for energy and environmental applications: A short review,” *Catal. Today*, vol. 178, no. 1, pp. 197–205, Dec. 2011, doi: 10.1016/j.cattod.2011.08.028.

[16] Y. Yan *et al.*, “Carbon nanotube catalysts: recent advances in synthesis, characterization and applications,” *Chem. Soc. Rev.*, vol. 44, no. 10, pp. 3295–3346, 2015, doi: 10.1039/C4CS00492B.

[17] N. Agarwal *et al.*, “An overview of carbon-carbon composite materials and their applications,” *Front. Mater.*, vol. 11, July 2024, doi: 10.3389/fmats.2024.1374034.

[18] Yu. S. Virgil’ev and I. P. Kalyagina, “Carbon–Carbon Composite Materials,” *Inorg. Mater.*, vol. 40, no. 1, pp. S33–S49, Jan. 2004, doi: 10.1023/B:INMA.0000036327.90241.5a.

[19] C. L. Holloway, M. S. Sarto, and M. Johansson, “Analyzing carbon-fiber composite materials with equivalent-Layer models,” *IEEE Trans. Electromagn. Compat.*, vol. 47, no. 4, pp. 833–844, Nov. 2005, doi: 10.1109/TEMC.2005.854101.

[20] Y. Zhang, K. Y. Rhee, D. Hui, and S.-J. Park, “A critical review of nanodiamond based nanocomposites: Synthesis, properties and applications,” *Compos. Part B Eng.*, vol. 143, pp. 19–27, June 2018, doi: 10.1016/j.compositesb.2018.01.028.

[21] K. B. Holt, “Diamond at the nanoscale: applications of diamond nanoparticles from cellular biomarkers to quantum computing,” *Philos. Trans. R. Soc. Math. Phys. Eng. Sci.*, vol. 365, no. 1861, pp. 2845–2861, Sept. 2007, doi: 10.1098/rsta.2007.0005.

[22] M. D. Torelli, N. A. Nunn, and O. A. Shenderova, “A Perspective on Fluorescent Nanodiamond Bioimaging,” *Small*, vol. 15, no. 48, p. 1902151, 2019, doi: 10.1002/smll.201902151.

[23] Y. Y. Hui, C.-L. Cheng, and H.-C. Chang, “Nanodiamonds for optical bioimaging,” *J. Phys. Appl. Phys.*, vol. 43, no. 37, p. 374021, Sept. 2010, doi: 10.1088/0022-3727/43/37/374021.

[24] F. Liu *et al.*, “Synthesis of graphene materials by electrochemical exfoliation: Recent progress and future potential,” *Carbon Energy*, vol. 1, no. 2, pp. 173–199, 2019, doi: 10.1002/cey2.14.

[25] P. Avouris and C. Dimitrakopoulos, “Graphene: synthesis and applications,” *Mater. Today*, vol. 15, no. 3, pp. 86–97, Mar. 2012, doi: 10.1016/S1369-7021(12)70044-5.

[26] A. Mašláni *et al.*, “Pyrolysis of methane via thermal steam plasma for the production of hydrogen and carbon black,” *Int. J. Hydrog. Energy*, vol. 46, no. 2, pp. 1605–1614, Jan. 2021, doi: 10.1016/j.ijhydene.2020.10.105.

[27] L. Fulcheri, V.-J. Rohani, E. Wyse, N. Hardman, and E. Dames, “An energy-efficient plasma methane pyrolysis process for high yields of carbon black and hydrogen,” *Int. J. Hydrog. Energy*, vol. 48, no. 8, pp. 2920–2928, Jan. 2023, doi: 10.1016/j.ijhydene.2022.10.144.

[28] J. E. Butler and A. V. Sumant, “The CVD of Nanodiamond Materials,” *Chem. Vap. Depos.*, vol. 14, no. 7–8, pp. 145–160, 2008, doi: 10.1002/cvde.200700037.

[29] A. Belamkar, B. Wagner, M. Kim, F. Bermudez, and L. Mangolini, “Conversion of Methane to Graphite-Like Carbon Nanoparticles Using a Low-Temperature Dusty Plasma,” *ACS Appl. Nano Mater.*, vol. 7, no. 10, pp. 11053–11058, May 2024, doi: 10.1021/acsanm.4c01614.

[30] X. Huang and S. Li, “Solubility of Acetylene in Alcohols and Ketones,” *J. Chem. Eng. Data*, vol. 63, no. 6, pp. 2127–2134, June 2018, doi: 10.1021/acs.jced.8b00126.

[31] E. Dames, V. Rohani, and L. Fulcheri, “Plasma chemistry and plasma reactors for turquoise hydrogen and carbon nanomaterials production,” in *Advances in Chemical Engineering*, vol. 61, Elsevier, 2023, pp. 253–317. doi: 10.1016/bs.ache.2023.05.001.

[32] M. Wolter, I. Levchenko, H. Kersten, and K. (Ken) Ostrikov, “Hydrogen in plasma-nanofabrication: Selective control of nanostructure heating and passivation,” *Appl. Phys. Lett.*, vol. 96, no. 13, p. 133105, Mar. 2010, doi: 10.1063/1.3374324.

[33] U. R. Kortshagen, R. M. Sankaran, R. N. Pereira, S. L. Girshick, J. J. Wu, and E. S. Aydil, “Nonthermal Plasma Synthesis of Nanocrystals: Fundamental Principles, Materials, and Applications,” *Chem. Rev.*, vol. 116, no. 18, pp. 11061–11127, Sept. 2016, doi: 10.1021/acs.chemrev.6b00039.

[34] D. Das and A. Roy, “Growth of Nanostructured Diamond Films on Glass Substrates by Low-Temperature Microwave Plasma-Enhanced Chemical Vapor

Deposition for Applications in Nanotribology," *ACS Appl. Nano Mater.*, vol. 5, no. 3, pp. 3558–3571, Mar. 2022, doi: 10.1021/acsanm.1c04175.

[35] N. B. Uner and E. Thimsen, "Nonequilibrium plasma aerotaxy of size controlled GaN nanocrystals," *J. Phys. Appl. Phys.*, vol. 53, no. 9, p. 095201, Dec. 2019, doi: 10.1088/1361-6463/ab59e6.

[36] D. V. Szabó and S. Schlabach, "Microwave Plasma Synthesis of Materials—From Physics and Chemistry to Nanoparticles: A Materials Scientist's Viewpoint," *Inorganics*, vol. 2, no. 3, pp. 468–507, Sept. 2014, doi: 10.3390/inorganics2030468.

[37] L. Mangolini, E. Thimsen, and U. Kortshagen, "High-Yield Plasma Synthesis of Luminescent Silicon Nanocrystals," *Nano Lett.*, vol. 5, no. 4, pp. 655–659, Apr. 2005, doi: 10.1021/nl050066y.

[38] A. J. Cendejas, H. Sun, S. E. Hayes, U. Kortshagen, and E. Thimsen, "Predicting plasma conditions necessary for synthesis of γ-Al2O3 nanocrystals," *Nanoscale*, vol. 13, no. 26, pp. 11387–11395, July 2021, doi: 10.1039/D1NR02488D.

[39] D. Mariotti and R. M. Sankaran, "Microplasmas for nanomaterials synthesis," *J. Phys. Appl. Phys.*, vol. 43, no. 32, p. 323001, July 2010, doi: 10.1088/0022-3727/43/32/323001.

[40] T. Nikhar *et al.*, "Importance of gas heating in capacitively coupled radiofrequency plasma-assisted synthesis of carbon nanomaterials," *J. Phys. Appl. Phys.*, vol. 57, no. 47, p. 475205, Aug. 2024, doi: 10.1088/1361-6463/ad6d78.

[41] "A. Belamkar, B. Wagner, M. Kim, F. Bermudez, and L. Mangolini, ACS Appl. Nano Mater., 2024, 7 (10), 11053–11058. - Google'da Ara." Accessed: Aug. 11, 2025. [Online]. Available: https://pubs.acs.org/doi/10.1021/acsami.3c12696

[42] A. Woodard, K. Shojaei, G. Nava, and L. Mangolini, "Graphitization of Carbon Particles in a Non-thermal Plasma Reactor," *Plasma Chem. Plasma Process.*, vol. 38, no. 4, Mar. 2018, doi: 10.1007/s11090-018-9884-4.

[43] M. Moreno-Couranjou, M. Monthioux, J. Gonzalez-Aguilar, and L. Fulcheri, "A non-thermal plasma process for the gas phase synthesis of carbon nanoparticles," *Carbon*, vol. 47, no. 10, pp. 2310–2321, Aug. 2009, doi: 10.1016/j.carbon.2009.04.003.

[44] K. De Bleecker, A. Bogaerts, and W. Goedheer, "Detailed modeling of hydrocarbon nanoparticle nucleation in acetylene discharges," *Phys. Rev. E*, vol. 73, no. 2, p. 026405, Feb. 2006, doi: 10.1103/PhysRevE.73.026405.

[45] W. Lian *et al.*, "The transformation of acetylene black into onion-like hollow carbon nanoparticles at 1000 °C using an iron catalyst," *Carbon*, vol. 46, no. 3, pp. 525–530, Mar. 2008, doi: 10.1016/j.carbon.2007.12.024.

[46] D. M. Kolotilo, "Chemical bond and properties of graphite materials," *Sov. Powder Metall. Met. Ceram.*, vol. 7, no. 12, pp. 966–971, Dec. 1968, doi: 10.1007/BF00773433.

[47] J. Vejpravová, "Mixed sp2–sp3 Nanocarbon Materials: A Status Quo Review," *Nanomaterials*, vol. 11, no. 10, p. 2469, Oct. 2021, doi: 10.3390/nano11102469.

[48] A. C. Ferrari and J. Robertson, "Interpretation of Raman spectra of disordered and amorphous carbon," *Phys. Rev. B*, vol. 61, no. 20, pp. 14095–14107, May 2000, doi: 10.1103/PhysRevB.61.14095.

[49] D. R. Cooper *et al.*, "Experimental Review of Graphene," *Int. Sch. Res. Not.*, vol. 2012, no. 1, p. 501686, 2012, doi: 10.5402/2012/501686.

[50] A. K. Geim and K. S. Novoselov, "The rise of graphene," *Nat. Mater.*, vol. 6, no. 3, pp. 183–191, Mar. 2007, doi: 10.1038/nmat1849.

[51] K. S. Novoselov *et al.*, "Two-dimensional atomic crystals," *Proc. Natl. Acad. Sci.*, vol. 102, no. 30, pp. 10451–10453, July 2005, doi: 10.1073/pnas.0502848102.

[52] “Novoselov, K. S. et al. Electric fi eld eff ect in atomically thin carbon fi lms. Science 306, 666–669 (2004). - Google’da Ara.” Accessed: Aug. 13, 2025. [Online]. Available: https://www.science.org/doi/10.1126/science.1102896

[53] A. K. Geim, “Graphene: Status and Prospects,” *Science*, vol. 324, no. 5934, pp. 1530–1534, June 2009, doi: 10.1126/science.1158877.

[54] D. D. L. Chung, “Review Graphite,” *J. Mater. Sci.*, vol. 37, no. 8, pp. 1475–1489, Apr. 2002, doi: 10.1023/A:1014915307738.

[55] Z. Q. Li, C. J. Lu, Z. P. Xia, Y. Zhou, and Z. Luo, “X-ray diffraction patterns of graphite and turbostratic carbon,” *Carbon*, vol. 45, no. 8, pp. 1686–1695, July 2007, doi: 10.1016/j.carbon.2007.03.038.

[56] R. Sengupta, M. Bhattacharya, S. Bandyopadhyay, and A. K. Bhowmick, “A review on the mechanical and electrical properties of graphite and modified graphite reinforced polymer composites,” *Prog. Polym. Sci.*, vol. 36, no. 5, pp. 638–670, May 2011, doi: 10.1016/j.progpolymsci.2010.11.003.

[57] L. A. Falkovsky, “Anisotropy of graphite optical conductivity,” *JETP Lett.*, vol. 92, no. 5, pp. 348–351, Sept. 2010, doi: 10.1134/S0021364010170169.

[58] J. Robertson, “Diamond-like amorphous carbon,” *Mater. Sci. Eng. R Rep.*, vol. 37, no. 4, pp. 129–281, May 2002, doi: 10.1016/S0927-796X(02)00005-0.

[59] S. Zhang *et al.*, “Discovery of carbon-based strongest and hardest amorphous material,” *Natl. Sci. Rev.*, vol. 9, no. 1, p. nwab140, Jan. 2022, doi: 10.1093/nsr/nwab140.

[60] F. Tuinstra and J. L. Koenig, “Raman Spectrum of Graphite,” *J. Chem. Phys.*, vol. 53, no. 3, pp. 1126–1130, Aug. 1970, doi: 10.1063/1.1674108.

[61] Y. B. Tan and J.-M. Lee, “Graphene for supercapacitor applications,” *J. Mater. Chem. A*, vol. 1, no. 47, pp. 14814–14843, Nov. 2013, doi: 10.1039/C3TA12193C.

[62] J.-Z. Wang, C. Zhong, S.-L. Chou, and H.-K. Liu, “Flexible free-standing graphene-silicon composite film for lithium-ion batteries,” *Electrochem. Commun.*, vol. 12, no. 11, pp. 1467–1470, Nov. 2010, doi: 10.1016/j.elecom.2010.08.008.

[63] S. Watcharotone *et al.*, “Graphene−Silica Composite Thin Films as Transparent Conductors,” *Nano Lett.*, vol. 7, no. 7, pp. 1888–1892, July 2007, doi: 10.1021/nl070477+.

[64] S. Li, Y. Hu, Q. Xu, J. Sun, B. Hou, and Y. Zhang, “Iron- and nitrogen-functionalized graphene as a non-precious metal catalyst for enhanced oxygen reduction in an air-cathode microbial fuel cell,” *J. Power Sources*, vol. 213, pp. 265–269, Sept. 2012, doi: 10.1016/j.jpowsour.2012.04.002.

[65] C. Buelke, A. Alshami, J. Casler, Y. Lin, M. Hickner, and I. H. Aljundi, “Evaluating graphene oxide and holey graphene oxide membrane performance for water purification,” *J. Membr. Sci.*, vol. 588, p. 117195, Oct. 2019, doi: 10.1016/j.memsci.2019.117195.

[66] R. H. Savage, “Graphite Lubrication,” *J. Appl. Phys.*, vol. 19, no. 1, pp. 1–10, Jan. 1948, doi: 10.1063/1.1697867.

[67] C. Baudín, C. Alvarez, and R. E. Moore, “Influence of Chemical Reactions in Magnesia-Graphite Refractories: I, Effects on Texture and High-Temperature Mechanical Properties,” *J. Am. Ceram. Soc.*, vol. 82, no. 12, pp. 3529–3538, 1999, doi: 10.1111/j.1151-2916.1999.tb02276.x.

[68] E. Shobert, “Carbon, Graphite, and Contacts,” *IEEE Trans. Parts Hybrids Packag.*, vol. 12, no. 1, pp. 62–74, Mar. 1976, doi: 10.1109/TPHP.1976.1135101.

[69] D. D. L. Chung, “A perspective on electromagnetic interference shielding materials comprising exfoliated graphite,” *Carbon*, vol. 216, p. 118569, Jan. 2024, doi: 10.1016/j.carbon.2023.118569.

[70] M. Smalc, G. Shives, G. Chen, S. Guggari, J. Norley, and R. A. Reynolds, “Thermal Performance of Natural Graphite Heat Spreaders,” presented at the ASME

2005 Pacific Rim Technical Conference and Exhibition on Integration and Packaging of MEMS, NEMS, and Electronic Systems collocated with the ASME 2005 Heat Transfer Summer Conference, American Society of Mechanical Engineers Digital Collection, Mar. 2009, pp. 79–89. doi: 10.1115/IPACK2005-73073.

[71] B. Moradi and G. G. Botte, "Recycling of graphite anodes for the next generation of lithium ion batteries," *J. Appl. Electrochem.*, vol. 46, no. 2, pp. 123–148, Feb. 2016, doi: 10.1007/s10800-015-0914-0.

[72] L. Zhao *et al.*, "Revisiting the Roles of Natural Graphite in Ongoing Lithium-Ion Batteries," *Adv. Mater.*, vol. 34, no. 18, p. 2106704, 2022, doi: 10.1002/adma.202106704.

[73] M. Abdollahifar, S. Doose, H. Cavers, and A. Kwade, "Graphite Recycling from End-of-Life Lithium-Ion Batteries: Processes and Applications," *Adv. Mater. Technol.*, vol. 8, no. 2, p. 2200368, 2023, doi: 10.1002/admt.202200368.

[74] Y. Fan, G. D. Fowler, and M. Zhao, "The past, present and future of carbon black as a rubber reinforcing filler – A review," *J. Clean. Prod.*, vol. 247, p. 119115, Feb. 2020, doi: 10.1016/j.jclepro.2019.119115.

[75] B. Orel, I. Radoczy, and Z. Crnjak Orel, "Organic soot pigmented paint for solar panels: Formulation, optical properties and industrial application," *Sol. Wind Technol.*, vol. 3, no. 1, pp. 45–52, Jan. 1986, doi: 10.1016/0741-983X(86)90047-0.

[76] Z. Wei, D. Wang, X. Yang, C. Wang, G. Chen, and F. Du, "From Crystalline to Amorphous: An Effective Avenue to Engineer High-Performance Electrode Materials for Sodium-Ion Batteries," *Adv. Mater. Interfaces*, vol. 5, no. 19, p. 1800639, 2018, doi: 10.1002/admi.201800639.

[77] Q. Li, Y. Zhu, P. Zhao, C. Yuan, M. Chen, and C. Wang, "Commercial activated carbon as a novel precursor of the amorphous carbon for high-performance sodium-ion batteries anode," *Carbon*, vol. 129, pp. 85–94, Apr. 2018, doi: 10.1016/j.carbon.2017.12.008.

[78] K. Kanda *et al.*, “Application of diamond-coated cutting tools,” *Surf. Coat. Technol.*, vol. 73, no. 1, pp. 115–120, July 1995, doi: 10.1016/0257-8972(94)02370-0.

[79] V. Mochalin, O. Shenderova, D. Ho, and Y. Gogotsi, “The Properties and Applications of Nanodiamonds,” in *Nano-Enabled Medical Applications*, Jenny Stanford Publishing, 2020.

[80] M. H. Alkahtani *et al.*, “Fluorescent nanodiamonds: past, present, and future,” *Nanophotonics*, vol. 7, no. 8, pp. 1423–1453, Aug. 2018, doi: 10.1515/nanoph-2018-0025.

[81] C. Laube *et al.*, “Controlling the fluorescence properties of nitrogen vacancy centers in nanodiamonds,” *Nanoscale*, vol. 11, no. 4, pp. 1770–1783, 2019, doi: 10.1039/C8NR07828A.

[82] L. Childress and R. Hanson, “Diamond NV centers for quantum computing and quantum networks,” *MRS Bull.*, vol. 38, no. 2, pp. 134–138, Feb. 2013, doi: 10.1557/mrs.2013.20.

[83] M. D. Torelli, N. A. Nunn, and O. A. Shenderova, “A Perspective on Fluorescent Nanodiamond Bioimaging,” *Small*, vol. 15, no. 48, p. 1902151, 2019, doi: 10.1002/smll.201902151.

[84] S. J. Blanksby and G. B. Ellison, “Bond Dissociation Energies of Organic Molecules,” *Acc. Chem. Res.*, vol. 36, no. 4, pp. 255–263, Apr. 2003, doi: 10.1021/ar020230d.

[85] S. Schneider, S. Bajohr, F. Graf, and T. Kolb, “State of the Art of Hydrogen Production via Pyrolysis of Natural Gas,” *ChemBioEng Rev.*, vol. 7, no. 5, pp. 150–158, 2020, doi: 10.1002/cben.202000014.

[86] A. Abánades, “Low Carbon Production of Hydrogen by Methane Decarbonization,” in *Production of Hydrogen from Renewable Resources*, Z. Fang,

Jr. Smith Richard L., and X. Qi, Eds., Dordrecht: Springer Netherlands, 2015, pp. 149–177. doi: 10.1007/978-94-017-7330-0_6.

[87] M. Plevan *et al.*, “Thermal cracking of methane in a liquid metal bubble column reactor: Experiments and kinetic analysis,” *Int. J. Hydrog. Energy*, vol. 40, no. 25, pp. 8020–8033, July 2015, doi: 10.1016/j.ijhydene.2015.04.062.

[88] M. Msheik, S. Rodat, and S. Abanades, “Methane Cracking for Hydrogen Production: A Review of Catalytic and Molten Media Pyrolysis,” *Energies*, vol. 14, no. 11, p. 3107, Jan. 2021, doi: 10.3390/en14113107.

[89] T. Yang *et al.*, “Hydrogen-Abstraction/Acetylene-Addition Exposed,” *Angew. Chem. Int. Ed.*, vol. 55, no. 48, pp. 14983–14987, 2016, doi: 10.1002/anie.201607509.

[90] P. Liu, H. Lin, Y. Yang, C. Shao, B. Guan, and Z. Huang, “Investigating the Role of CH2 Radicals in the HACA Mechanism,” *J. Phys. Chem. A*, vol. 119, no. 13, pp. 3261–3268, Apr. 2015, doi: 10.1021/jp5124162.

[91] T. Mendiara, M. U. Alzueta, A. Millera, and R. Bilbao, “A Comparison of Acetylene Soot and Two Different Carbon Blacks: Reactivity to Oxygen and NO,” *Int. J. Chem. React. Eng.*, vol. 5, no. 1, Nov. 2007, doi: 10.2202/1542-6580.1510.

[92] Y. Tian *et al.*, “Synthesis of carbon-based materials by methane pyrolysis in a low-current gliding arc discharge,” *Surf. Coat. Technol.*, vol. 505, p. 132063, June 2025, doi: 10.1016/j.surfcoat.2025.132063.

[93] M. Taheraslani and H. Gardeniers, “Coupling of CH4 to C2 Hydrocarbons in a Packed Bed DBD Plasma Reactor: The Effect of Dielectric Constant and Porosity of the Packing,” *Energies*, vol. 13, no. 2, p. 468, Jan. 2020, doi: 10.3390/en13020468.

[94] A. Grill, B. S. Meyerson, and V. V. Patel, “Diamondlike carbon films by rf plasma-assisted chemical vapor deposition from acetylene,” *IBM J. Res. Dev.*, vol. 34, no. 6, pp. 849–857, Nov. 1990, doi: 10.1147/rd.346.0849.

[95] A. N. Obraztsov, A. A. Zolotukhin, A. O. Ustinov, A. P. Volkov, Yu. Svirko, and K. Jefimovs, “DC discharge plasma studies for nanostructured carbon CVD,” *Diam. Relat. Mater.*, vol. 12, no. 3, pp. 917–920, Mar. 2003, doi: 10.1016/S0925-9635(02)00338-2.

[96] J. P. Trelles, “Nonequilibrium Phenomena in (Quasi-)thermal Plasma Flows,” *Plasma Chem. Plasma Process.*, vol. 40, no. 3, pp. 727–748, May 2020, doi: 10.1007/s11090-019-10046-1.

[97] L. Mangolini and U. Kortshagen, “Plasma-Assisted Synthesis of Silicon Nanocrystal Inks,” *Adv. Mater.*, vol. 19, no. 18, pp. 2513–2519, 2007, doi: 10.1002/adma.200700595.

[98] P. Felbier *et al.*, “Highly Luminescent ZnO Quantum Dots Made in a Nonthermal Plasma,” *Adv. Funct. Mater.*, vol. 24, no. 14, pp. 1988–1993, 2014, doi: 10.1002/adfm.201303449.

[99] Y. Huang *et al.*, “An overview of low-temperature plasma surface modification of carbon materials for removal of pollutants from liquid and gas phases,” *Plasma Process. Polym.*, vol. 18, no. 3, p. 2000171, 2021, doi: 10.1002/ppap.202000171.

[100] V. A. Rakov and M. A. Uman, *Lightning: physics and effects*. Cambridge, U.K. ; New York: Cambridge University Press, 2003.

[101] M. I. Boulos, “Thermal plasma processing,” *IEEE Trans. Plasma Sci.*, vol. 19, no. 6, pp. 1078–1089, Dec. 1991, doi: 10.1109/27.125032.

[102] N. B. Uner and E. Thimsen, “Superlocal chemical reaction equilibrium in low temperature plasma,” *AIChE J.*, vol. 66, no. 6, p. e16948, 2020, doi: 10.1002/aic.16948.

[103] P. J. Bruggeman, F. Iza, and R. Brandenburg, “Foundations of atmospheric pressure non-equilibrium plasmas,” *Plasma Sources Sci. Technol.*, vol. 26, no. 12, p. 123002, Nov. 2017, doi: 10.1088/1361-6595/aa97af.

[104] J. Gonzalez-Aguilar, M. Moreno, and L. Fulcheri, “Carbon nanostructures production by gas-phase plasma processes at atmospheric pressure,” *J. Phys. Appl. Phys.*, vol. 40, no. 8, p. 2361, Apr. 2007, doi: 10.1088/0022-3727/40/8/S16.

[105] J. Pacheco *et al.*, “Greenhouse gas treatment and H2 production, by warm plasma reforming,” *Int. J. Hydrog. Energy*, vol. 40, no. 48, pp. 17165–17171, Dec. 2015, doi: 10.1016/j.ijhydene.2015.08.062.

[106] A. Fridman, S. Nester, L. A. Kennedy, A. Saveliev, and O. Mutaf-Yardimci, “Gliding arc gas discharge,” *Prog. Energy Combust. Sci.*, vol. 25, no. 2, pp. 211–231, Apr. 1999, doi: 10.1016/S0360-1285(98)00021-5.

[107] C. Guo, F. Tang, J. Chen, X. Wang, S. Zhang, and X. Zhang, “Development of dielectric-barrier-discharge ionization,” *Anal. Bioanal. Chem.*, vol. 407, no. 9, pp. 2345–2364, Mar. 2015, doi: 10.1007/s00216-014-8281-y.

[108] U. Kogelschatz, B. Eliasson, and W. Egli, “Dielectric-Barrier Discharges. Principle and Applications,” *J. Phys. IV*, vol. 07, no. C4, pp. C4-66, Oct. 1997, doi: 10.1051/jp4:1997405.

[109] J.-S. Chang, P. A. Lawless, and T. Yamamoto, “Corona discharge processes,” *IEEE Trans. Plasma Sci.*, vol. 19, no. 6, pp. 1152–1166, Dec. 1991, doi: 10.1109/27.125038.

[110] M. Goldman, “Corona discharges and their applications,” *IEE Proc. Phys. Sci. Meas. Instrum. Manag. Educ. Rev.*, vol. 128, no. 4, pp. 298–302, May 1981, doi: 10.1049/ip-a-1.1981.0044.

[111] U. R. Kortshagen, R. M. Sankaran, R. N. Pereira, S. L. Girshick, J. J. Wu, and E. S. Aydil, “Nonthermal Plasma Synthesis of Nanocrystals: Fundamental Principles, Materials, and Applications,” *Chem. Rev.*, vol. 116, no. 18, pp. 11061–11127, Sept. 2016, doi: 10.1021/acs.chemrev.6b00039.

[112] M. Otobe, T. Kanai, T. Ifuku, H. Yajima, and S. Oda, “Nanocrystalline silicon formation in a SiH4 plasma cell,” *J. Non-Cryst. Solids*, vol. 198–200, pp. 875–878, May 1996, doi: 10.1016/0022-3093(96)00161-5.

[113] D. Wei, Y. Lu, C. Han, T. Niu, W. Chen, and A. T. S. Wee, “Critical Crystal Growth of Graphene on Dielectric Substrates at Low Temperature for Electronic Devices,” *Angew. Chem. Int. Ed.*, vol. 52, no. 52, pp. 14121–14126, 2013, doi: 10.1002/anie.201306086.

[114] B. Barwe, F. Riedel, O. E. Cibulka, I. Pelant, and J. Benedikt, “Silicon nanoparticle formation depending on the discharge conditions of an atmospheric radio-frequency driven microplasma with argon/silane/hydrogen gases,” *J. Phys. Appl. Phys.*, vol. 48, no. 31, p. 314001, July 2015, doi: 10.1088/0022-3727/48/31/314001.

[115] M. T. Swihart, “Vapor-phase synthesis of nanoparticles,” *Curr. Opin. Colloid Interface Sci.*, vol. 8, no. 1, pp. 127–133, Mar. 2003, doi: 10.1016/S1359-0294(03)00007-4.

[116] A. Bouchoule, A. Plain, L. Boufendi, J. P. Blondeau, and C. Laure, “Particle generation and behavior in a silane-argon low-pressure discharge under continuous or pulsed radio-frequency excitation,” *J. Appl. Phys.*, vol. 70, no. 4, pp. 1991–2000, Aug. 1991, doi: 10.1063/1.349484.

[117] K. G. Spears, R. P. Kampf, and T. J. Robinson, “Particle densities in radio-frequency discharges of silane,” ACS Publications. Accessed: Aug. 16, 2025. [Online]. Available: https://pubs.acs.org/doi/pdf/10.1021/j100329a046

[118] G. S. Selwyn, J. E. Heidenreich, and K. L. Haller, “Particle trapping phenomena in radio frequency plasmas,” *Appl. Phys. Lett.*, vol. 57, no. 18, pp. 1876–1878, Oct. 1990, doi: 10.1063/1.104021.

[119] A. A. Fridman, L. Boufendi, T. Hbid, B. V. Potapkin, and A. Bouchoule, “Dusty plasma formation: Physics and critical phenomena. Theoretical approach,” *J. Appl. Phys.*, vol. 79, no. 3, pp. 1303–1314, Feb. 1996, doi: 10.1063/1.361026.

[120] H. Do, G. Thieme, M. Froehlich, H. Kersten, and R. Hippler, “Ion Molecule and Dust Particle Formation in Ar/CH4, Ar/C2H2 and Ar/C3H6 Radio-frequency Plasmas,” *Contrib. Plasma Phys.*, vol. 45, pp. 378–384, Aug. 2005, doi: 10.1002/ctpp.200510043.

[121] F. Gao, S.-X. Zhao, X.-S. Li, and Y.-N. Wang, “Effects of matching network on the hysteresis during E and H mode transitions in argon inductively coupled plasma,” *Phys. Plasmas*, vol. 17, no. 10, p. 103507, Oct. 2010, doi: 10.1063/1.3496385.

[122] N. Balcon, A. Aanesland, and R. Boswell, “Pulsed RF discharges, glow and filamentary mode at atmospheric pressure in argon,” *Plasma Sources Sci. Technol.*, vol. 16, no. 2, p. 217, Jan. 2007, doi: 10.1088/0963-0252/16/2/002.

[123] S. Atlas *et al.*, “Investigation of Capacitively Coupled Radio-Frequency Argon Plasma: Integration of in Situ Optical Diagnostics with Data-Driven and Theoretical Modeling,” *Plasma Chem. Plasma Process.*, vol. 45, no. 4, pp. 1261–1292, July 2025, doi: 10.1007/s11090-025-10563-2.

[124] E. Amanatides and D. Mataras, “Frequency variation under constant power conditions in hydrogen radio frequency discharges,” *J. Appl. Phys.*, vol. 89, no. 3, pp. 1556–1566, Feb. 2001, doi: 10.1063/1.1337597.

[125] Y.-X. Liu, Y.-R. Zhang, A. Bogaerts, and Y.-N. Wang, “Electromagnetic effects in high-frequency large-area capacitive discharges: A review,” *J. Vac. Sci. Technol. A*, vol. 33, no. 2, p. 020801, Feb. 2015, doi: 10.1116/1.4907926.

[126] Y. Kondo *et al.*, “Silicon nitride etching performance of CH2F2 plasma diluted with argon or krypton,” *Jpn. J. Appl. Phys.*, vol. 54, no. 4, p. 040303, Mar. 2015, doi: 10.7567/JJAP.54.040303.

[127] H. J. Kim, K. Lee, and H. Park, “Effect of dilution gas on the distribution characteristics of capacitively coupled plasma by comparing SiH4/He and SiH4/Ar,” *Plasma Sources Sci. Technol.*, vol. 32, no. 11, p. 115008, Nov. 2023, doi: 10.1088/1361-6595/ad03bc.

[128] A. Akhoundi and G. Foroutan, “The effects of gas dilution on the nanoparticles nucleation in a low pressure capacitively coupled acetylene discharge,” *Phys. Plasmas*, vol. 24, no. 5, p. 053516, May 2017, doi: 10.1063/1.4983325.

[129] D.-J. Kim and K.-S. Kim, “Analysis on nanoparticle growth by coagulation in silane plasma reactor,” *AIChE J.*, vol. 48, no. 11, pp. 2499–2509, 2002, doi: 10.1002/aic.690481109.

[130] L. Mangolini and U. Kortshagen, “Selective nanoparticle heating: Another form of nonequilibrium in dusty plasmas,” *Phys. Rev. E*, vol. 79, no. 2, p. 026405, Feb. 2009, doi: 10.1103/PhysRevE.79.026405.

[131] F. Kunze, S. Kuns, T. Hülser, H. Wiggers, and S. M. Schnurre, “Validation of the silicon nanoparticle production on the pilot plant scale via long-term gas-phase synthesis using a microwave plasma reactor,” *Appl. Energy Combust. Sci.*, vol. 15, p. 100195, Sept. 2023, doi: 10.1016/j.jaecs.2023.100195.

[132] B. Buesser and S. E. Pratsinis, “Design of Nanomaterial Synthesis by Aerosol Processes,” *Annu. Rev. Chem. Biomol. Eng.*, vol. 3, pp. 103–127, 2012, doi: 10.1146/annurev-chembioeng-062011-080930.

[133] K. Ouaras, G. Lombardi, and K. Hassouni, “Nanoparticles synthesis in microwave plasmas: peculiarities and comprehensive insight,” *Sci. Rep.*, vol. 14, no. 1, p. 4653, Feb. 2024, doi: 10.1038/s41598-023-49818-3.

[134] L. Ravi and S. L. Girshick, “Coagulation of nanoparticles in a plasma,” *Phys. Rev. E*, vol. 79, no. 2, p. 026408, Feb. 2009, doi: 10.1103/PhysRevE.79.026408.

[135] A. Woodard, K. Shojaei, G. Nava, and L. Mangolini, “Graphitization of Carbon Particles in a Non-thermal Plasma Reactor,” *Plasma Chem. Plasma Process.*, vol. 38, no. 4, pp. 683–694, July 2018, doi: 10.1007/s11090-018-9884-4.

[136] S. K. Friedlander, *Smoke, Dust, and Haze: Fundamentals of Aerosol Dynamics*. New York: Oxford University Press, 2000.

[137] "Separation of Particles from a Gas: Gas Cyclones," in *Introduction to Particle Technology*, John Wiley & Sons, Ltd, 2008, pp. 247–264. doi: 10.1002/9780470727102.ch9.

[138] M. S. Seehra and A. S. Pavlovic, "X-Ray diffraction, thermal expansion, electrical conductivity, and optical microscopy studies of coal-based graphites," *Carbon*, vol. 31, no. 4, pp. 557–564, Jan. 1993, doi: 10.1016/0008-6223(93)90109-N.

[139] F. F. Chen and J. P. Chang, "Optical Emission Spectroscopy," in *Lecture Notes on Principles of Plasma Processing*, F. F. Chen and J. P. Chang, Eds., Boston, MA: Springer US, 2003, pp. 151–160. doi: 10.1007/978-1-4615-0181-7_28.

[140] J. W. Coburn and M. Chen, "Optical emission spectroscopy of reactive plasmas: A method for correlating emission intensities to reactive particle density," *J. Appl. Phys.*, vol. 51, no. 6, pp. 3134–3136, June 1980, doi: 10.1063/1.328060.

[141] W. E. Pretty, "The swan band spectrum of carbon," *Proc. Phys. Soc.*, vol. 40, no. 1, p. 71, Dec. 1927, doi: 10.1088/0959-5309/40/1/313.

[142] S. Marinov, V. Vachkov, I. Ivanov, and Z. Kiss'ovski, "Double-discharge plasma system for deposition of carbon nanostructures," *J. Phys. Conf. Ser.*, vol. 2240, no. 1, p. 012020, Mar. 2022, doi: 10.1088/1742-6596/2240/1/012020.

[143] R. C. Johnson, "V. The structure and origin of the Swan band spectrum of carbon," *Philos. Trans. R. Soc. Lond. Ser. Contain. Pap. Math. Phys. Character*, vol. 226, no. 636–646, pp. 157–230, Jan. 1997, doi: 10.1098/rsta.1927.0005.

[144] N. Konjević, M. Ivković, and N. Sakan, "Hydrogen Balmer lines for low electron number density plasma diagnostics," *Spectrochim. Acta Part B At. Spectrosc.*, vol. 76, pp. 16–26, Oct. 2012, doi: 10.1016/j.sab.2012.06.026.

[145] D. L. Crintea, U. Czarnetzki, S. Iordanova, I. Koleva, and D. Luggenhölscher, "Plasma diagnostics by optical emission spectroscopy on argon and

comparison with Thomson scattering," *J. Phys. Appl. Phys.*, vol. 42, no. 4, p. 045208, Jan. 2009, doi: 10.1088/0022-3727/42/4/045208.

[146] E. Dames, V. Rohani, and L. Fulcheri, "Chapter Five - Plasma chemistry and plasma reactors for turquoise hydrogen and carbon nanomaterials production," in *Advances in Chemical Engineering*, vol. 61, M. Pelucchi and M. Maestri, Eds., in Turquoise Hydrogen: An Effective Pathway to Decarbonization and Value Added Carbon Materials, vol. 61. , Academic Press, 2023, pp. 253–317. doi: 10.1016/bs.ache.2023.05.001.

[147] N. B. Uner and E. Thimsen, "Low temperature plasma as a means to transform nanoparticle atomic structure," *Plasma Sources Sci. Technol.*, vol. 27, no. 7, p. 074005, July 2018, doi: 10.1088/1361-6595/aad36e.

[148] U. Holzwarth and N. Gibson, "The Scherrer equation versus the 'Debye-Scherrer equation,'" *Nat. Nanotechnol.*, vol. 6, no. 9, pp. 534–534, Sept. 2011, doi: 10.1038/nnano.2011.145.

[149] J. B. Aladekomo and R. H. Bragg, "Structural transformations induced in graphite by grinding: Analysis of 002 X-ray diffraction line profiles," *Carbon*, vol. 28, no. 6, pp. 897–906, Jan. 1990, doi: 10.1016/0008-6223(90)90338-Y.

[150] A. C. Ferrari and J. Robertson, "Interpretation of Raman spectra of disordered and amorphous carbon," *Phys. Rev. B*, vol. 61, no. 20, pp. 14095–14107, May 2000, doi: 10.1103/PhysRevB.61.14095.

[151] Y. Hao *et al.*, "Probing Layer Number and Stacking Order of Few-Layer Graphene by Raman Spectroscopy," *Small*, vol. 6, no. 2, pp. 195–200, 2010, doi: 10.1002/smll.200901173.

[152] L. G. Cançado *et al.*, "Measuring the degree of stacking order in graphite by Raman spectroscopy," *Carbon*, vol. 46, no. 2, pp. 272–275, Feb. 2008, doi: 10.1016/j.carbon.2007.11.015.

[153] A. N. Popova, “Crystallographic analysis of graphite by X-Ray diffraction,” *Coke Chem.*, vol. 60, no. 9, pp. 361–365, Sept. 2017, doi: 10.3103/S1068364X17090058.

[154] X. Xiao, J. W. Elam, S. Trasobares, O. Auciello, and J. A. Carlisle, “Synthesis of a Self-Assembled Hybrid of Ultrananocrystalline Diamond and Carbon Nanotubes,” *Adv. Mater.*, vol. 17, no. 12, pp. 1496–1500, 2005, doi: 10.1002/adma.200401581.

[155] “Gas Correction Factors for Thermal-based Mass Flow Controllers.” Accessed: Aug. 22, 2025. [Online]. Available: https://www.mks.com/n/gas-correction-factors-for-thermal-based-mass-flow-controllers

APPENDICES

A. OPERATION AND CALIBRATION OF MFCs

Several mass flow controllers of various brands were available during the assembly of the experimental setup. However, none were supplied with their OEM controller units. For this purpose, an Arduino Mega-based control box and an Arduino Uno-based bubble flow meter device were built for MFC calibration and operation. Calibration was made via the bubble flow meter, which utilizes two lasers positioned across two photodiodes. The lasers and the diodes are housed in a 3D printed holder. The same holder carries a glass tube in between the lasers and the diodes, and it provides a platform for forming bubbles of a solution containing soap, glycerin and water. Formed bubbles travelled in the flow meter tube with constant speed thanks to the gas flow. The flow rate was measured through the time that takes for the bubble to pass between two lasers, and the inner diameter of the tube was known. The circuit diagram of the bubble flow meter is shown in Figure A1.

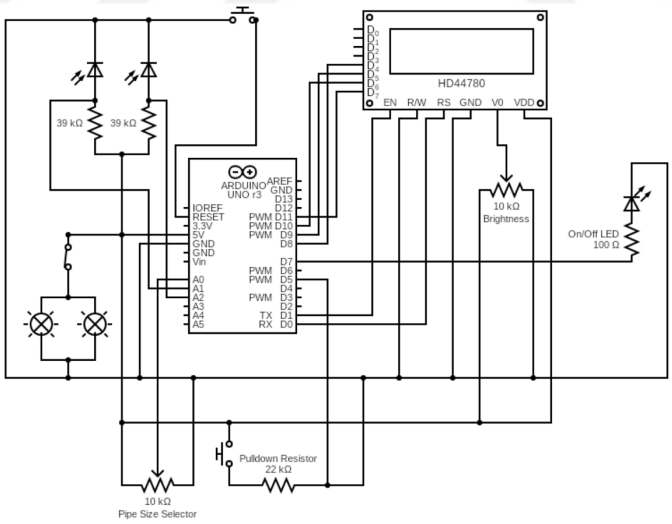

Figure A1. Arduino Uno circuit diagram for bubble flow meter device.

A similar Arduino circuit was built for controlling three mass flow controllers. All MFCs came with an analog communication whose pin outs were

either available online or on the MFC itself. From the pinouts, the related connections were made to an Arduino Mega controller due to vast number of pins required for three MFCs. Unit UFC-1200A, Horiba SEC-E440J and M+W Instruments D-5111 MFCs were connected to the controller via custom pinned DB9 connectors. Voltage was supplied to MFCs in ±15 VDC through two separate power supplies.

Successful operation was obtained with after verifying correct pin mapping which later required calibration of the MFCs to convert analog signal into meaningful flow. MFCs were calibrated using the bubble flow meter to obtain calibration curves for flow rate vs analog signal. For each MFC, flow rate versus 10-bit command (0-1023 counts) was recorded to generate calibration curves. Calibration was made using air and argon which helped cross-checking the gas calibration factor of the thermal-based MFCs and deviations from it. Flowrates corresponding to same analog signal usually gave the same argon/air ratio of 1.39 with small deviations. These deviations were corrected for each MFC according to the gas they utilized. No gas correction factor was used for M+W Instruments MFC as it was already calibrated using argon. Unit MFC was corrected with using methane conversion factor of 0.72 and the Horiba MFC was calibrated using hydrogen conversion factor 1.01 [155].

Table A1. Calibration data for Unit MFC used for methane.

Gas/Analog signal	*101*	*255*	*511*	*767*	*1023*
Air	42.79	90.75	165.93	243.48	319.59
Argon	61.06	129.19	238.49	347.28	452.89

Table A2. Calibration data for M+W MFC used for argon.

Gas/Analog signal	*101*	*255*	*511*	*767*	*1023*
Argon	127.16	323.6	639.86	943.36	1294.23

Table A3. Calibration data for Horiba MFC used for hydrogen.

Gas/Analog signal	*101*	*255*	*511*	*767*	*1023*
Air	41.57	112.18	228.53	339.75	454.69
Argon	-	156.16	322.02	474.30	636.040

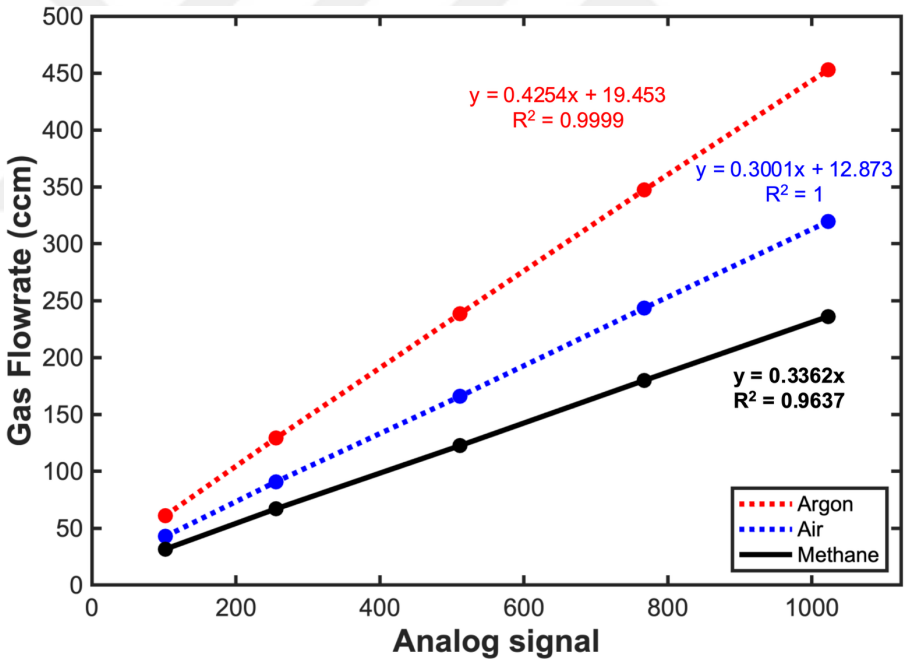

Figure A2. Calibration curves used for Unit UFC-1200A mass flow controller. MFC was used for methane flow.

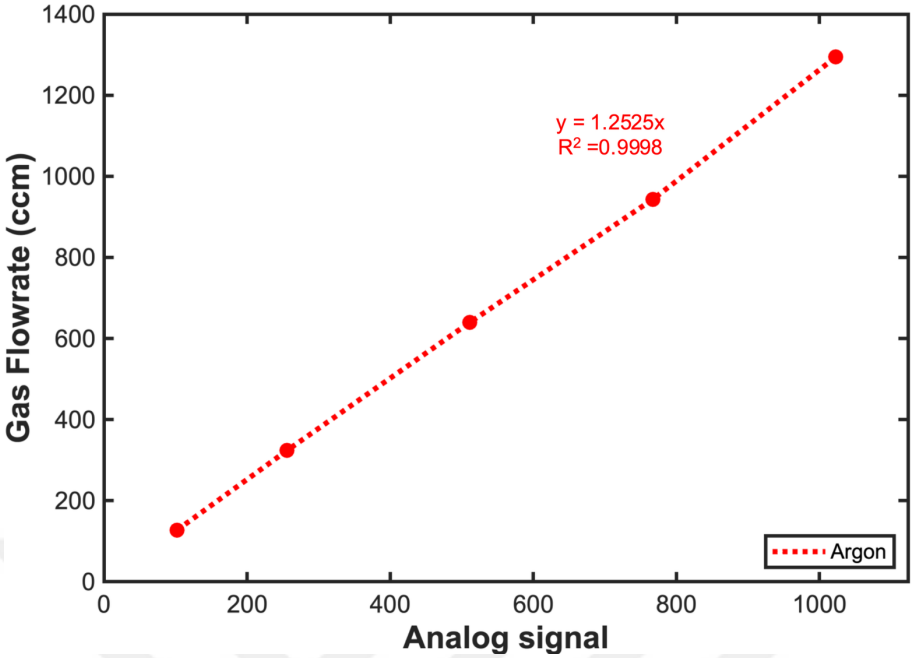

Figure A3. Calibration curves used for M+W D-5111 mass flow controller. MFC was used for argon flow.

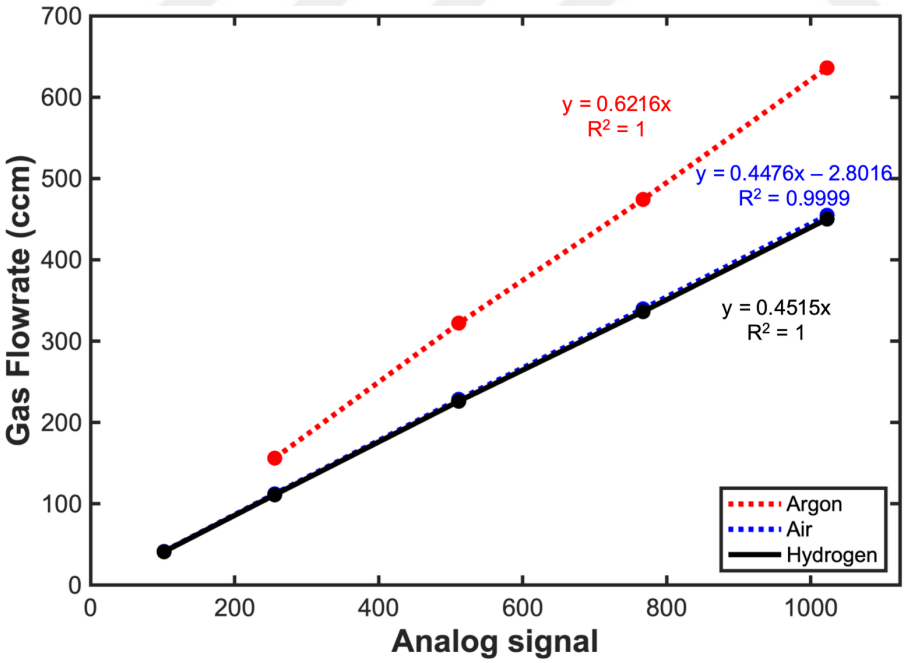

Figure A4. Calibration curves used for Horiba SEC-E440J mass flow controller. MFC was used for hydrogen flow.

B. STAIRMAND-TYPE LOW-PRESSURE CYCLONE SEPARATOR DESIGN

Stairmand-type cyclone separators are reverse flow type cyclone separators which have predetermined cyclone proportions with respect to its cylindrical diameter. In such reverse flow cyclone separators, particles are subjected to centrifugal forces which creates a vortex that reverses its direction at the bottom of the conical part and leaves the cyclone at the outlet in top part. Vortex created inside the cyclone induces a pressure gradient which makes up the total pressure drop combined with frictional forces on the walls. Total pressure drop is related to characteristic velocity through Euler number, Eu, where ΔP is pressure drop, ρ_f is gas density, u is characteristic velocity, $\dot{V}$ is volumetric flow rate and D is the inner diameter of the cyclone body.

$$\mathrm{Eu} = \frac{2\Delta P}{\rho_f u^2} \qquad \text{Eqn. B1}$$

$$u = \frac{4\dot{V}}{\pi D^2} \qquad \text{Eqn. B2}$$

According to the balance between centrifugal forces and fluid drag, the cyclone has a critical size of particles, X_{crit}, which determines the particles that are retained in the cyclone. Due to gas velocity fluctuations, particle interactions, re-entrainment and diffusion, there usually is a smooth transition in the number of particles captured around this critical size. Grade efficiency curve, which is used for describing how separation efficiency of the cyclone changes with particle size, is therefore S-shaped. In this S-shaped-curve, the particle size which yields a grade efficiency of 50% is named X_{50}. Alternatively called the cut size, this means that 50% of particles in this size will be collected as the coarse mode and remains in the cyclone, and 50% of it will leave the cyclone as the fine mode and. X_{50} is a useful concept as the cyclone efficiency can be expressed as a single number and can be used in scaling calculations.

Scaling of cyclone is based on the Stokes number which is a dimensionless number defined as the ratio inertial forces acting on the particle and drag forces caused by the fluid and it characterizes the separation performance of similar cyclone geometries. It is defined in Eqn. B3 where *C* is Cunningham slip correction factor and μ is gas viscosity.

$$Stk_{50} = \frac{\mathrm{C}X_{50}\rho_p u}{18\mu D} \qquad \text{Eqn. B3}$$

Cunningham slip correction factor is used for low pressure conditions when Knudsen number is larger than 0.1, where particle sizes are in the order of mean free path of gas molecules (λ). Slip correction modifies the drag force which in turn modifies the Stokes number to account for decreased gas-particle interactions. Cunningham slip correction factor is expressed in Eqn. B4 as a function of cut-size and the expression for mean free path was given as a function of Boltzmann constant (k_B), gas temperature (T_g), collision cross section area (σ) and pressure (P) in Eqn. B5.

$$C = 1 + \frac{2\lambda}{X_{50}}\left[1.257 + 0.4\exp\left(\frac{-0.55X_{50}}{\lambda}\right)\right] \qquad \text{Eqn. B4}$$

$$\lambda = \frac{k_B T_g}{\sqrt{2}\sigma P} \qquad \text{Eqn. B5}$$

Stairmand-type cyclones are classified as high efficiency (H.E.) and high flowrate (H.R.) cyclones. Stokes and Euler numbers for these geometries are prespecified. For high efficiency Stairmand cyclone Stk_{50} = 1.4 x 10^{-4} and Eu = 320 and for high flowrate Stairmand cyclone Stk_{50} = 6 x 10^{-4} and Eu = 46. Cyclone geometry parameters relative to diameter are given in Table B1 these parameters are shown in Figure B1 [137].

Table B1. Cyclone dimensions for H.E. and H.R. types relative to cyclone diameter D.

Cyclone Type	*A*	*B*	*C*	*E*	*J*	*L*	*K*	*N*
Stairmand, H.E.	4.0	2.5	1.5	0.375	0.5	0.2	0.5	0.5
Stairmand, H.R.	4.0	2.5	1.5	0.575	0.875	0.375	0.75	0.75

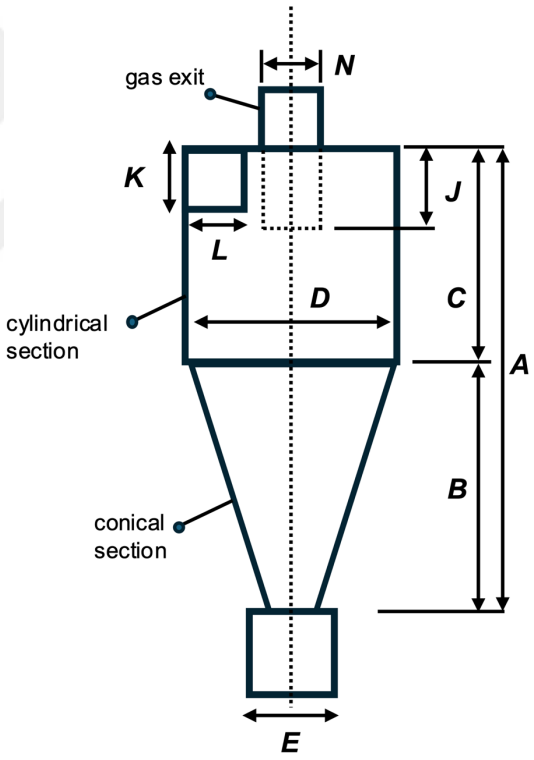

Figure B1. Geometry and defining parameters for Stairmand-type cyclone.

Equations B3 and B4 were solved simultaneously to determine the cut-size for a given cyclone diameter and flowrate in a H.R. type Stairmand-type cyclone shown in Eqn. B6.

$$X_{50}^2\left\{1+\frac{2\lambda}{X_{50}}\left[1.257+0.4\exp\left(\frac{-0.55X_{50}}{\lambda}\right)\right]\right\}=\frac{18\mu DStk_{50}}{\rho_f u} \qquad \text{Eqn. B6}$$

First, the effect of diameter was calculated using Eqn. B6. For the pressure range between 10-30 Torr, the predicted cut size decreased with decreasing cyclone diameter (Figure B2). Increasing pressure increased the cut size for any diameter due to reduced Cunningham slip correction factor. In order to minimize the cut size within manufacturing limitations, the smallest practical diameter, 21.33 mm, was selected. Second, at fixed diameter (21.33 mm), the effect of flowrate was investigated using Eqn. B6. Cut size was bigger for higher pressures similar to the previous case and as flow rate increased, cyclone performance was predicted to increase with a decrease in cut size.

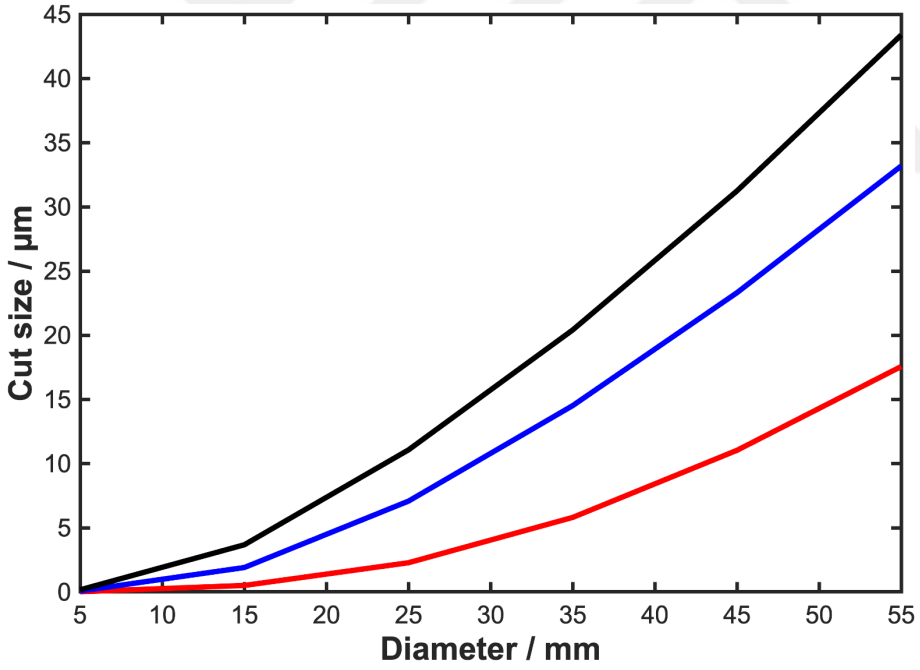

Figure B2. Variance in cut size with diameter. Red curve: 10 Torr, blue curve: 20 Torr, black curve: 30 Torr. *u* was calculated for 660 sccm flow rate at 500 K.

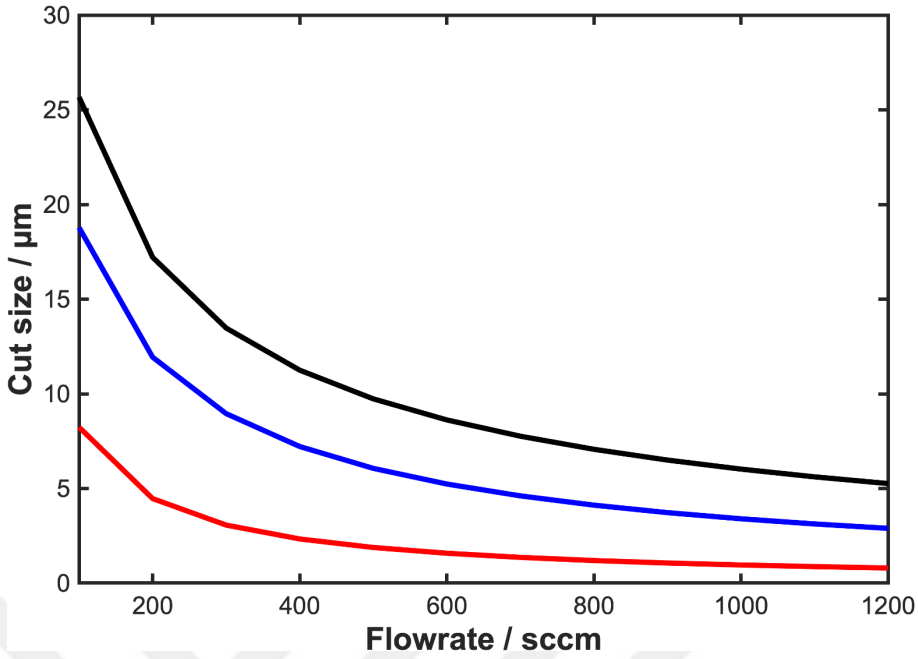

Figure B3. Variance in cut size with increasing flow rate. Red curve: 10 Torr, blue curve: 20 Torr, black curve: 30 Torr. Diameter was taken 21.33 mm at 500 K.

With predicted cut size from a few microns up to 20 microns, the cyclone was manufactured with diameter 21.33 mm and the rest of the parameters from Stairmand's design for high flowrate cyclones. Several changes were made to his design, where the entrance duct was changed into KF25 quick coupling flange for quick integration to the experimental setup. A 5 cm deep reservoir was designed for collecting large particles and the outlet was designed as KF25 quick coupling flange to maintain vacuum connections. The technical drawing of this cyclone is shown in Figure B4. The parts of the cyclone were manufactured in-house from 6013 grade aluminum shown in Figure B5. Parts were assembled through parallel threads which were covered with high-vacuum grease (Dow Corning). Void between the tangential part was covered with silicone sealant for enhanced vacuum tightness.

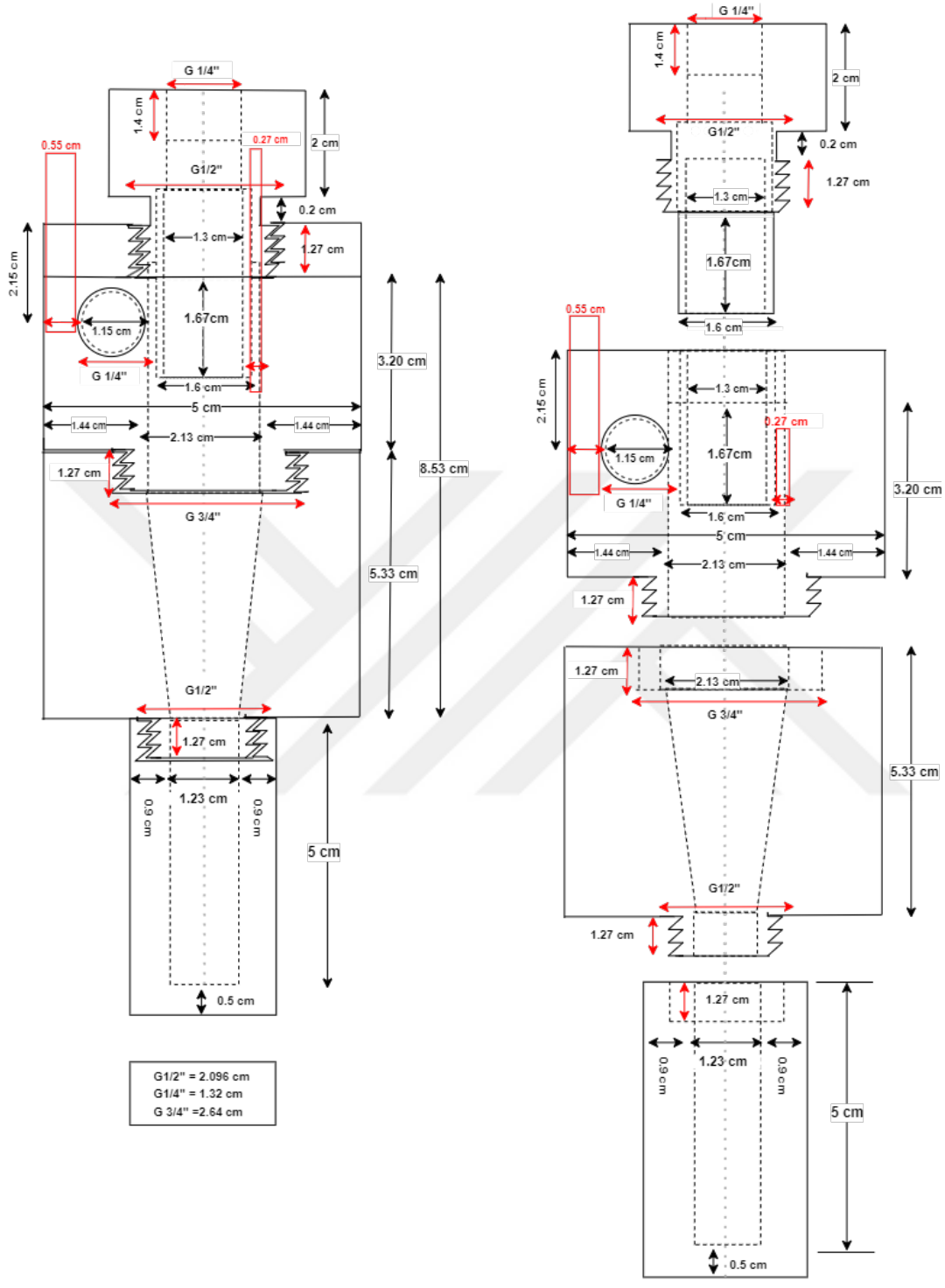

Figure B5. Dimensions of the parts that constitute the designed cyclone.

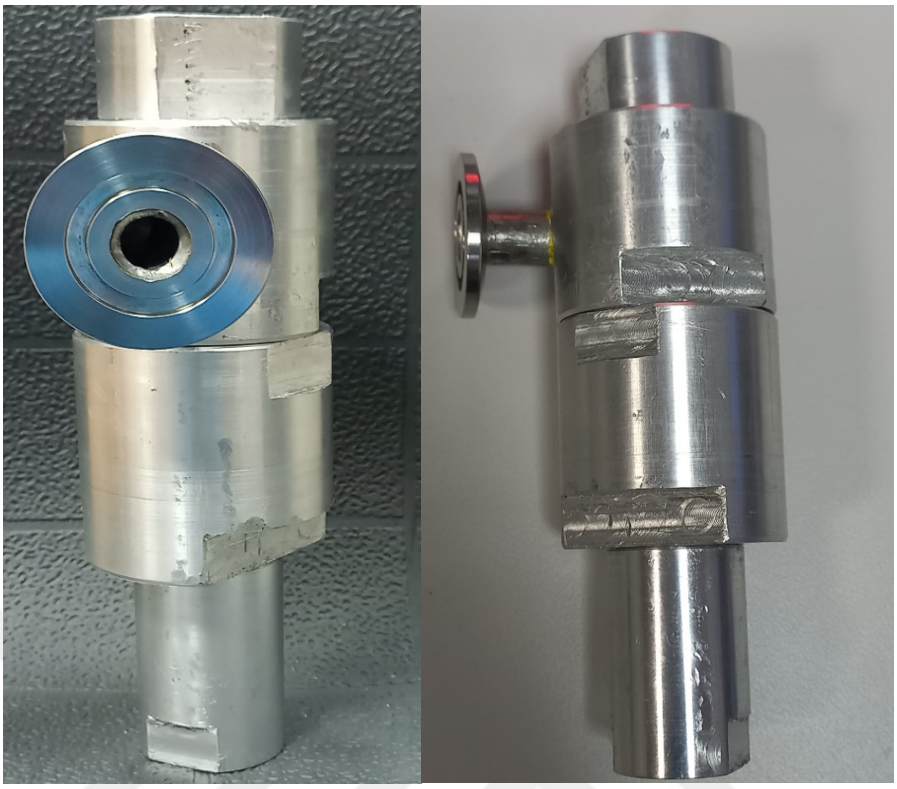

Figure B6. Photographs of the manufactured cyclone.

C. CALCULATION OF FILTER COLLECTION EFFICIENCY

Particle separation efficiency of the impaction stage and the cyclone was measured by placing 400 mesh stainless-steel filters just before the respective stage (Figure C1). Filter 1 was located before impaction tee, filter 2 was located at the entrance of the cyclone separator and filters 3 and 4 were located after the cyclone. Only filters 3 and 4 were installed together while conducting these experiments, in order to assess particle collection efficiency of the filter. Filters 1 and 2 were separately installed during different experiments. Two different residence times was used, (i) with total gas flow of 123 sccm where 3 sccm of methane was sent to the reactor at 46 ms residence time, and (ii) with total gas flow of 41 sccm where 1 sccm of methane was sent resulting in 139 ms. In order to keep total methane sent to the reactor constant, 46 ms experiments were run for 2 minutes and 139 ms experiments were run for 6 minutes.

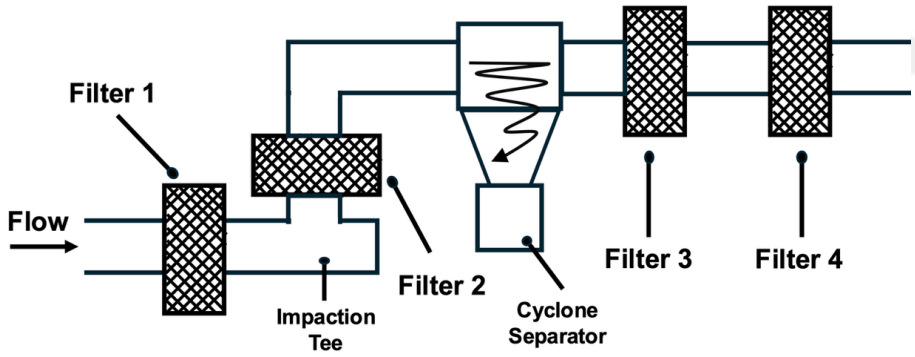

Figure C1. Locations of the filters for identifying filter collection and particle separation efficiency of impaction stage and cyclone.

Filter collection efficiency was calculated using the following approach. The amount of particles collected at the first filter downstream of the cyclone (m_3) is the product of particle collection efficiency of the filter (η) and total particle mass flow rate ($\dot{m}$) times the amount of time particles are collected (Δt).

$$\eta \dot{m} \Delta t = m_3 \qquad \text{Eqn. C1}$$

Similarly, the amount of particles collected at the second filter downstream of the cyclone (m_4) is the product of particle collection efficiency (η), and total particle mass flow rate ($\dot{m}$) times the amount of time particles are collected (Δt), minus particles collected at the first filter (m_3).

$$\eta(\dot{m} \Delta t - m_3) = m_4 \qquad \text{Eqn. C2}$$

Solving equation C1 and C2 for filter collection efficiency, the expression for η is obtained.

$$\eta = 1 - \frac{m_4}{m_3} \qquad \text{Eqn. C3}$$

Masses collected on the filters are summarized in Table C1. The collection efficiency of the stainless-steel filters was found approximately as 70%. The yield of in-flight synthesized particles was seen to change with respect to residence time, which is expected. Yields at 46 and 139 ms residence times were found to be 24% and 17% respectively.

Table C1. Particle amounts on filters and particle collection efficiencies.

Residence Time	*Filter 1*	*Filter 2*	*Filter 3*	*Filter 4*	$\eta_{collection}$
$\tau = 46$ ms	0.75 mg	0.66 mg	0.54 mg	0.15 mg	73%
$\tau = 139$ ms	0.59 mg	0.52 mg	0.49 mg	0.14 mg	71%

D. X-RAY DIFFRACTION DATA USED FOR FWHM CALCULATIONS

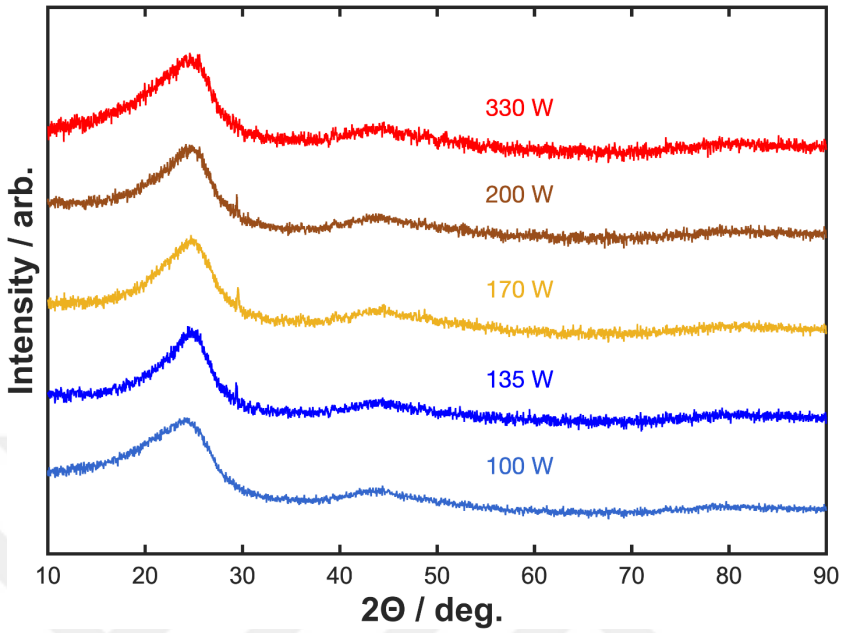

Figure D1. XRD spectra of particles as a function of plasma power. FWHMs of 2Θ = 26° was used in Figure 4.10-a.

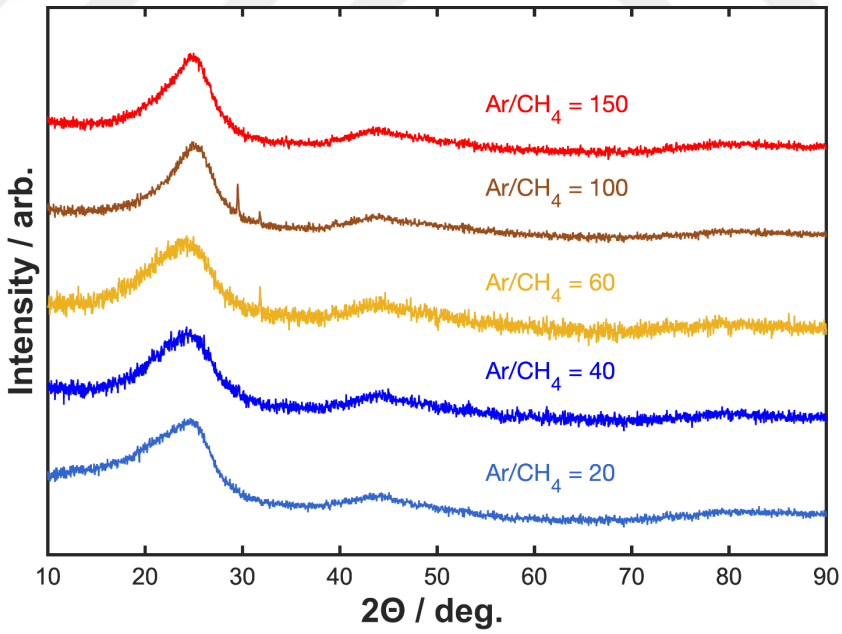

Figure D2. XRD spectra of particles as a function of Ar/CH_4 ratio. FWHMs of 2Θ = 26° was used in Figure 4.10-b.

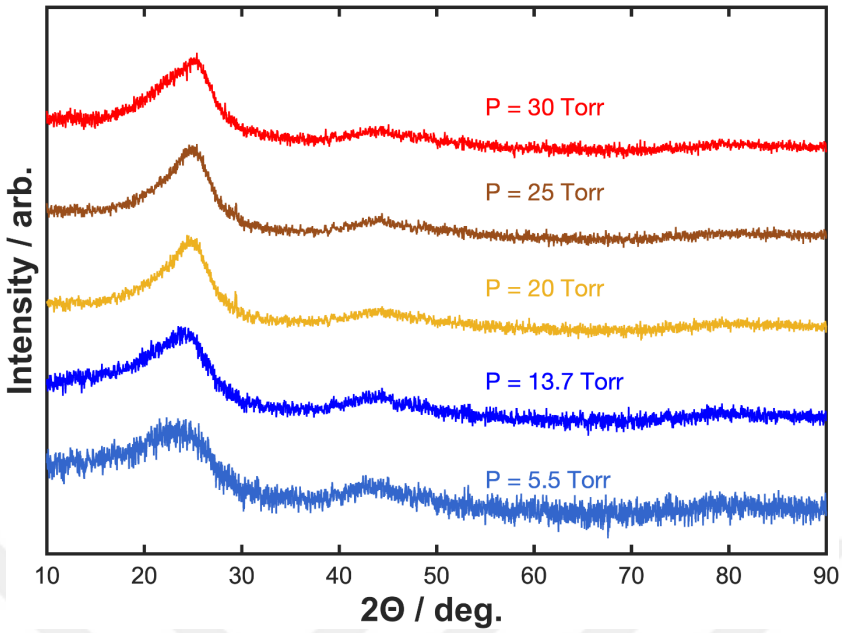

Figure D3. XRD spectra of particles as a function of pressure. FWHMs of 2Θ = 26° was used in Figure 4.10-c.